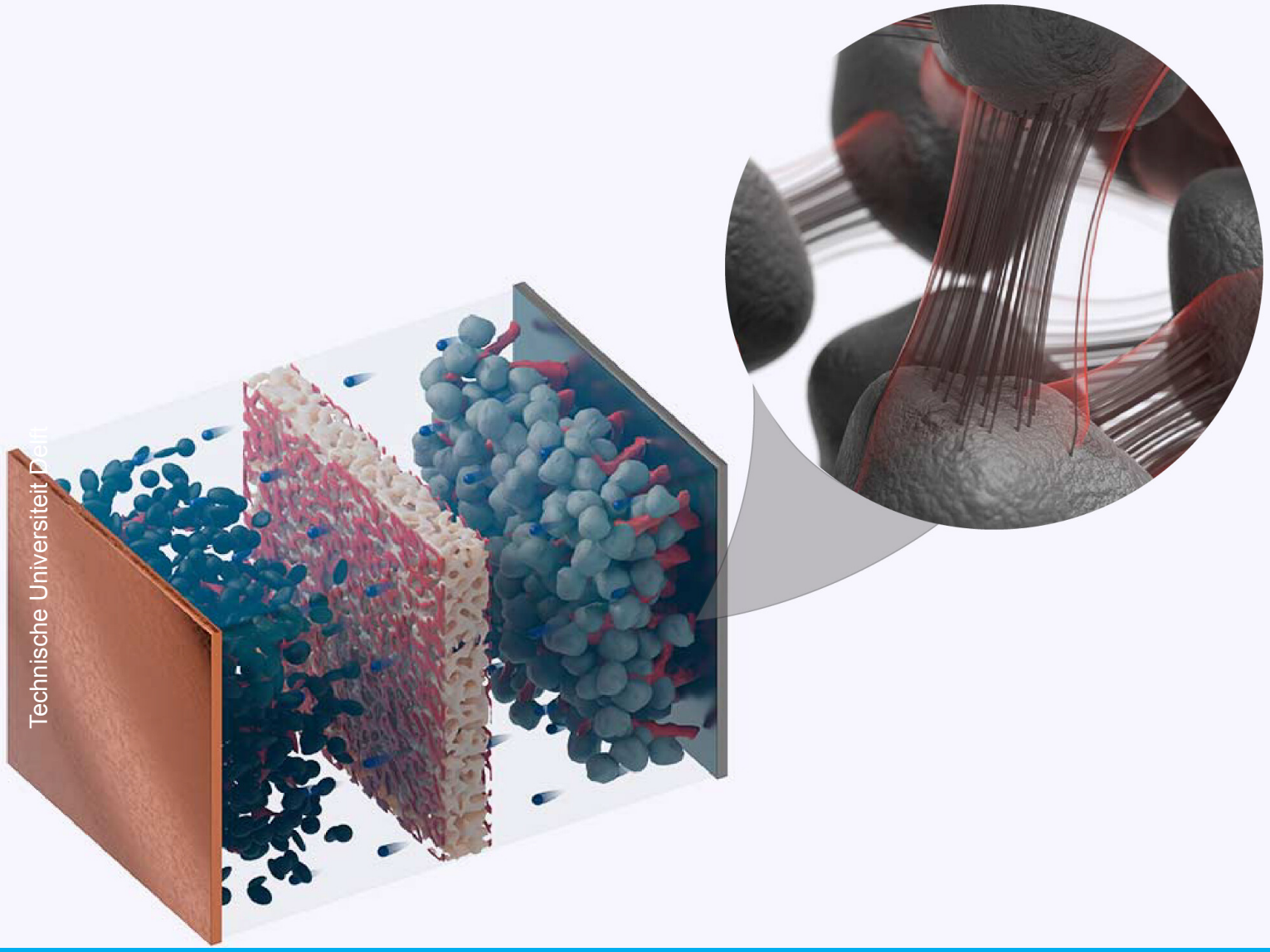

Technische Universiteit Delft

Temperature Effects and Performance Optimization in Battery Systems

Dimitrios Ntagkras

TU Delft

Temperature Effects and Performance Optimization in Battery Systems

by

Dimitrios Ntagkras

to obtain the degree of:

Master of Science in Mechanical Engineering

at the **Delft University of Technology**

to be defended publicly on Tuesday August 31, 2023 at 10:00 AM.

Student:	Dimitrios Ntagkras	
Student number:	5539587	
Contact:	dhmhtrhs_dag@hotmail.com	
Project duration:	November 16, 2022 – August 31, 2023	
Thesis committee:	Prof. dr. K. Hooman,	TU Delft, supervisor
	Dr. O. Moultos,	TU Delft
	Prof dr. ir. M. Wagemaker	TU Delft
	Dr. A. Vasileiadis,	TU Delft, co-supervisor
	PhD. P. Ombrini	TU Delft, co-supervisor

An electronic version of this thesis is available at `http://repository.tudelft.nl/`.

TU Delft

Acknowledgements

I would like to express my deepest gratitude to all those who have supported and guided me throughout the course of this thesis project. Their invaluable contributions and unwavering support have played a significant role in the completion of this endeavor.

First of all, my main supervisor, Kamel Hooman, showed to me his trust from the first day, and whenever something unexpected popped up, even for non-related stuff to my thesis, he was trying to help me and to show me twith his experience how to manage these cases. His expertise and commitment to my academic growth have been instrumental in shaping the direction of this research. My daily supervisor, P. Ombrini , was always there, even in his holidays, he was answering every doubt and without his help, this project could not be embodied. Alexandros Vasileiadis, my co-supervisor, with his unique understanding and his incredible way to impart very complex phenomena enhances my comprehension for electrochemistry and the underlying physics.

I am also indebted to the members of my thesis committee, for their constructive presence and valuable suggestions. Their expertise has enriched the quality of my work and helped me refine my ideas.

I extend my appreciation to Frans Ooms, the main technician in the battery lab, which in the beginning of the project and during my experiments he worked with me like a supervisor and i enrich not only my practical but also my theoretical knowledge in materials. Our discussions and brainstorming sessions have been invaluable in shaping the trajectory of my research.

My sincere thanks go to my family and friends for their unwavering support, encouragement, and understanding throughout this journey. Their belief in my abilities has been a constant source of motivation. Special thanks to Rahul Nanda, Suenley Paulina and Dimitrios Mintsis with whom i shared all my thoughts and my doubts and we were struggling all together for similar problems through the process.

I am grateful to TU Delft for providing the necessary resources, access to the library, and a conducive research environment that have facilitated the completion of this thesis.

Finally, I want to express my gratitude to all those unnamed individuals who have, in one way or another, contributed to the development of this project. Your influence may be hidden but is certainly not forgotten.

In conclusion, this thesis project stands as a testament to the collective effort of many individuals who have played a pivotal role in its completion. Their guidance, encouragement, and support have made this journey both fulfilling and rewarding.

Thank you.

Contents

List of Figures

List of Tables

Nomenclature

Abbreviations

Abbreviation	Definition
(aq)	Species are dissolved in water
BMS	Battery Management System
BV	Butler-Volmer
C	Carbon
Co	Cobalt
Cd	Cadmium
DFN	Doyle-Fuller-Newman
DFT	Density Functional Theory
EMF	Electromagnetic Force
Fe	Iron
GHG	Greenhouse gas
H	Hydrogen
HOMO	Highest Occupied Molecular Orbital
e^-	electron
Li	Lithium
LUMO	Lowest Unoccupied Molecular Orbital
LFP	Lithium Iron Phosphate
MHC	Marcus-Hush-Chidsey
MPET	Multiphase Porous Electrode Theory
n	number of electrons
Ni	Nickel
O	Oxygen
OCV	Open-circuit Voltage
P	Phosphorus
Pb	Lead
R-C	Resistor-capacitor
R-L	Resistor-Inductor
S	Sulfur
(*s*)	solid
SEI	solid-electrolyte interface
SOC	State Of Charge

Symbols

Symbol	Definition	Unit
b_a	Tafel's slope	-
dq	infinitesimal amount of charge	C

Symbol	Definition	Unit
D_s	Self-diffusion coefficient	$(3.2 \pm 0.5)\ m^2/s$
S	Solubility	$mol\ kg^{-1}$
A	Area	m^2
c_R	concentration of the reactant	mol/L
E_a	Activation Energy	J
E_{oc}	Open-Circuit Voltage	V
F	Faraday's constant	$9.68*10^7$ C/mol
G	Gibbs free energy	J
j	Current Density	A/m^2
H	Enthalpy	J/kg
I	Current	A
k	electronic conductivity	$\Omega^{-1}\ m^{-1}$
L	Length	m
N_v	Volume-averaging Product Flux	$mol/(m^2/s)$
$\dot{Q}_{irr}$	Irreversible heat loss	W
$\dot{Q}_{rev}$	Reversible heat loss	W
R	Resistance	Ω
R_v	Volume-averaging Reaction Rate	C/s
S	Entropy	J/(K mol)
T	Temperature	K
v	Velocity	m/s
x	Dimensionless Fractional concentration	-
α	charge transfer coefficient	-
γ	Activity coefficient	-
$\Delta_e h$	Enthalpy of evaporation	$J\ mol^{-1}$
$\Delta\phi$	potential difference	V
ϵ_s	Porosity	-
η	Overpotential	V
μ	Chemical potential	J/mol
ρ_e	Charge Density	C/m^3
σ	electrical conductivity	S/m
τ	Tortuosity	-
τ_+	transference number	-
Ω	regular solution parameter	J/mol

Temperature Effects and Performance Optimization in Battery Systems

Dimitrios Ntagkras

Abstract

As the energy transition gains momentum, the development of effective energy storage technologies is crucial. Among these technologies, batteries are of utmost importance as they store chemical energy that can be converted into electrical energy. The operation of batteries is a complex process that involves the interplay of material technology, multiphysics transport phenomena, and mechanical effects. While experiments can reveal new and unexpected features of batteries in various conditions, simulation models offer a cost- and time-effective way to gain valuable insights across a wider range. However, the accuracy and fidelity of mathematical models are directly proportional to the complexity of describing all the relevant phenomena. To date, equivalent-circuit models have been the dominant framework for industrial applications due to their simplicity and low computational cost. However, these models treat batteries as black boxes, which limit users' ability to interpret the results. In contrast, physics-based models that couple electrochemistry, conservation laws, and heat equations can produce high-fidelity models that capture the intricacies of battery operation. The Multiphase Porous Electrode theory (MPET) provides a useful framework for integrating these phenomena and enables users to modify parameters that can significantly impact simulation results. In this study, experiments in different operating temperatures were conducted and analysed, and based on these outcomes, the accuracy and validity of MPET was tested. The root mean squared error between the simulation and experimental results was smaller than 5% in all cases. The correlation between the high temperature (50 °C) discharge curve and the ambient temperature discharge curve showed the high dependence of temperature to the state of charge of the battery which was confirmed by the experiments. Furthermore, a possible degradation mechanism could have an impact in the final results. The main research outcomes were the exponential relation between the temperature and the rate constant and between the particles conductivity and the temperature. Using these two relations, the model could reproduce the same trend and equal maximum capacity with the experiments. This shows the flexibility of the model in completely different operating conditions. After the validation, the active particle population model can be used to understand the coccurent or particle by particle intercalation and gives indentifications of hotspot in a battery. The final part was a sensitivity analysis about capacity optimization taking into account not only different C-rates but also different temperatures. Because the whole study was in an experimental coin cell, a relation to bigger battery systems should be built in the same manner using this software so as to facilitate the development of more effective energy storage technologies.

Keywords: *Li-ion batteries, phase separation materials, temperature dependency, parameter estimation, optimization, machine learning, physics-based models.*

1

Introduction

1.1. Motivation

Nowadays the energy transition is imperative to move to a more sustainable world and to sketch new pathways for technology. Fossil fuels are the main raw material of electricity and the relation with the CO_2 (carbon dioxide) emissions is inextricable. Global warming and generally increasing incidents of severe weather are the main consequences of these emissions [9]. As it is obvious in Figure 1.1, during the last three decades, in almost all the sectors, the greenhouse emissions are decreased significantly [28]. This downward trend is attributable to new global energy regulations aimed at achieving net-zero emissions by the mid-century. Wind turbines and solar panels are pivotal drivers of the substantial reduction in greenhouse gas emissions from the energy industry. However, the intermittent nature of renewable energy sources, stemming from their reliance on weather conditions, prevents them from fully dominating the energy supply throughout the year. The solution to this intermittent operation lies in energy storage. Battery energy storage systems, flywheels, compressed air storage systems, and ultracapacitors are among the innovative technologies that, at varying scales, seek to bridge the technical and economic gaps associated with renewable sources [1].

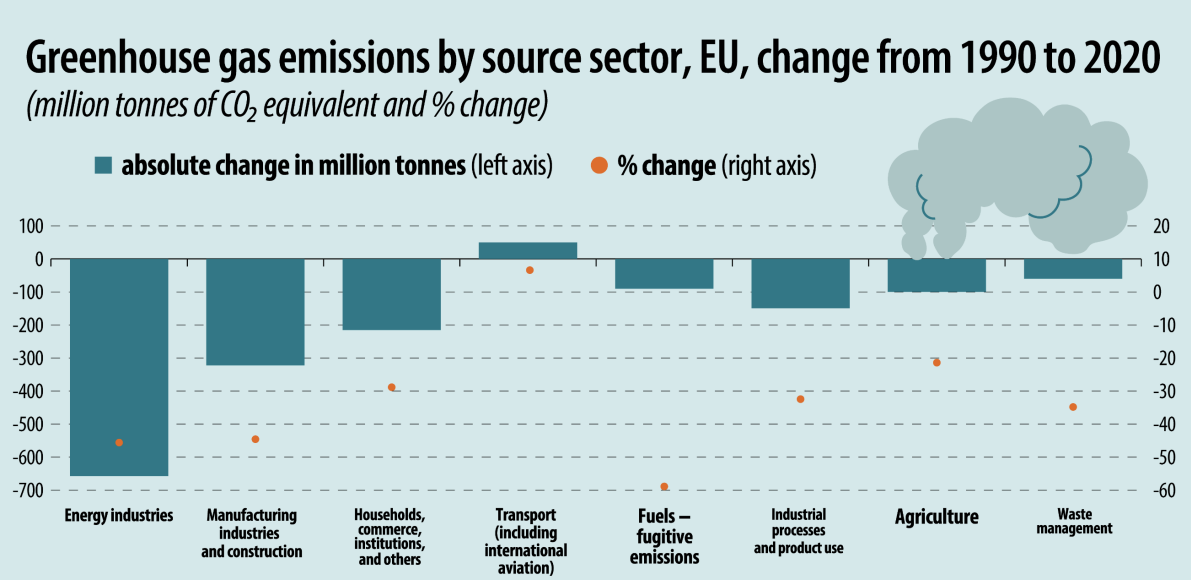

Figure 1.1: Greenhouse gas emissions by source sector in Europe from 1990 to 2020 [28].

The sole exception to this trend, with a slight increase over the last three decades, is observed in the transportation sector [28]. In Figure 1.2, it is illustrated the classification of GHG emissions based on the different methods of transportation [28]. Road transport possesses more than 75% of the bar that indicates the amount of emissions in million tones every year. Surprisingly, in 2020 the emissions from this specific sector diminished to almost half of the amount of the previous year but this was caused by the appearance of Covid-19. Thus, the electrification of vehicles is a massive step towards the sustainability [6]. The transition to hybrid and electric vehicles promises a significant reduction in emissions within this sector, serving as a cornerstone of the broader energy transition. Batteries, which constitute a key component of electric vehicles and energy storage applications, play a central role in this transformation.

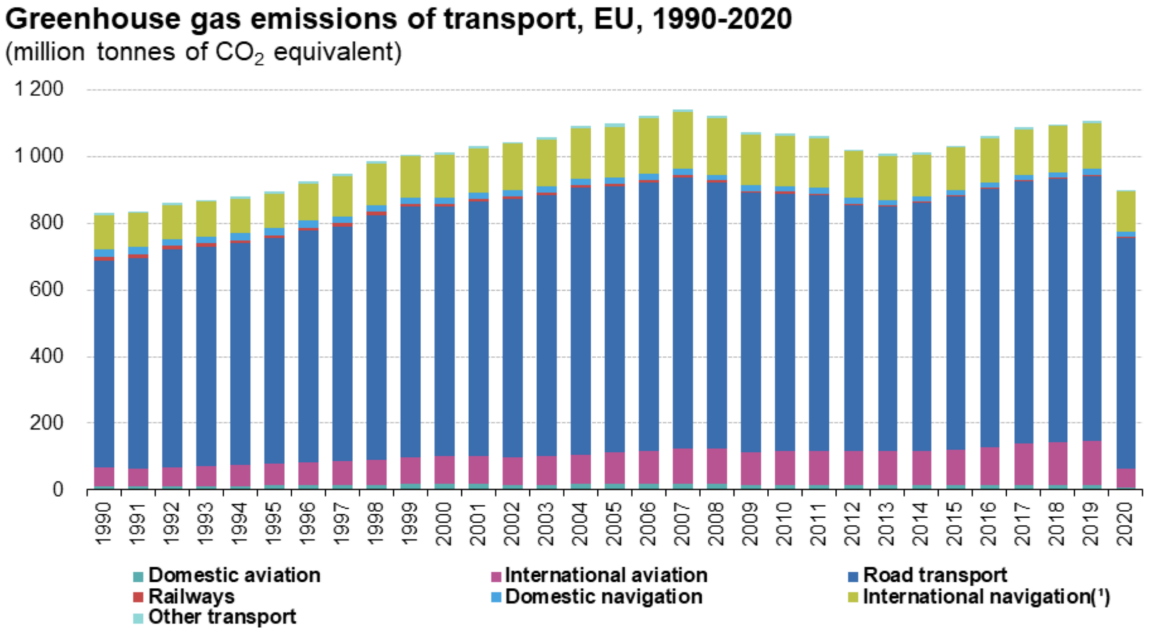

Figure 1.2: Greenhouse gas emissions of transport from 1990 to 2020 [28].

1.2. Challenges of Li-ion Batteries

The availability of the materials used as cathode and anode is crucial to avoid becoming a limiting factor in the development of batteries. The anode is typically made of graphite, a widely available material. This prudent choice stems from the fact that the total global reserves of graphite reached 320 million metric tons in 2021 [27]. On the other hand, the primary compounds used in cathodes are lithium-transition metals, which are combined with salts such as phosphate (PO_4^-), nickel (Ni), iron (Fe), and manganese (Mn). These salts are not only readily available, but they also complement the properties of lithium [5].

One of the main concerns of batteries' manufacturers is the charging requirements. The time that one electric car can be charged and the range of this charge is inseparably connected with the chemistry and the ability of the compounds such as the intercalation process [22]. The efficiency of a battery is significantly influenced by temperature. Understanding the stable operational region of the battery is essential, as it guides the thermal management system to prevent potential hazards such as over-charging, thermal runaway, electrolyte decomposition and more. Moreover, high performance and cycle life are crucial components of the figure of merit of batteries. To remain competitive in the market, companies need to use cost-effective metals. Recycling these batteries poses a significant challenge, and most companies aim to collect the battery components as alloys or aggregates rather than recovering each metal separately [22].

The development of a very stable electrolyte is one of the biggest challenge. The stability window of an electrolyte is defined by its lowest unoccupied molecular orbital (LUMO) and the highest occupied molecular orbital (HOMO). The Fermi energy level in the anode should be smaller than the LUMO, otherwise undesirable reactions will occur forming unstable compounds. For the same reason the Fermi level in the cathode should be higher than the HOMO. The "extension" of this stability window will result to higher safety measures and will enhance the research to new electrolyte compositions which can tolerate higher voltages without decomposition.

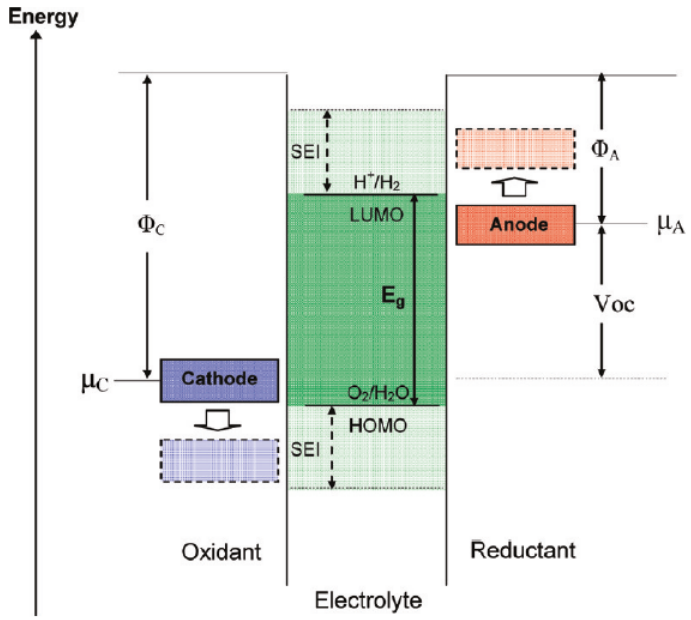

Figure 1.3: Stability window of an electrolyte with and without a SEI layer[19] .

1.3. Modelling of a battery

The lifetime and the performance of a battery rely on its physical properties. The vital parameter is not the power consumption but how fast is the charge and the discharge process. Hence, the responsibility of the battery management system (BMS) is to ensure the safe and the efficient operation of these processes. The control of parameters such as the state of charge (SoC), state of health (SoH), overdischarge and overcharge are the main function of the BMS and this is the reason why the modelling of batteries is so significant to the development of this technology [40].

Equivalent-circuit models

1. **Simple models:** This model consists of an internal resistance that can represent the different losses in a battery (ohmic losses, activation losses etc.) and an ideal voltage source. In a real battery the resistances, because of transport limitations that were described previously, vary. Thus, the dynamic parameters of the problem such as the state of charge [41] does not take into account for influencing the resistance's value.

2. **Thevenin models:** This is a more advanced electrical-circuit model which has the ability to capture the transient behavior of phenomena, for example higher discharge rate and varying stage of charge. With the use of resistor-capacitor networks in series and in parallel, these models are capable of representing many complicating electrochemical incidents without going inside the battery. The nonlinear effect of the state of charge can not be calculated accurately with the use only of resistor-capacitor networks but the combination with machine learning through experimental data, can create a reliable model which has also very small computational cost. This is the main advantage and why the majority of the automotive industries are using these models in the BMS [40].

Machine Learning models

1. **Data-driven models:** The field of machine learning has become pervasive in various technological domains. One key advantage of these techniques is their ability to achieve high accuracy while requiring relatively low computational costs. The power of these models are higher because of the capability to capture the nonlinear behavior which is present in many different parameters in batteries. The three phases of these model are the pre-processing (sorting and evaluation of data), training (allow the model to be trained in an adequate data points from different scenarios) and estimation (predict the behavior of the component in new and unprecedented data to validate its level of accuracy). However, it is important to note that machine learning models are inherently reliant on collected data, and the accuracy and reliability of a given model depend on the range of cases that the data has captured and the quality of the data sorting. While experimental data can be used to train these models, there is a risk of misinterpreting the battery's state of health. Additionally, machine learning models do not offer insight into phenomena such as solid electrolyte interface formation or lithium plating, making it difficult to investigate these processes [24]. In cases of thermal runaway or other unexpected outcomes, these models cannot offer information about the root cause of the issue, making it difficult to address the problem in future application.

Electrochemical models

1. **Moving Reaction zone model:** These models assume that a specific region participates in a reaction and this region moves with time. It is crucial to accurately model the activation losses with respect to the state of charge, as the resistance of inactive material at the beginning of the discharge process is very small. However, as the discharge region expands, molecules should

travel longer distances to reach the reaction zone, resulting in greater activation losses. As the state of charge changes over time, activation losses should also be time-dependent. A commonly used assumption is that electronic conductivity is much higher than ionic conductivity in the electrode, as the metal of the electrode enhances the movement of electrons. However, it is important to note that this model does not consider partially discharged regions and only assumes fully charged and discharged regions. This model is more applicable in high charge and discharge rate applications[20].In this model, the use of the equation 2.12 is chosen for the cell voltage.

2. **Single particle models:** The focus of this model is on a single particle. Basic assumptions such as that the concentration in the electrode is constant or that the ionic conductivity is a lot higher are present. This model is suitable for slow charge applications where the concentration through the electrode does not change significantly and the model can simulate a homogeneous concentration by solving only for one particle. Solving the diffusion equation and the mass conservation equation for one particle, the important variables can be calculated through the whole electrode assuming no variation in the other particles. The conservation law about concentration should be solved both for the solid concentration in the electrode but also for the electrolyte concentration. Expressing all the mechanisms (reaction resistances due to concentration, mass transport limitations, etc) that are also present in the macroscopic scale of an electrode, the creation of such a model is doable and can provide surprisingly precise results and reliable models for validation.

3. **Doyle-Fuller-Newman model(DFN):** A pseudo-two-Dimensional model which uses non-linear partial differential equations and algebraic equations in order to describe the complex interaction between the electrode and the electrolyte. The model is volume averaging approach so as to assume that this region is homogeneous and continuous. This is the main reason why this model is appropriate for solid- solution active materials. Mass transfer equations and electrochemical relations are used to describe phenomena like diffusion or overpotential in this model [40]. This is a macro-homogeneous model which provides the opportunity to the user to change not only the design aspects of the battery, such as the electrode thickness and porosity but also the physical properties such as the diffusion coefficient of the solid or the electrolyte [41]. Every finite volume in the anode and cathode assumes to consist of one spherical homogeneous particle so as to show that the whole finite volume has the same physical and chemical properties[17]. The main obstacle of implementing this model to BMS is that the high complexity of solving these equations require powerful computational tools in order to minimize the runtime. Although, in a pilot-scale can give a lot of insight and, thus, can improve not only the research but also find solutions in the development of batteries. For example, the lithium plating can be diminished by controlling the overpotential and this choice can be done only with a physics-based model [24].

1.4. The need of Modelling

Computational modeling entails creating a virtual representation of the behavior of complex systems using principles derived from mathematics, physics, and computer science. Modeling offers numerous advantages across a wide range of applications. It enables efficient simulations under various operating conditions, leading to cost savings by reducing the necessity for extensive experiments.

By utilizing modeling techniques, it becomes possible to investigate separate processes and understand their impact on the overall system. Furthermore, the incorporation of optimization algorithms can greatly enhance the development of engineering tools. Computational models offer a

safer and more cost-effective alternative to conduct experiments under extreme conditions. It is important to note that the purpose of modeling is to guide experiments rather than replace them.

One of the key challenges is creating an accurate model that avoids making excessive assumptions while maintaining a manageable computational time. Thorough examination of assumptions is crucial to ensure that the model closely represents reality. Therefore, a solid understanding of the underlying physics is essential for developing a reliable model. Last but not least, one of the most important point of digital models is the choice of a representative unit which can describe more accurately the problem but also can capture the dynamics. Thus, the length scale of your model is critical.

1.5. Rationale and structure of study

This work delves into the influence of temperature on battery performance and the phase separation of cathode materials. It encompasses electrochemical experiments alongside the validation of a computational model. The study places a heightened focus on the solid dynamics within a particle, facilitating the shaping of distinct concentration profiles. Through investigation, it becomes evident that temperature engenders voltage loss and influences the heterogeneous behavior observed through experimentation. Unlike some other models, the research model adeptly captures and elucidates this phenomenon, offering vital insights into the interior processes without resorting to an opaque 'black box' approach.
In chapter 2, a theoretical overview is given of any mechanisms underlying and a general overview of the operation of Li-ion battery is illustrated. Additionally, the transport limitations and the phase separation definition are introduced. While the methodology section is situated in chapter 3, it is specifically referred to the computational section. Parameter estimation techniques are also elaborated and the technique of this study is also present in the end of the chapter. The experimental methodology and experimental results of this study is discussed in chapter 4. Furthermore, in this section, the entire experimental procedure is explained. The validation of the computational model, the computational results and the sensitivity analysis are conducted in chapter 5. The study is concluded in chapter 6, and a set of recommendations for future work are included in chapter 7.

2

Theoretical Background

The goal of the following sections are to provide a general overview of the underlying physics in Li-ion batteries and more specifically in the phase separation materials like LFP cathode batteries.

2.1. Terminology

In the Appendix there is a table which describes important terminology that will be used in the next sections. If a definition is unclear, the reader can refer to this table(Table A.1).

2.2. Constituents and Operational Mechanisms of a Battery

As shown in Figure 2.1, in the negative electrode which is mostly a lead metal, during the discharge process, electrons leave from the current collector (depicted in orange) and through an external circuit goes to the positive electrode through the cathode current collector (depicted in grey). The white rectangular section between the electrodes is called a separator which , not only, distinguishes the two regions but also does not allow electrons to flow so as to prevent a short circuit. The build of charge during the operation of the battery is compensated by the movement of ions with the help of an electrolyte. Electrolyte enhances the movement of cations or anions through the separator while it is an electronic insulator as mentioned before. Thus, the electrolyte is a solvent with dissolved chemicals which can be alkaline or basic based on the application, so as to consist of positively and negatively charge molecules.

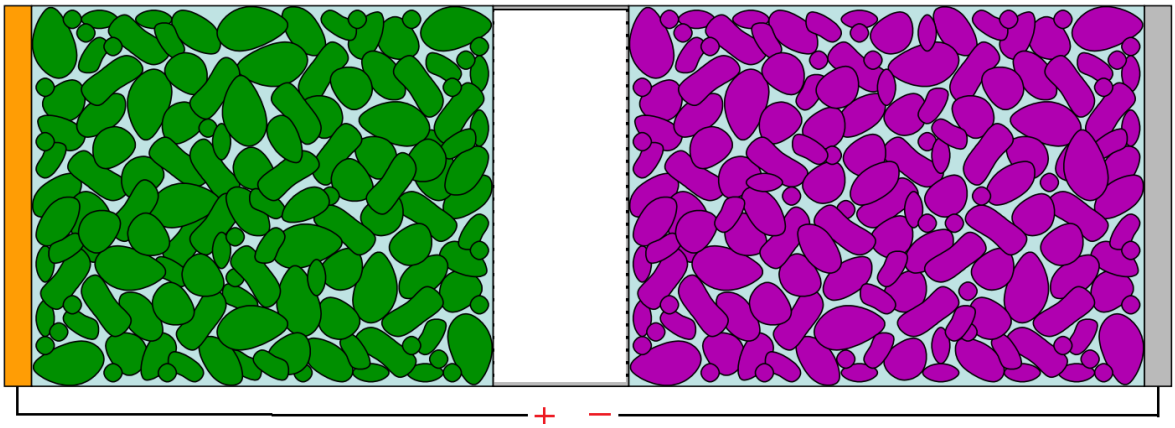

Figure 2.1: Basic components of a battery cell [18].

It is pertinent to note that the fundamental operating principle of a battery is predicated on the concept of electrochemical potential energy. This notion postulates that materials possess an inherent tendency to either emit or accept electrons based on their composition. In the discharge phase of a battery, the anodic material loses electrons, which causes ions to migrate from the anode to the cathode. If the electrochemical reactions occurring within the battery are reversible, then electrical energy can be generated, which can be subsequently converted into chemical energy. The electrochemical potential energy can be likened to the gravitational potential energy of a ball placed above a surface (Figure 2.2). If the ball falls from this height the gravitational (potential) energy will convert to kinetic energy. In order to return the ball to this height, work should be supplied equal to the gravitational energy.

The **figure of merit** of a battery comprises critical parameters that are essential for designing new batteries. These parameters include capacity, energy density (which is a function of weight), voltage, long cycle life, and low cost, among others. In addition to these parameters, the anode material must possess at least one electron in a valence state, while the cathode material should exhibit a propensity to close the outer shell with at least one electron. Consequently, manufacturers are limited to using specific materials

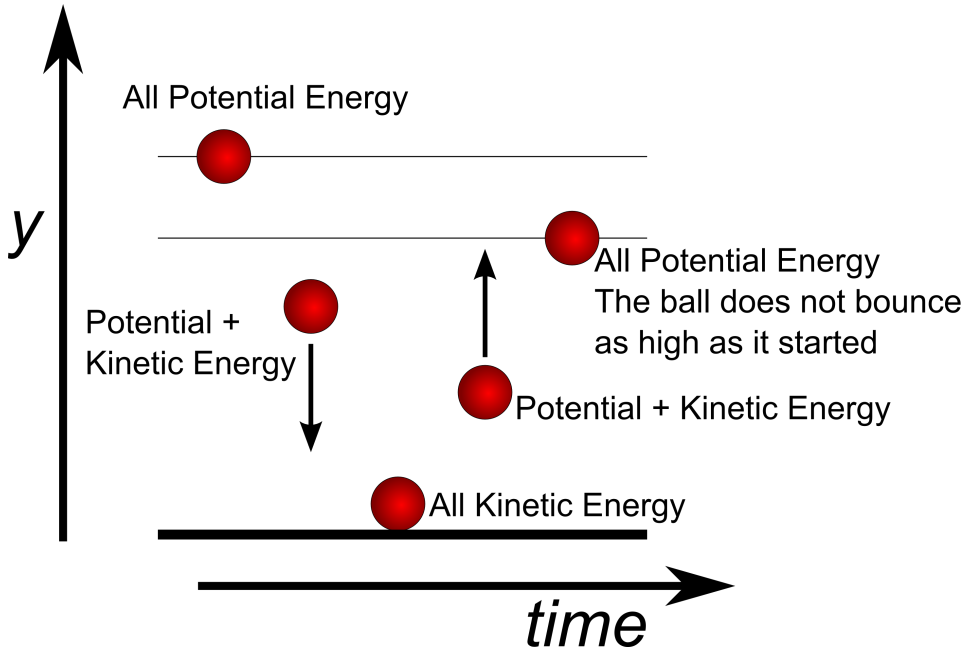

Figure 2.2: Conversion of potential to kinetic energy [8].

2.2.1. Intercalation Working Principle

The lithium-ion battery cell operates through a process known as intercalation, where the movement of lithium ions is akin to cars parking in slots. This process preserves the electrode structure, which is crucial. During discharge, the lithium atom loses an electron, resulting in Li^+, which traverses the electrolyte and separator to reach the cathode, where it meets an electron and reverts to its original state as neutral Li. Therefore, the material's crystal structure must be open to enable the insertion and extraction of lithium atoms. Another important concept to grasp is that during the anode's (discharge) process, the lithium atom that transforms to an ion resides on the particle's surface, and to return to equilibrium, the concentration on the surface must be replenished by diffusion from the particle's center. Conversely, in the cathode, the opposite recovery through diffusion occurs since the lithium concentration is higher on the surface when it reaches the positive electrode. The inhomogeneity of the particles creates partial lithiation, which will be described in detail in a separate section. The degree of lithiation is extremely significant in determining the amount of power generated and Joule heating produced through current in a specific location. Binders are also added to the material to improve electronic conductivity.

2.3. Cell Potential and Overpotential

The cell potential, also known as the electromotive force or EMF, of a battery is the maximum potential difference that can be achieved between the electrodes of the battery, when no current is flowing. It is a measure of the ability of the battery to do work and is determined by the difference in the standard electrode potentials of the two half-cells that comprise the battery, as well as the concentration of the species involved in the redox reactions that occur at the electrodes. The cell potential is typically expressed in volts (V) and is a critical parameter in determining the performance and efficiency of a battery. Hereby, before creating the final formula of the cell voltage, the individual losses should be considered and analysed below.

Ohmic losses: It is related to the difficulty in the movement of electrons in the electrode and the movement of ions in the electrolyte and the separator. Based on the Ohm's law (2.1) and the Poullet's law(2.2), a construction of an equation which relates the voltage drop and the conductivity and the geometrical properties are presented below.

$$\Delta\phi = I \cdot R \tag{2.1}$$

$$R = \frac{L}{A \cdot k} \tag{2.2}$$

Where $\Delta\phi$ (V) is the potential difference, I (A) is the current, R (Ω) is the resistance, L (m) is the length of the electrode, A (m^2) the area of the electrode and k (Ω^{-1} m^{-1}) the conductivity. Combining these two equations, the final equation is Equation 2.3(j (A/m^2) is the current density).

$$\Delta\phi = \frac{j \cdot L}{k} \tag{2.3}$$

It is obvious that the goal is to minimize this loss by increasing the conductivity and decreasing the length so as to not only diminish the voltage drop but also the cost of production.

Activation losses: This loss is referred to the energy required by the reactants to initiate the transformation into the products. As illustrated in Figure 2.3, the magnitude of the activation energy is influenced by various factors, such as the endothermic or exothermic nature of the reaction, temperature and the corresponding kinetic energy of the molecules, and concentration of the reactants. Consequently, the product flux is contingent on the aforementioned variables in a proportional manner (Equation 2.5).

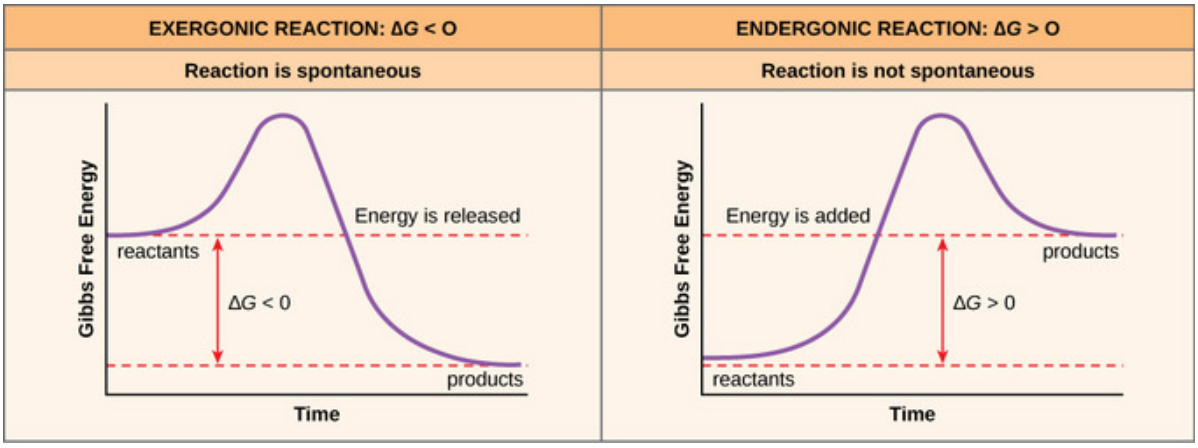

Figure 2.3: Activation energy in spontaneous and non-spontaneous reactions.

Using Faraday's law (2.4) which comes from mass and charge conservation and assuming first order reactions (2.5), the current density can be expressed through the equation 2.7:

$$j = n \cdot F \cdot N \tag{2.4}$$

$$N \propto c_R \cdot e^{\frac{-E_a}{R \cdot T}} \tag{2.5}$$

$$j \propto n \cdot F \cdot c_R \cdot e^{\frac{E_a}{R \cdot T}} \tag{2.6}$$

where n is the number of electrons that is moving from anode to the cathode, F(C/mol) is the Faraday's constant, N(mol/(m^2/s)) is the product flux, c_R(mol/L) is the concetration of the reactants, E_a(J) is the activation energy, R(J $K^{-1}mol^{-1}$) is the gas constant and T(K) is the temperature.
The activation energy can also be expressed with respect to the potential difference between the electrode and the electrolyte and a charge transfer coefficient α which lowers the barrier and decides which is the rate-limiting step of the reaction (i.e. electron transfer limited if α is close to 1).

$$j \propto n \cdot F \cdot c_R \cdot e^{\frac{\alpha_0 \cdot F \cdot (E-\phi)}{R \cdot T}} \tag{2.7}$$

Using the definition of activation overpotential (the potential difference above the equilibrium potential required to overcome the activation energy, equation 2.8) and the exchange current density (the current at zero overpotential,equation 2.9), the final equation is called Butler-Volmer equation (equation 2.10) and accounts for the most fundamental equation of electrochemistry.

$$\eta = (E-\phi) - (E-\phi)_{eq} \tag{2.8}$$

$$j_* = nF(k_O c_{R,eq})^{a_O}(k_R c_{O,eq})^{a_R} \tag{2.9}$$

$$j = j_* \cdot \left(\frac{c_R}{c_{R,eq}} \cdot e^{\frac{\alpha_0 \cdot F \cdot \eta}{R \cdot T}} - \frac{c_O}{c_{O,eq}} \cdot e^{\frac{-\alpha_R \cdot F \cdot \eta}{R \cdot T}}\right) \tag{2.10}$$

The subscript O is referred to the oxidation process and R to reduction, c is the concentration and k is the rate constant of the reaction. The Butler-Volmer equation is the difference between the anodic and cathodic current and shows that the higher the exchange current density is the lower the activation losses are.

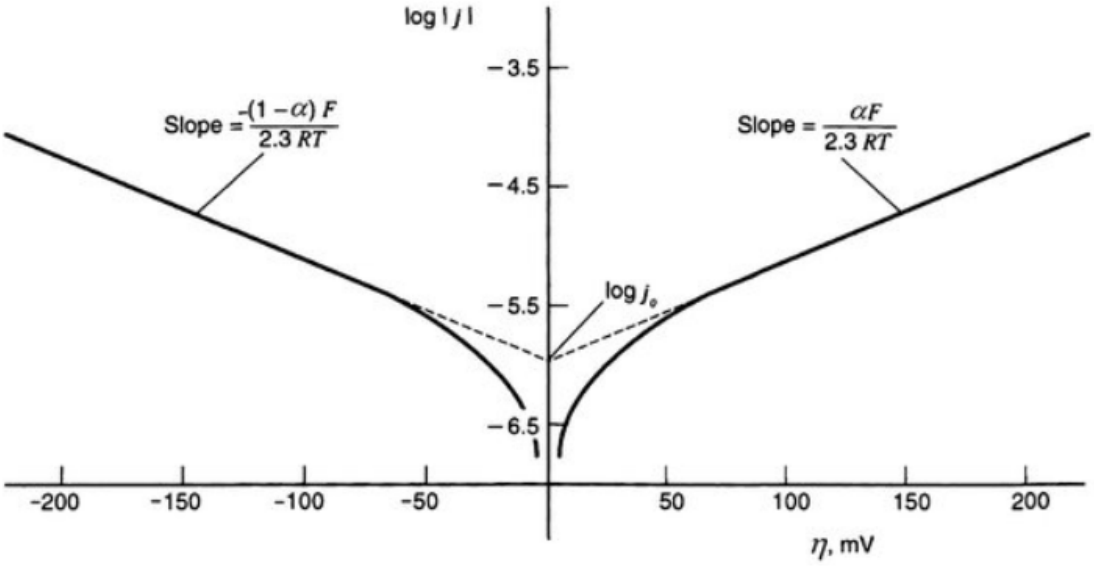

Figure 2.4: Anodic and cathodic tafel plot (concentration independent) of current with respect to overpotential[36].

In the case that one of the reduction or the oxidation reaction dominates, the Butler-Volmer equation becomes Tafel equation. Using the Figure 2.4, you can calculate the exchange current density, which physically represents the current that is needed in order for a molecule to jump the activation barrier (thus a higher exchange current density minimizes the activation losses), but also the coefficients of the Tafel equation which is the tafel slopes.

$$j = j_* \cdot \frac{c_R}{c_{R,eq}} \cdot e^{\frac{\eta_a}{b_a}} \tag{2.11}$$

where b_a is the anodic Tafel slope which is equal to RT/(α_oF). Connecting all the above, the final formula of the cell voltage is presented below:

$$V_{cell} = E_{oc} - (\eta_c - \eta_a - \Delta\phi - \Delta V) \tag{2.12}$$

where, E_{oc} is the open-circuit voltage, η_c and η_a is the overpotential in the cathode and the anode respectively which relates the activation losses, $\Delta\phi$ is the voltage drop because of the ohmic losses due to ions' transport and ΔV is the voltage drop because of the cable and electrode resistances(due to electrons' transport).

2.3.1. Overpotentials during charge transport

A comprehensive understanding of overpotential requires a detailed examination of the multiple sources that contribute in electrochemical reactions. This approach involves careful consideration

of the distinct types of overpotential that may arise and their individual contributions to the overall overpotential observed in a given system.
1)Ionic conduction in the electrolyte: The diffusion of an ion not only through the separator but also though the porous electrodes which is happening using the electrolyte as a carrier. Material properties such as the mobility of ions and the density of an ion but also concentration and electrical field gradients are the main mechanisms that drive this transport. The Fick's law equation and the more general Nernst-Plank equation is some of the fundamental equations that can be used to describe this phenomenon.
2)Charge transport over the electrolyte-electrode interface: The reaction between the electrolyte and the electrode enhances the transfer of ion in the electrode particle. This transport can be expressed with the Butler-Volmer equation and is related to the activation barrier that should be overcome in order to happen this reaction.
3)Ionic conduction in the electrode material: The diffusion of an ion in the particle in order to reach an electron and form Li. The ion transport through a lattice depends on the attempt jump frequency that Li has so as to go from one stable position to the other one. Using Density Functional Theory (DFT) you can simulate this behavior and calculate the diffusion of Li in a crystal structure.
4)Electronic conduction in the electrode material: The diffusion of an electron through the binders and the additive material so as to reach the electrode particle and diffuse in the particle to reach the ion (3rd charge transport).

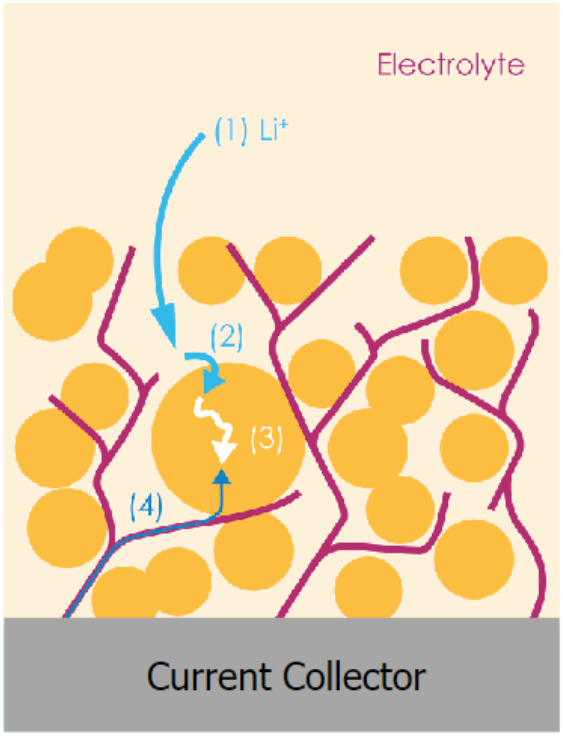

Figure 2.5: The tranport limitations that were described before with the respective numbering.

2.3.2. Cell Voltage and Gibbs Free Energy

It is vital to connect the cell voltage with the Gibbs free energy in order to explain the trend of voltage curves (Figure 2.7) and explaining phenomena like solid solution or phase separation.

$$-E_{cell}dq = \sum_i \mu_i dn_i \tag{2.13}$$

where μ(J/mole) is the chemical potential, dn is the number of moles, and dq is the amount of charge which is equal to z· F · dn. Assuming that the lithium concentration in the anode is constant in order to create a relation about the cell voltage which will be dependent only to the cathode chemical potential. Thus,

$$E_{cell}(x) = -\frac{\mu^{Li}_{cathode}(x)}{F} \tag{2.14}$$

The definition of chemical potential is the derivative of the Gibbs free energy. The final relation is given below:

$$E_{cell}(x) = -\frac{1}{F}\frac{\partial g(x)}{\partial x} \tag{2.15}$$

2.3.3. Phase separation

The immiscible mixture of two compounds such as oil and water is a phase separation example. The coexistence of two or more different phases in the same material with different chemical and physical properties is what is called phase separation and the miscibility gap is the range of compositions where this phenomenon can occur. A regular solution model is able to capture the thermodynamic properties of such a problem and relates the composition of lithium to the cell voltage.

$$g(x) = k_b T(x\ln(x) + (1-x)\ln(1-x)) + \Omega x(1-x) \tag{2.16}$$

where x is the dimensionless fractional concentration(0-1), k_b is the Boltzmann's constant, T (K) is the temperature and Ω is called regular solution parameter. This parameter is related to the enthalpy of mixing and explains if enthalpy or entropy term is dominant. The entropy term is the term before Ω in the equation and the enthalpy term is the last term. Using the equation and the figure 2.6, it is implied that when the regular solution parameter is smaller than $2k_bT$, the system prefers to be in disorder, thus a homogeneous solution is possible during the lithiation of the electrode. On the other hand, increasing the Ω the nature can find different paths of minimum Gibbs free energy and this results to partially lithiated spaces. There are lithium-poor and lithium-rich regions which is what is called phase separation regions. In other words, when the voltage is measured, in reality the chemical potential is measured and is inextricably connected to each other. Using this mathematical description for the Gibbs Free energy (Eq.2.16), the boundary involves naturally and the different interfaces can be captured and not artificially implemented.

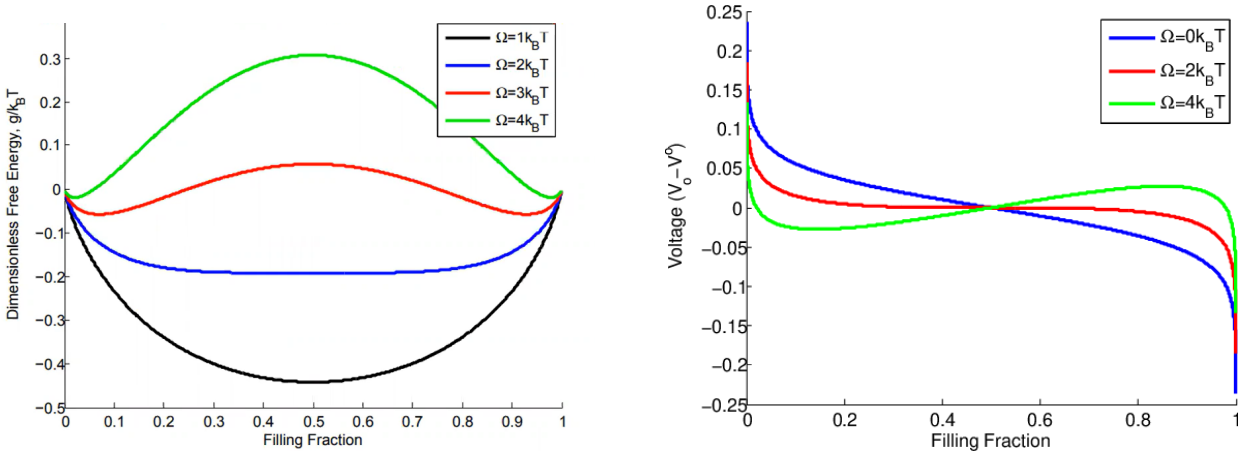

Figure 2.6: Gibbs free energy (Left) and Voltage profile (Right) with respect to lithium concentration and different Ω [16] .

2.4. Temperature influence in batteries

The demanding charging and discharging requirements, as well as the challenging vehicular environment, exert a notable influence on the operational parameters of the battery. In this context, the thermal management system plays a crucial role in maintaining the battery's temperature within the optimal range of 30-45 °C, thereby enhancing its efficiency and performance [7].

Thermal runaway is the biggest danger in batteries and can occur when the battery is exposed to high temperatures, such as when it is overcharged, overheated, or damaged. When the temperature of the battery increases, the electrolyte inside the battery can start to break down, leading to the release of oxygen and other gases. The increased pressure inside the battery can cause the battery to rupture and catch fire[15]. There are many mitigation techniques such as separating the battery cells from communicating thermally with each other (addition of a material that prevents the thermal propagation but enhances the electrical conductivity between the cells), or using safety controls(immense liquid flow for cooling) in a case of an excess of heat in the battery module[12].

2.4.1. Constant temperature impact in batteries

The coupling of electrochemical models with a thermal model is mandatory to describe accurately the internal behavior of a battery. Empirically, it has been observed that the diffusivity of solid state lithium, reaction rates, and electrolyte conductivity and diffusivity can be effectively characterized by an Arrhenius relationship with respect to temperature, thereby providing valuable insights from a practical standpoint. Thus, the previous parameters can be defined according to the following relation[7]:

$$f(T) = f_{ref} e^{\frac{E_a}{R}(\frac{1}{T_{ref}} - \frac{1}{T})} \tag{2.17}$$

E_a(J) is the activation energy, R(J $K^{-1}mol^{-1}$), T_{ref}(K) is the reference temperature and T(K) is the operating temperature. The function f is the parameter of interest. Although the cell voltage is nonlinear so it can be measured through the energy equation.

The total chemical energy that can be converted to useful electrical energy and irreversible heat dissipation is described by the following relationship:

$$-A\frac{\partial G}{\partial t} = I \cdot V + A \cdot \dot{Q}_{irr} \tag{2.18}$$

where G is the total Gibbs energy in the cell, I(A) is the current produced in this time step multiplied by the voltage V(V), A is the area of the cell and $\dot{Q}_{irr}$ is the irreversible heat loss which is very sensitive to the operating temperature [7]. This irreversible heat loss represents the following losses: dissipated effects in the electrolyte, the heat of mixing in the anode particles , Ohmic dissipation in the solid parts of the anode , dissipation arising from the current flow across the overpotential drop at the surfaces of the anode particles (also termed the polarisation loss),the heat of mixing in the cathode particles , Ohmic dissipation in the solid parts of the cathode and the polarisation losses at the surfaces of the cathode particles[34]. A very important note is that this is for the **isothermal** case through a cell so the left hand side of equation 2.18 is zero.

Battery development is being decelerated because of the temperature influence during its operation. Pesaran, Santhanagopalan, and Kim [31] showed that the temperature impact can be categorized in low and high temperature effects. In cold conditions (below $0°C$) the ion transport resistance increases and in temperature higher than $40°C$, side reactions can occur spontaneously leading in battery degradation. He found out that in low ranges of temperature, the formation of a dendrite is more possible, which has as an effect the cycle life reduction of the battery. On the other hand, despite that higher temperature leads to higher reaction rate(2.17), thus low charge overpotential, the occurrence of side-reactions lowers the amount of lithium that can intercalate having as a result the decrease of the cycle life. Moreover, Liu, Gao, and Cao [26] studied the impact of temperature to the LFP battery capacity. The experiments conducted in the temperature range between $-10°C$ to $60°C$ and the capacity was measured every 20 cycles. The main outcome was that temperature higher than $60°C$ has the most significant effect in the cycle life which shows that this is the upper temperature limit for a battery operation. The lower bound is the $-10°C$ and in Liu's research this temperature has the second biggest impact in the capacity and in the internal resistance of the battery. Surprisingly, the internal resistance for temperatures higher than the upper limit is bigger than the very low temperatures in spite of the proportionality between internal resistance and the Arrhenius relation.

Duong, Bastawrous, and See [13] created an equivalent circuit model to simulate the temperature effect on state of charge estimation in the LFP battery under dynamic load operation. After experiments in different temperatures, the voltage curve with respect to the state of charge is diminishing with decreasing temperature. The equivalent circuit model can predict accurately the voltage curve in a big range but below $0°C$ the model fails because the relation between the OCV and temperature becomes nonlinear [21]. Paarmann et al. [30] investigated the temperature influence to the current distribution in a cell experimentally. The conclusion was that the cell exhibits a significantly lower current for lower temperatures than for higher temperatures.Although, the voltage dependency to the different constant operating temperature and the position where the current is maximum has not been examined in this research.

2.5. LFP characteristics

The first automotive batteries from Tesla was with NCA but from 2021, the most well-known electric automotive company decides to change to LFP batteries. For this reason, it is important to investigate the reasons behind this action. The high resistance because of the low diffusion rate and the poor electrical conductivity of LFP gives a primary idea that it can not be the first choice of a manufacturer. If we look in the atomic scale, the atoms of iron are far away from each other(more than 4 Angstroms apart) because of the existence of the oxygen atoms (Figure 3.6). It is assumed that one material has good electronic conductivity if the distance between the iron atoms is below

3 Angstroms. On the contrary, the crystal structure of NCA provides high conductivity because of the small distance of Nickel atoms. Although, this creates instability and does not allow the full delithiation of the electrode in order to prevent a crystal buckling. Thus, the researchers, except from creating nanoparticles as it is mentioned above, carbon coatings increases drastically the surface area and the conductivity between LFP cathode [37]. Even with these innovations, including that the LFP batteries need less packaging, the LFP material is outplayed by the NCA in pack level performance as it is obvious in the table below.

Table 2.1: Comparison of LFP and NCA [37]

Characteristics	Lithium Iron Phosphate(LFP)	Nickel Cobalt Aluminium(NCA)
Energy Density Pack	128 Wh/kg and 168Wh/l	160 Wh/kg and 238Wh/l
Safety	High	Low
Cycle life	760k to 1M Miles	250k to 320k Miles
Acceleration/Power	Great	Great(can become excellent)

A significant difference between nickel cobalt aluminium (NCA) and lithium iron phosphate (LFP) lies in their voltage curve. Due to the 2-D diffusion in NCA, lithium ions can move freely within the electrode during the discharge process. In contrast, LFP experiences phase separation (which will be explained in a subsequent section), wherein only a specific region of the particle is active for lithiation while the rest is inactive. Consequently, the voltage potential of LFP remains steady, reacting solely from the active region. While this steady voltage curve provides several advantages to manufacturers, they must adopt a different perspective when working with these materials to avoid confusion due to their new characteristics.

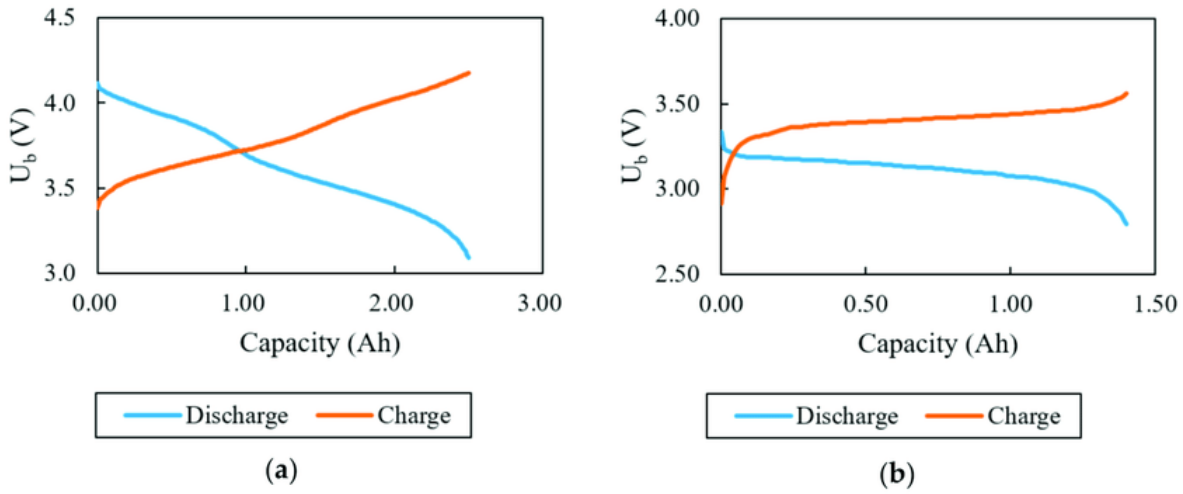

Figure 2.7: Battery discharge and charge curve for a)NCA and b)LFP [33] .

Regarding the safety aspect, NCA can reach a thermal runaway reaction at a lower temperature than LFP. Furthermore, the amount of heat that is released in NCA is almost 5 times bigger than that of lithium iron phosphate battery. The main reason is that the structure of NCA is unstable and allow oxygen to decompose which is a main ingredient of fire.
Last but not least, is the cycle life where the LFP is by far greater than NCA and this is the main reason why is so attractive for the new Tesla vehicles. The chemistry of this compound does not

allow to degrade so easily even in higher temperatures and provide the possibility of charging until 100% without any problem.

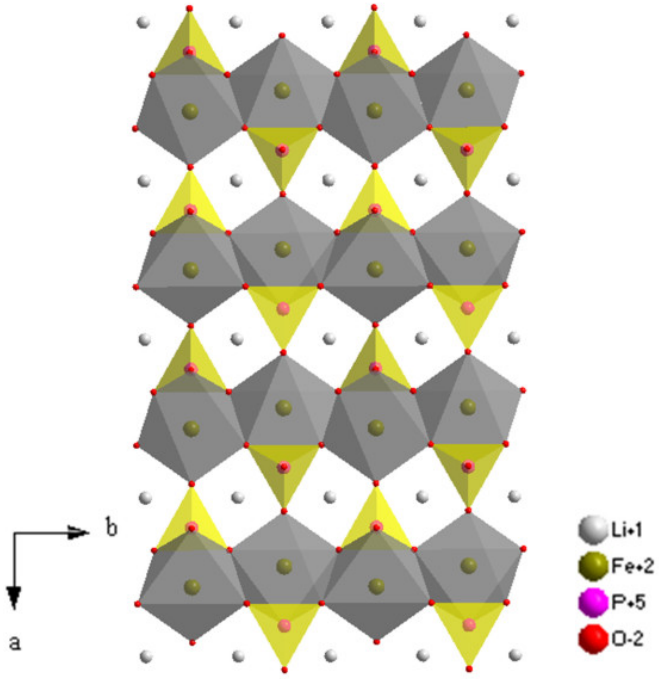

Figure 2.8: The crystal structure of LFP [14] .

2.6. Research Goals, Questions and Approach

1. **Research Goal:** The goal of this research is to compare MPET predictions with battery experimental results in different temperature ranges. The data should be analyzed so as to realize, in different cases, the possible starting point of a hotspot in a battery and , thus, to prevent the detrimental phenomenon of thermal runaway.

2. **Research Question 1:** How the experimental voltage curve and the simulated voltage curve are influenced by different temperature operation condition?
   Research Question 2: What is the effect on battery performance when varying the material and physical properties of the components?
   Subquestion: How is the active particle population influenced by the temperature variation?

3. **Research Approach:** The conduction of experiments in coin cells that are constructed in the battery lab of TU Delft is the first part of this research. Running simulation using MPET to compare the results is the second part of the research. Boundary conditions and physical input parameters play significant role to the outcome and should be carefully chosen. The outcome of this research using the isothermal MPET model can shed light on the impact of temperature on phase separation materials. Temperature is known to affect the kinetics of phase separation, but the exact impact is not known yet. Through experiments and phase field modelling, we can underscore the importance of accurately characterizing the effects of temperature on battery behavior. Furthermore, sensitivity analysis is a powerful tool for understanding the influence of different factors on battery performance. In particular, varying

particle sizes, thermal and electronic conductivity, and electrode thickness can have a significant impact on battery behavior, especially at critical temperatures. To perform a sensitivity analysis, one can systematically vary each parameter while holding the other parameters constant and observe the resulting changes in battery performance metrics, such as capacity, power, and efficiency. As a result, you can understand the dominant limitation and how to improve the construction of batteries so as to nullify this problem.

3

Methodology

This study aims to improve and validate a physics-based model for Li-ion batteries, focusing on the mesoscale within a continuum media framework, while accounting for the significant impact of phase separation within battery materials. The approach integrates conservation laws (balance equations) and transport equations (constitutive relations) to create a precise representation of Li-ion battery behavior. To achieve an accurate mesoscale model, microscale characteristics, including particle size and shape, are inferred using advanced image processing techniques, while maintaining computational efficiency as a priority. Nonetheless, due to the complexity, many commercial software solutions incorporate an artificial representation of the microstructure.
The description of microscale is based on transport phenomena. The electrolyte equations are categorized in dilute and moderate mixtures and the ion exchange equations are based on Butler-Volmer equation.Three different models will be explained so as to build the physics that will describe the operation of a battery.
This section consists of three parts. The electrolyte equations, the electrode equations and the boundary conditions. Furthermore, the DFN model is subdivided with the same manner. The last section is the description of multiphase porous electrode theory which is used in this study.
The methodology for constructing the computational model will be explained in this section, while the experimental procedures will be presented in a separate chapter. Starting from the microscale, we endeavor to derive the Doyle Fuller Newman (DFN) model, separating it into electrode and electrolyte equations. The structure of this section is similar to the following references about DFN ([7]) and MPET ([38]) models.

3.1. Microscale model-Electrolyte equations

The electrolyte is flowing from the current collector in the porous medium of the anode and the separator and reaches the cathode and the other current collector. Modelling the sites where the electrolyte is flowing, and assuming charge neutrality (the amount of positive and negative ions is equal) the following general **conservation** equations can be written:

$$\frac{\partial c_{i+}}{\partial t} = -\nabla N_{i+} \tag{3.1}$$

$$\frac{\partial \rho_{i+}}{\partial t} = -\nabla j_{i+} \tag{3.2}$$

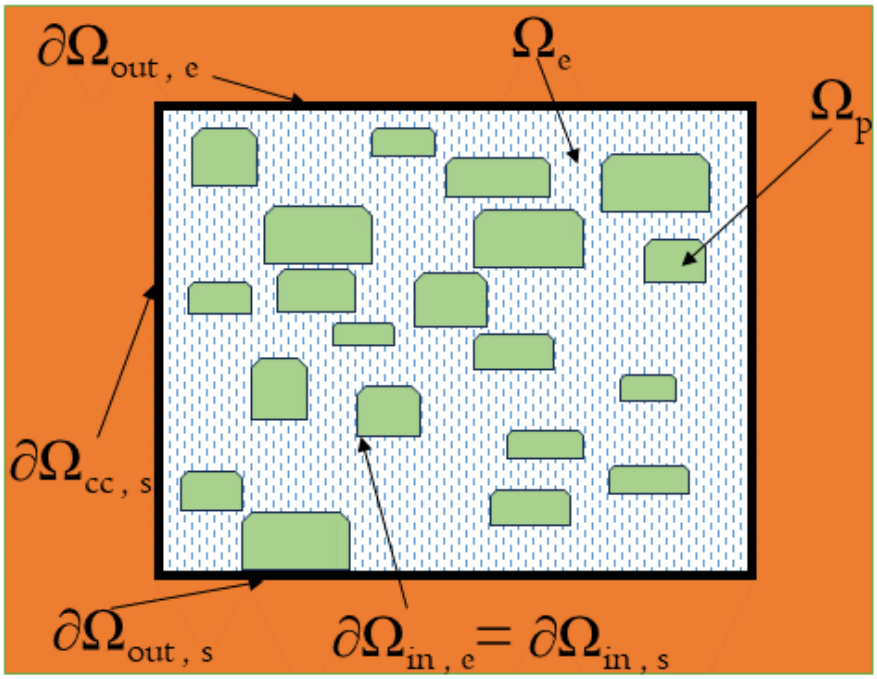

Figure 3.1: The computational domain of the microscale model in the electrode. The main domains are the electrolyte domain Ω_e and the solid material Ω_p. The primary distinction from the subsequent generalized models lies in the explicit delineation of boundary conditions for each domain. The subscript e is reffered to electrolyte, s to solid and cc to current collector.

The concentration c (mol/m^3) can be either the positive (i+) or the negative (i-) ion's concentration in the electrolyte, N_+ (mol/($m^2 \cdot s$) is the ionic flux, ρ (C/m^3) is the charge per cubic volume and j (C/($m^2 \cdot s$) is the current density[25] in the electrolyte.

The **constitutive** relations, the equations for the definitions of fluxes in the electrolyte, are categorized in two cases. Assuming dilute electrolytes, neglecting the interaction between the ions, but taking into account only the chemical potential gradient, the flux can be defined:

$$N_+ = -M_i c_i \nabla \mu_i \tag{3.3}$$

where M_i (m^2/(V s)) is the mobility from the Einstein equation and the chemical potential (μ) is defined as the summation of chemical and electrostatic contributions ($k_b T \ln \alpha_i + \mu_a + z_i e \phi$, where k_b is the Boltzmann constant, T (K) is the temperature, μ_a (J/mole) is the reference chemical potential and z_i is the amount of charge ions, α is the activity coefficient and ϕ(V) is the electrostatic potential).

From Nernst-Plank Theory and using the 3.3 and the chemical potential definition:

$$N_i = \underbrace{-D_i \nabla c_i}_{\text{Diffusion}} + \underbrace{c_i v_i}_{\textit{Advection}} + \underbrace{\frac{t_+}{F z_+} j_i}_{\textit{Electromigration}} \tag{3.4}$$

$$j_i = \underbrace{-\kappa \nabla \phi_i}_{\text{Ohm's Law}} - \underbrace{\kappa \frac{t_+}{F z_+} \frac{\partial \mu_i}{\partial c_i} \nabla c_i}_{\textit{Chemical potential gradient}} \tag{3.5}$$

,where the first term of 3.4 comes from the Fick's law, the second term is neglected in most cases and comes from the convective flux, and the last term represents the flux because of electrostatic interactions. D_i is the diffusion coefficient, v (m/s) is the velocity of ions, t_+ is the transference number and F is the Faraday constant. These equations are solved in the domain Ω_e.
In the equation 3.5, κ (S/m) is the ionic conductivity and ϕ_i is the electrolyte potential(V) with respect to lithium electrode. This equation comes from the difference between the ionic fluxes of the anions and cations(3.6).

$$j_{i+} = F(N_{i+} - N_{i-}) \tag{3.6}$$

Using equation 3.4 and 3.6, the final conservation equation is presented below.

$$\nabla j_{i+} = 0 \tag{3.7}$$

A more realistic model is the Stefan-Maxwell which also includes the interactions of all species, thus:

$$N_+ = -\sum U_{i,j} \nabla \mu_{i,j} \tag{3.8}$$

where $U_{i,j}$ is the direct and indirect coefficients. Not only the electrochemical but also friction forces between the ions are taken into account with this model. A more detailed derivation of the moderate electrolyte equations are presented in the following paper [35]. The coefficients in this model are a function of temperature and this is why in this study this model is implemented to investigate the power of the model in the dependence of the electrolyte to the operating temperature.

3.1.1. Microscale model-Electrode equations

The **conservation** equations that are used for the electrode (subscript el) domains are the same with the electrolyte equations but instead of ions, the concentration flux and charge flux of lithium inside the particle is calculated. This equation are solved in the solid domain of the particles and the binders of the conductive matrix. On the other hand, the **constitutive** relations are influenced only by the concentration and potential gradients.

$$N_{el} = -D_{el} \nabla c_{el} \tag{3.9}$$

$$i_{el} = -\sigma_{el} \nabla \phi_{el} \tag{3.10}$$

These equations are solved in the domain Ω_p. It is very important to realise that the diffusivity (D_{el}) and the conductivity (σ_{el}) are spatially dependent because of the different materials of the microstructure. Except from the anode and cathode material there are also carbon binders and Polyvinylidene fluoride(PVDF) which influence these values.

3.1.2. Microscale model-Boundary conditions

The interface between the solid particles and the electrolyte ($\partial\Omega_{in,e}$ and $\partial\Omega_{in,s}$) is solved through Butler-Volmer equation.

$$i_{el} = i_0 sinh(\frac{F}{2RT}\eta_{el}) \tag{3.11}$$

where i_0 is the exchange current density (Equation 2.9) and η_{el} is the overpotential (Equation 2.8). The current density is used in the boundary of the particles' surface. The sign (equation 3.12) depends on the direction of flux if it is from or to the electrolyte.

$$N_{el} \cdot \hat{n} = -i_{el} \tag{3.12}$$

Furthermore, the differentiation between the various domains should be elucidated. In the current collector a boundary condition is imposed as zero flux of lithium ions(equation 3.12) and two boundary conditions of potential description in the two current collectors (Li foil- $\phi_+ = 0V$, LFP- $\phi_- = V(t)V$ at $\partial\Omega_{cc,s}$ and $\partial\Omega_{cc,ss}$). No current can flow through the separator and outside of the particles that are in contact with the outer boundary ($\partial\Omega_{out,e}$ and $\partial\Omega_{out,s}$, equation 3.13 and 3.12). The last initial conditions are the concentration of active material in anode and cathode and the concentration of the electrolyte ($c_s = c_{s,0}, c_e = c_{e,0}$ at t=0).

$$i_i \cdot \hat{n} = 0 \tag{3.13}$$

3.1.3. Microscale model-Main points

The variables that are calculated in this model are the lithium ion concentration, the electrolyte potential, the flux of lithium ions and the current density. Diffusion coefficient and ionic conductivity are spatially and thermally dependent and this is difficult to couple it. The chemical potential should be defined as a function of temperature and concentration. The ideal theory is used for this definition which can not capture the phase separation.

3.2. Doyle Fuller Newman model

In this model, the representation of distinct domains is presented as a continuum. It is a pseudo-2D model, and equations are volume-averaged equations, obtained through the differentiation of conservation laws, and utilizing effective properties instead of discrete values of diffusivities and conductivities, which are based on the specific material and domain. To describe the intercalation process within the particles, the assumption of spherical particle shapes is adopted, and a 1D spherical conservation equation is utilized (figure 3.2). The electrodes and the separator also are assumed as planar geometries which decreases the computational time and the complexity of the problem.

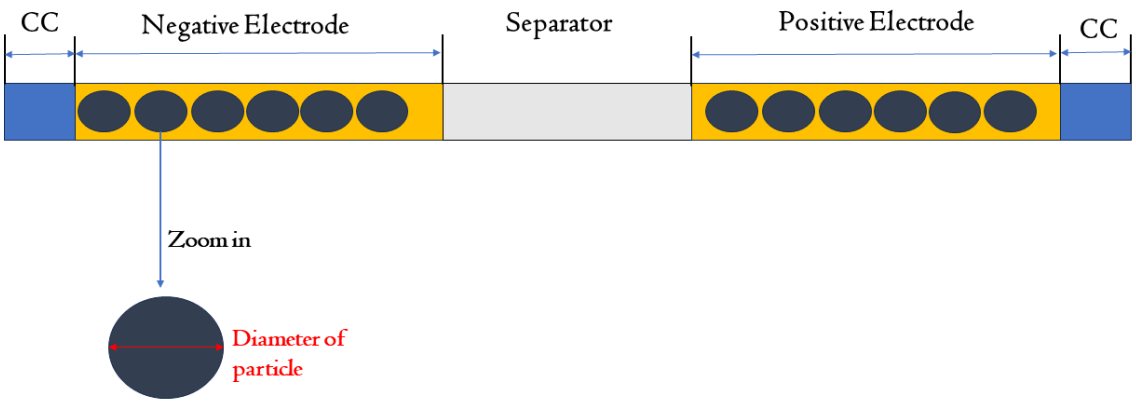

Figure 3.2: The computational domain of the DFN model.

3.2.1. Volume - averaged equations

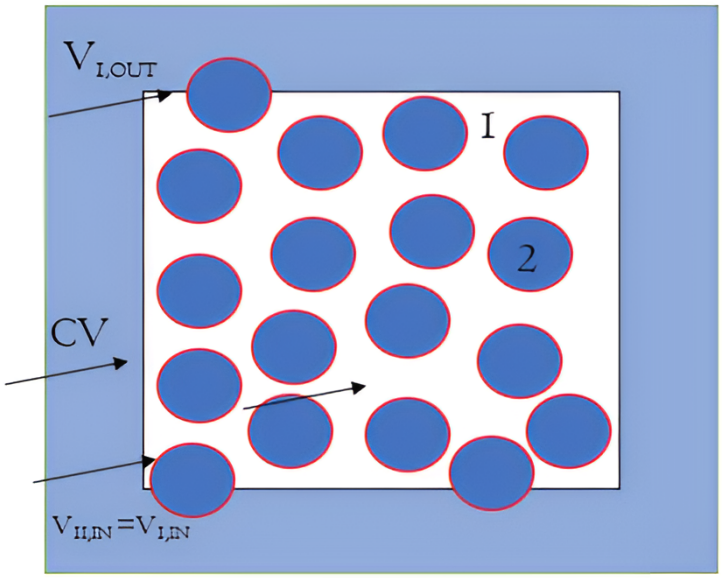

Figure 3.3: The control volume in a general volume averaged domain .

This technique discretizes the domain in finite volumes and because of the coexistence of two different phases, averages the equations according to the specific finite volume as figure 3.3. The equa-

tions are the same with the equation of electrodes equations in the previous section. The only difference is that here the fluxes represent averaged macroscale fluxes. With reference of figure 3.3, the conservation equations for the different phases(solid and liquid) can be expressed.

$$\frac{\partial c_1}{\partial t} = -(\frac{1}{V_1}\int_{V_{1,in}} \nabla N_1 \cdot \hat{n} ds + \frac{1}{V_1}\int_{V_{1,out}} \nabla N_1 \cdot \hat{n} ds) \tag{3.14}$$

the same equation can be written for the second phase. Summing the two equations:

$$\frac{\partial c_{tot}}{\partial t} = -(\frac{1}{V_{tot}}\int_{V_{1,out}} \nabla N_1 \cdot \hat{n} ds + \frac{1}{V_{tot}}\int_{V_{2,out}} \nabla N_2 \cdot \hat{n} ds) \tag{3.15}$$

The constitutive equation is equation 3.3 but replacing all the discrete properties with effective ones. (effective diffusion coefficient, effective mobility). By utilizing all the equations mentioned earlier, it becomes possible to determine all the parameters for each phase. The comprehensive set of equations, including the conservation laws, transport equations, and the Butler-Volmer equation for ion exchange, enables us to establish a complete description of the system's behavior. Through this approach, we can extract the necessary parameters for both the electrolyte and electrode phases, obtaining a comprehensive understanding of the Li-ion battery's performance and characteristics. Regarding the electrode, the charge conservation and the ohm's law ,modified in the same manner as above, can express the conservation equations of this scale. The main difference with equation 3.2 is the insertion of a term b_i which expresses the surface area per unit volume of particles in contact with the electrolyte. The same procedure is followed for the electrolyte equations. Below, all the equations and boundary conditions are presented. In the electrolyte model except from b_i, there is a coefficient (B_i) which is the transport efficiency based on the domain that is being calculated. The tortuosity (τ) is also given by using the Bruggerman relation.

3.2.2. Equations of DFN model

Particle equations

Conservation equation:

$$\frac{\partial c_p}{\partial t} + \frac{1}{r^2}\frac{\partial (r^2 N_p)}{\partial r} = 0 \tag{3.16}$$

Constitutive relation:

$$N_p = -D_p \frac{\partial c_p}{\partial r} \tag{3.17}$$

Boundary (and initial) conditions:

$$N_p = 0, r = 0$$

$$c_p = c_0, t = 0$$

$$N_p = i_p/F, r = R_p$$

Electrode equations

Conservation equation:

$$\frac{\partial j_{el}}{\partial x} = -b_{el} i_p \tag{3.18}$$

Constitutive relation:

$$j_{el} = -\sigma_{el} \frac{\partial \phi_{el}}{\partial x} \tag{3.19}$$

Boundary conditions:

$$\phi_{el} = 0, x = 0$$

$$j_{el} = 0, x = L_n$$

$$j_{el} = 0, x = L_p - L_n$$

Electrolyte equations

Conservation equation:

$$\epsilon(x) \frac{\partial c_{i+}}{\partial t} = -\nabla N_{i+} + \frac{b(x) i_p(x)}{F} \tag{3.20}$$

and equation 3.18.
Constitutive relation:

$$N_i = -D_i(x) B(x) \nabla c_i + c_i v_i + \frac{t_+}{F z_+} j_{el} \tag{3.21}$$

and equation 3.5.
Boundary conditions:

$$j_{el} = 0$$

and

$$N_{el} = 0, x = L$$

$$j_{el} = 0$$

and

$$N_{el} = 0, x = 0$$

$$c_{el} = c_{el,0}, t = 0$$

Table 3.1: DFN model Symbols

Symbols	Description	Domain
c_p	Li-ion concentration(mol/m^3)	Particle
N_p	Diffusive ion flux(mol/(m^{2}s)	Particle
i_p	interfacial current density(A/m^2)	Particle
j_{el}	av. macr. current density(A/m^2)	Electrode
σ_{el}	eff. electronic conductivity(S/m)	Electrode
b_{el}	$\frac{surf.}{vol.}$ of particles with electrolyte	Electrode
$c_{el,0}$	initial Li-ion concentration in electrolyte	electrolyte

Many symbols that are used in the above equations have not been explained thoroughly, thus, a summary table is shown and in the next section the main differences will be highlighted between this model and the MPET model and all the domains will be visualised.

3.3. MPET model

The Multiphase Porous Electrode Theory (MPET) comes from the Porous Electrode Theory by John Newmann with some strong differences. The open circuit potential comes from non-equilibrium thermodynamics to capture phenomena like phase separation (See chapter 2). Different models which explain the behavior of the particles will be presented below to understand the limit of solid solution and phase separation. Volume averaging theory fails to describe phenomena like the deformation inside the particles during intercalation and different concentration fields without the correct formulation in the particles' equations, thus DFN model is not capable of doing it. On the other hand, a complete interpretation of the microstructure is computationally inefficient. Here comes this software which **approach the heterogenities in particles with defining the free energy functional.** This section is separated in two subsections: the particle scale and the electrode-electrolyte scale because the equations are coupled and are easier to comprehend the interaction between the solid material and the electrolyte.

3.3.1. Computational Domain and Particle equations

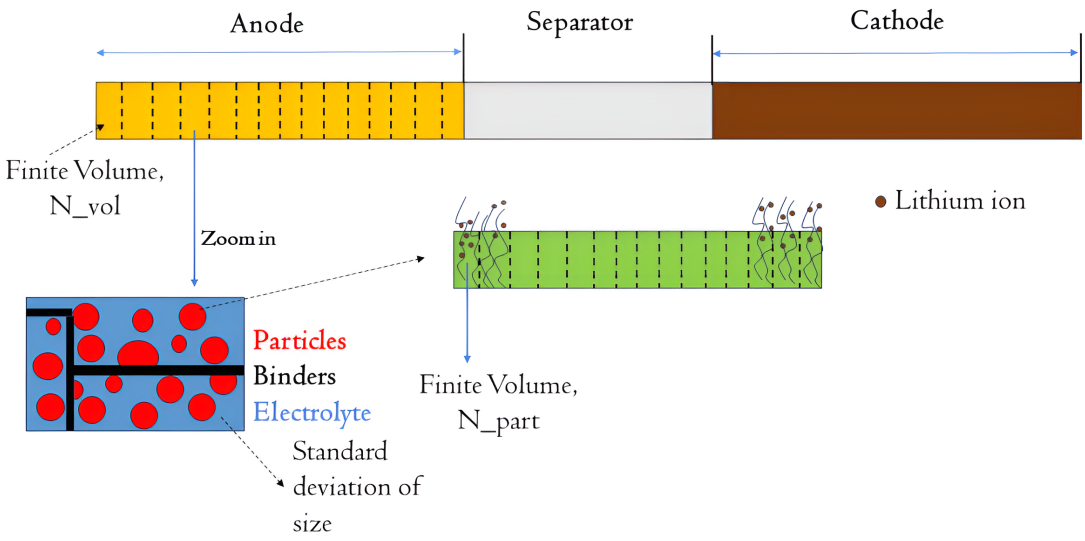

Figure 3.4: Computational domain in MPET model.

The simulation uses the finite volume method to solve the differential algebraic equations (DAE) and also involves volume averaged methods but the particles are solved in their own scale and after are treated as sources or sinks in the bigger scale (same with the DFN model).

3.3.2. Electrode - Electrolyte equations

Based on the conservation of species and conservation of charge(See section 3.1) the conservation laws for the electrolyte in the electrodes can be expressed with equation 3.22 and 3.23.The reaction rate R is equal to zero in the separator and thus the same equations describe the mass and charge conservation for the electrolyte in all the battery domain by just neglecting this term. The j_{i+} is calculated from equation 3.5 and the ionic flux from the Stefan-Maxwell equation (Constitutive relations).

$$\frac{\partial(\epsilon(x)c_{i+})}{\partial t} = -\nabla N_{i+} + R_{V,i} \tag{3.22}$$

$$\sum z_i e R_{V,i} = \nabla j_{i+} \tag{3.23}$$

The following figures summarize the aforementioned equations, field variables and some boundary conditions of electrolyte in the separator and electrode.

The noteworthy point that is not mentioned before is that the ionic conductivity in the constitutive equation of the current density is calculated through the research of Valoen and Bernardi in the following paper [42]. The dependence of electrolyte on temperature is being described through this research which shows the high importance in our study as well.

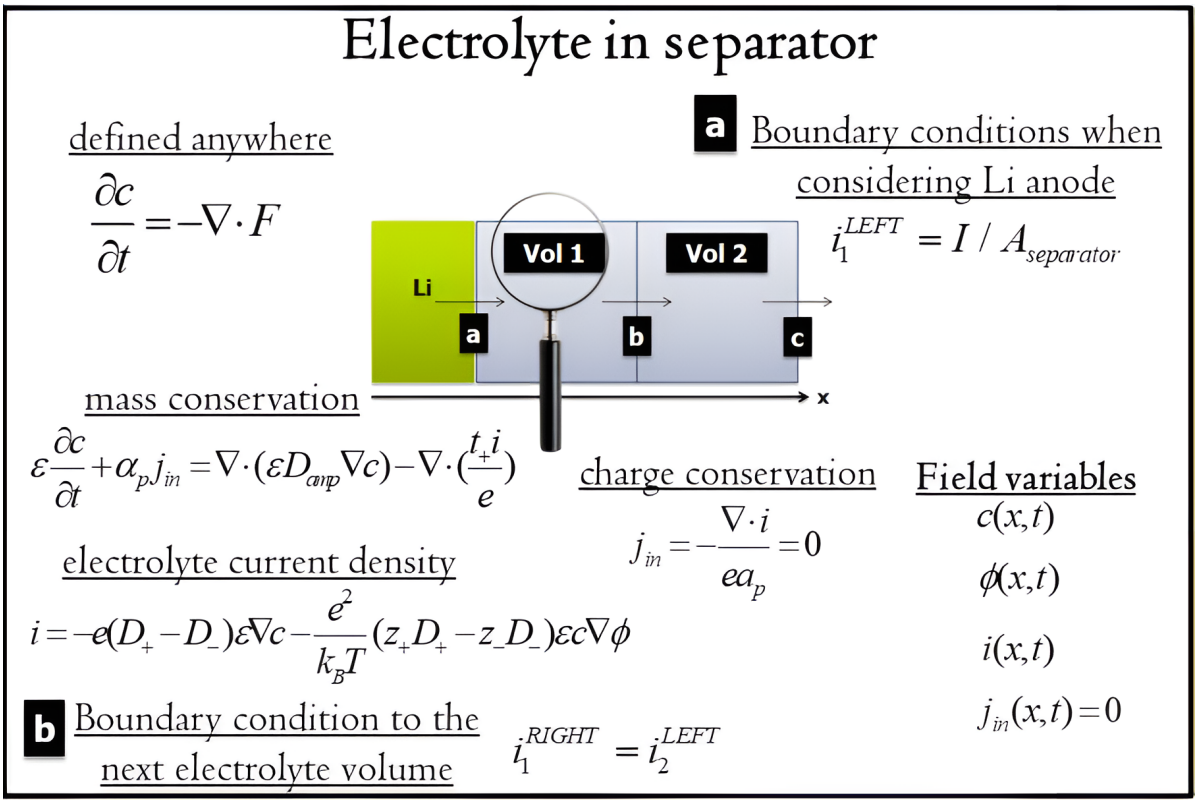

Figure 3.5: Electrolyte equations in separator.

For the ionic flux, the definition of chemical potential for a given ion should be presented.

$$\mu_{l,i} = \kappa_b T ln(\alpha_{l,i}) + \mu_{l,i_{eq}} + z_i e \phi_{l,i} \tag{3.24}$$

where κ_b is the Boltzmann constant, T(K) is the temperature ,$\alpha_{l,i}$ is the activity of species and $\mu_{l,i_{eq}}$ is the reference chemical potential. This definition takes into account both the electrostatic and chemical contributions.

Regarding the solid phase, the electrode equations have been mentioned in the previous sections (equations 3.18 and 3.19). The adding value of MPET is that the particle interaction can be both parallel (in the same finite volume) and serially through the electrode. The conductance between particles in a finite volume captures a more realistic behavior about the connection of the particles and plays a significant role in this study (figure 3.7). Using the Ohm's law and the charge conservation, the current per volume is separated in the particles in the following manner.

$$G_{j,k}(\phi_{j,k} - \phi_{j,k+1}) = I_{j,k} \tag{3.25}$$

$$I_{j,k} - I_{j,k+1} = \int_{A_{k+1}} j_{j,k+1} dA \tag{3.26}$$

where $G_{j,k}$ is the conductance and $I_{j,k}$ is the current between the particles.

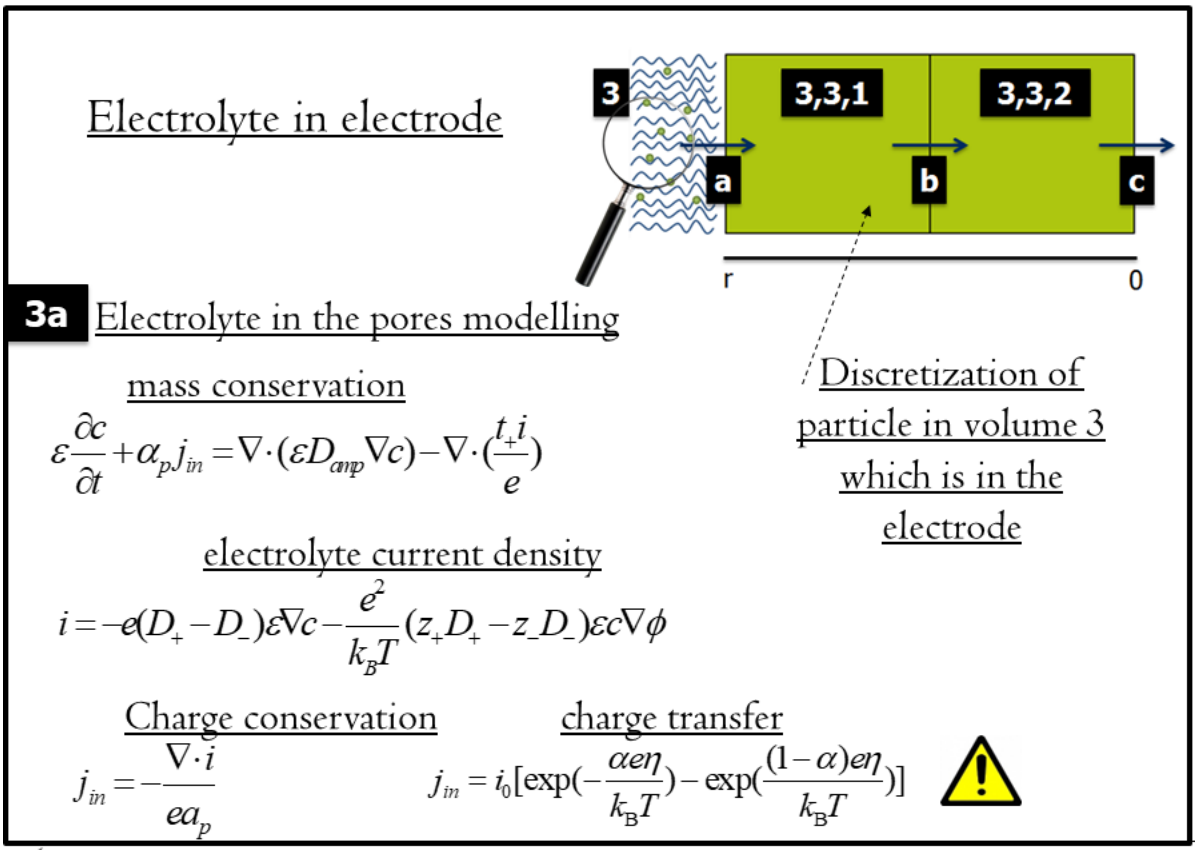

Figure 3.6: Electrolyte equations in electrode.

Boundary Conditions

The conservation equations and the constitutive relations will be solved only for anions because is more convenient, thus there are four first-order differential equations and you need four boundary conditions.

$$\nabla N_{el} = 0, \text{ at x=0 , x=L}$$

$$\nabla i_{el} = 0 \text{ at x=0 , x=L}$$

3.3.3. Particle equations

The particle section has two parts. The solid dynamics of the particles and electrochemical reaction section. The electrochemical section in our study, is referred to the Butler-Volmer equation which is described in the previous sections. The overpotential and the exchange current density is expressed with respect to the activities which are connected to the Gibbs free energy.

Solid dynamics

The calculation of the solid dynamics of a particle as can be seen from figure 3.8, needs the definition of the chemical potential from the regular solution theory. The chemical potential is the functional derivative of the total Gibbs free energy. Thus, the definition of Gibbs free energy is the new feature of this model which incorporates the free energy and the surface energy.

$$G = \int_{V_p} g dV + \int_{A_p} \gamma_\sigma dA \tag{3.27}$$

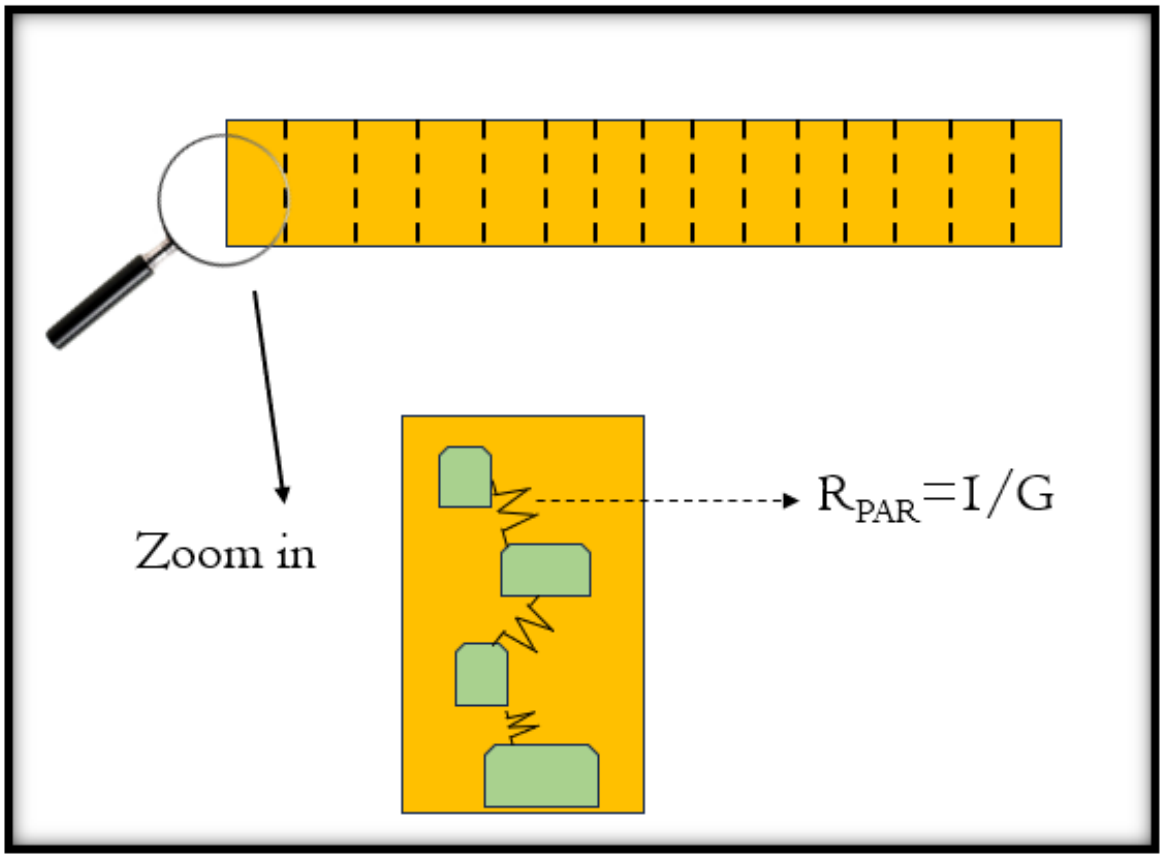

Figure 3.7: This figure shows that the particles are connected in series and electrons should flow in the conductive matrix(resistances) creating a voltage drop in particle by particle interaction.

g corresponds to the homogeneous (equation 2.16) and non-homogeneous gibbs free energy density. Using the Cahn-Hillard thermodynamic model, the phase separation can be described by the non-homegeneous gibbs free energy by the equation below.

$$g_{nh} = \frac{1}{2(c_{s,ref})^2} \nabla c_i \kappa \nabla c_i \tag{3.28}$$

where κ is the gradient penalty tensor and $c_{s,ref}$ is the a suitable concentration scale

The Allen-Cahn conservation equation used for LFP as proposed by Bazant, which neglects transport in the y-axis of the particle and the local rate of concentration can be calculated by :

$$\frac{\partial c_{av}}{\partial t} = \frac{A_p}{V_p} j_p(r) \tag{3.29}$$

In figure 3.8 a summary of two different particle solid dynamics are presented. It is important to realise that the Allen-Cahn model is characterized as reaction limited model instead of Cahn-Hillard as diffusion limited model. This is explained also from the equation in the figure but also from the domain visualization. In LFP, according to experimental outcomes, the y-axis diffusion is infinitely

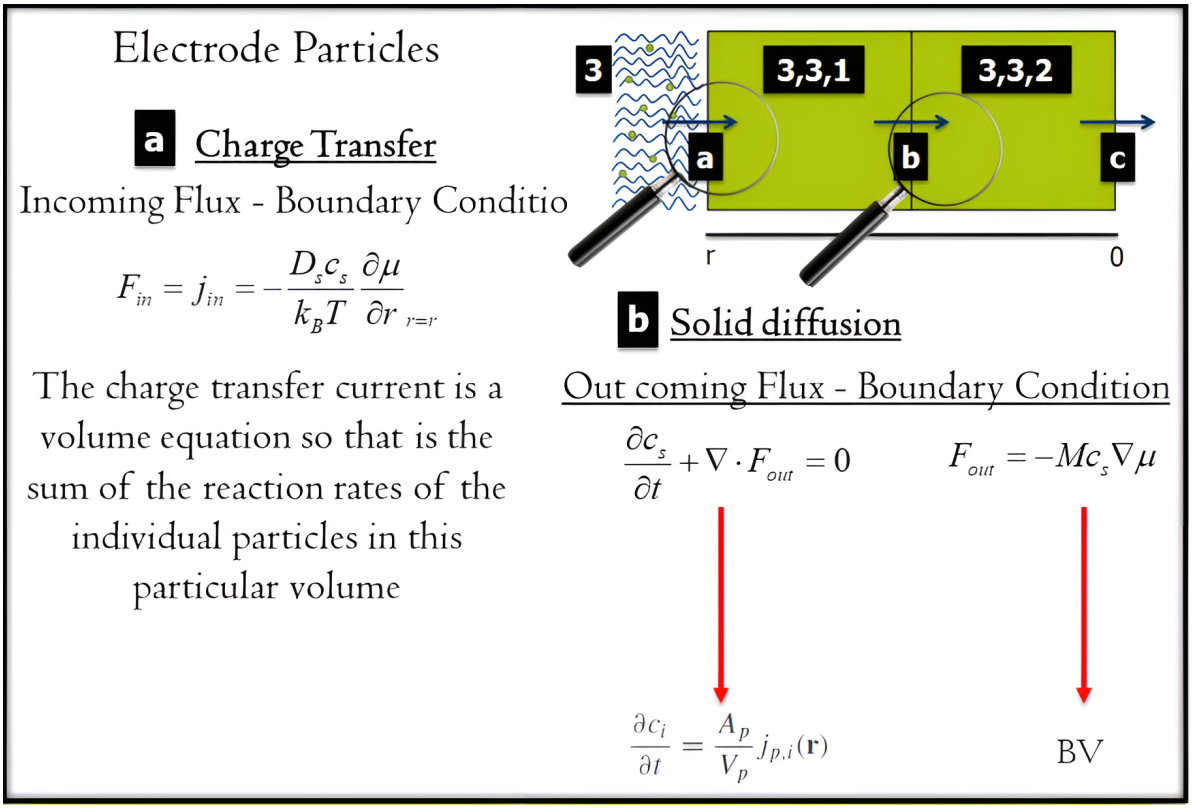

Figure 3.8: Particle discretization and summary of the equations .

fast so the reaction controls the intercalation of the lithium ions, but for example, in Lithium titanium oxide(LTO) the diffusion equation controls the model. The phase separation in LFP can be observed in x-axis as is illustrated in figure 3.9. The constitutive relation is the same as in the previous sections about the particles.

Boundary conditions

Taking into account only one of the conservation equations (eq.3.29) and its constitutive relation, two boundary conditions should be provided.

$$\hat{n} \cdot N_p = -j_p, \text{ at x=R}$$

$$\hat{n}\frac{\partial g}{\partial \nabla c_p} = \hat{n}\frac{\partial \gamma_s}{\partial c_p}, \text{ at x=R}$$

For easier convergence the dimensionless concentation in the sides of the particles is 0.98.

3.3.4. Length scale coupling

The different length scales are coupled by the electrochemical reaction equations. After the calculation of the rate of change of concentration in a particle (equation 3.29), the volumetric reaction rate $R_{v,i}$ is the summation of all the particles multiplied by the active material percentage. The total current density per electrode area is calculated as the summation of all the volumetric reaction rates.

$$i_{cell} = -\sum \int_{L_c} z_i e R_{V,i} dL \tag{3.30}$$

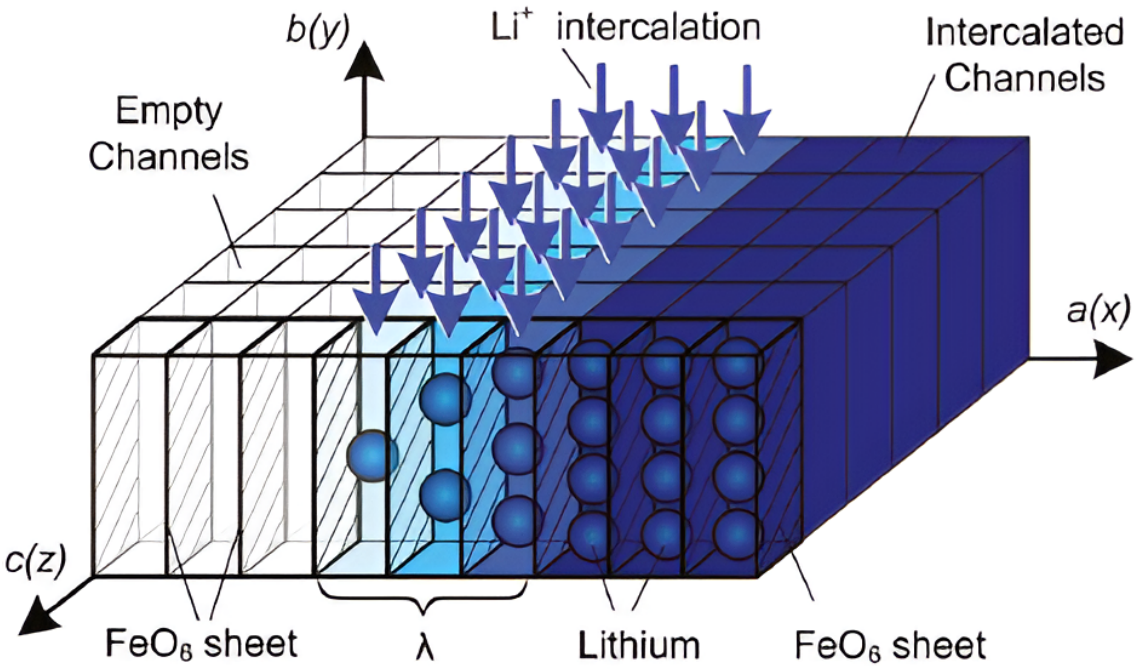

Figure 3.9: The intercalation loss of Li^+ in the y-axis is assumed to be neglected. The phase separation in a particle can be in a(x) axis as the finite volumes are completely empty in the beginning of the axis and in the end of the axis are completely lithiated [19].

Finally the overall cell voltage is calculated through the following equation:

$$\Delta\phi_{cell} = \Delta\phi_{app} - i_{cell}R_{ser} \tag{3.31}$$

3.3.5. Assumptions and limitations

One of the main limitations of this software is that every finite volume should include at least one particle in order to be able to capture the phase separating behavior with high accuracy. Furthermore, electroneutrality of the electrolyte and the non-existence of the pseudo-capacitance phenomenon are reasonable assumptions in battery modelling but a future version of MPET can inculde these characteristics. Another mechanism that is missing is the deformation stresses during intercalation that can occur.

One major limitation is the isothermal condition. Generation and transport of heat is implemented in MPET in 2023 but the accuracy of this new model has not been validated yet. The dependence in temperature is the main outline of this study but the heat production validation can be a future research. The two last limitations are the particles' geometry and the degradation modelling. The particles can be simulated as spheres or rectangles and the degradation does not play a role in the current version of MPET. The temperature dependence of degradation in experimental studies is known, thus this extension is of high importance.

3.3.6. Choice of Parameters

In our study, the anode is lithium foil, thus the cathode is only simulated. All the particles assume to be in a perfect bath of electrolyte. The parameters that have not been calculated or measured experimentally are the electronic conductivity of the cathode material, the Bruggerman exponent,

the particles' conductivity, the rate constant and the particle size. The electronic conductivity was sourced from the existing literature and also finds application in an open-source battery simulation package named Pybamm, developed in Python. Meanwhile, the determination of the Bruggerman exponent adopts a unique approach, as showcased in figure 3.11. This approach diverges from the conventional Bruggerman relation. Instead, it draws on experimental data for LFP with low carbon loading, a parallel that resonates with our research, thereby establishing a distinct relationship. The particle size can be measured experimentally (but because of the time limitation a mean size was chosen and a big standard deviation of the size can represent the different particles as can be seen in figure 3.10). This is a strong assumption which helps the simulation to capture the same behavior with the experiments and the influence of this parameter is also presented in the results section.

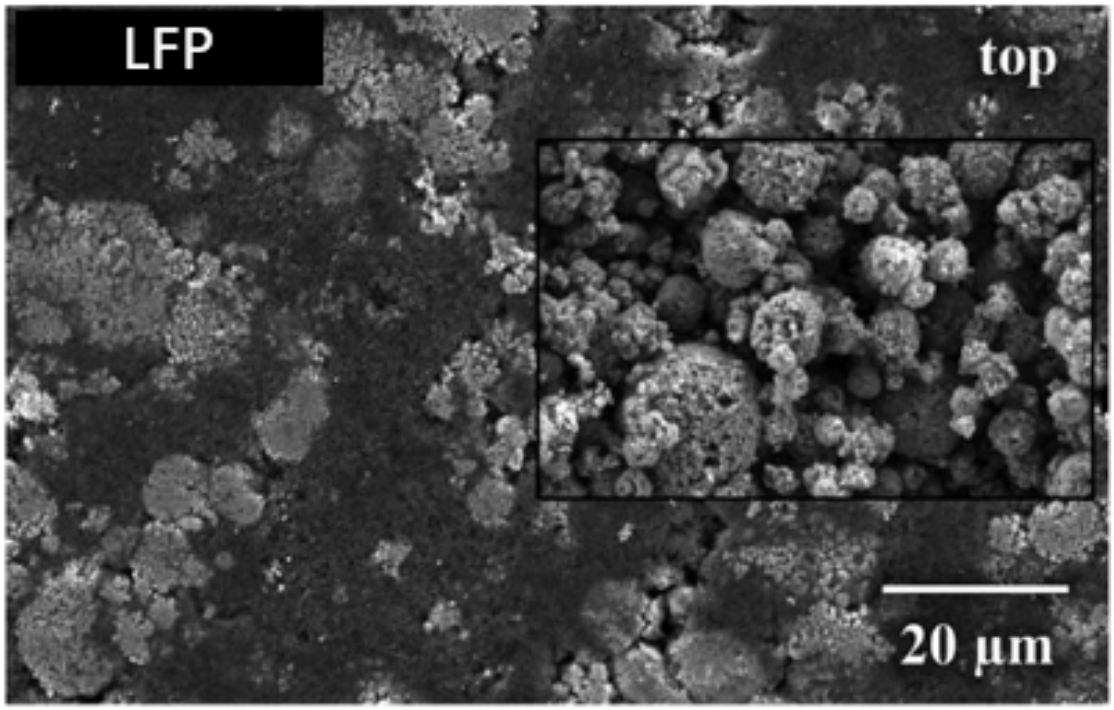

Figure 3.10: Image of the microstructure of an LFP cathode material. The particle size can vary a lot and this explains the choice of a high standard deviation[23].

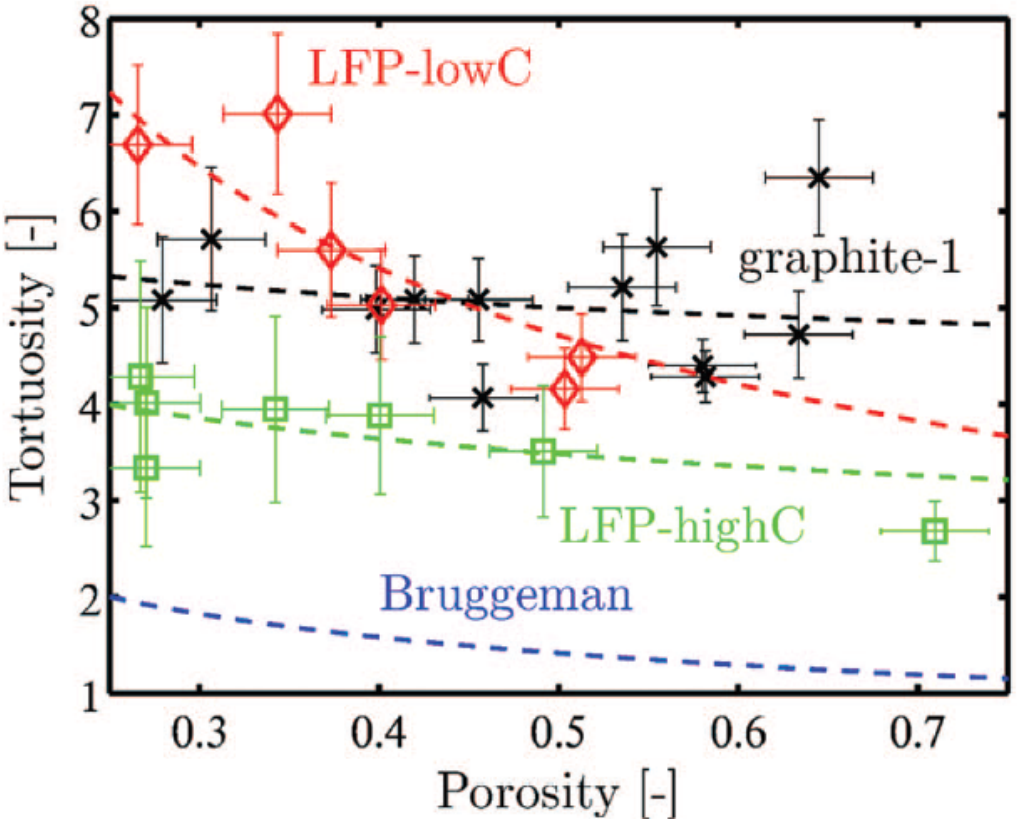

Figure 3.11: The tortuosity of 70% and 90% active material of LFP are presented in the figure by Landesfeind [23]. The comparison of Bruggerman for spherical particles is also depicted by the blue dashed line. This figure explains the choice of the value of Bruggerman exponent.

Table 3.2: Parameters

Physical Input Parameters	Value(Range)	Based on
Profile type	Constant current	-
Heat generation	Isothermal	-
C-Rate	vary	-
V_{max}	4 (V)	OCV
V_{min}	2.5 (V)	Cut-off Voltage
Temperature	268-323 (K)	case
Electronic conductivity (σ,Ohm's law)	0.34 (S/m)	Prada2013 model(PyBAMM)
Electronic conductivity in particles (G_c)	$0.34e^{-13}$ - $10.0e^{-13}$(S)	case
Standard deviation of G_c	$0.34e^{-14}$ - $10.0e^{-14}$(S)	case
Initial electrolyte concentration (c_0)	1000(mol/m^3)	initial condition
Electrolyte model	SM(Stefan-Maxwell)	temperature dependence
Electrolyte coefficients	valoen-bernardi	paper[42]
Neg.ion diffusion coefficient	D_n=2.94e-10 (m^2/s)	literature
Pos.ion diffusion coefficient	D_p=2.2e-10 (m^2/s)	literature

Table 3.3: Parameters

Design Input Parameters	Value(Range)	Based on
Particle size	$30e^{-9}$ (m)	-
Standard deviation of particle size	$100e^{-9}$ (m)	-
Length of electrode	$80e^{-6}$ (m)	measurement
Length of separator	$25e^{-6}$ (m)	measurement
Volume loading of active material	93%	calculation
cathode porosity	56%	calculation
seperator porosity	55%	literature [43]
Bruggerman exponent of cathode	-2	literature [23]

Table 3.4: Material Parameters

Material Parameters	Value(Range)	Source
Type	Allen-Cahn	Literature
Shape	C3	Literature
Ω	$1.8560e^{-20}$	experiments(literature)
gradient energy(κ)	$5.01481e^{-10}$	experiments(literature)
Reaction Type	Butler-Volmer	-
k_0	0.01-0.2	case
α	0.5 (symmetric)	-

Table 3.5: Computational Parameters

Computational Parameters	Value(Range)	Source
Particle's discretization	$2e^{-9}$ (m)	choice
Volume's discretization	$1.5e^{-6}$ (m)	choice
time steps	200	choice
tolerance	$1.0e^{-10}$	choice

3.4. Parameter Estimation

The first goal of this study is to validate the accuracy of the software compared to experimental results. In order to do so, the input parameters should be defined. There are different ways to estimate some parameters which are unknown because they can not be measured experimentally or vary in a very big range for similar cases. The two most powerful is machine learning or optimization algorithms.

During this study, both methods were investigated. Three different regression machine learning algorithms were implemented(Polynomial Regression , Support Vector Machine, Random Forest Regression). The first and simplest model that was implemented was the **Polynomial Regression Machine learning (ML) model.** This model is based on the least squares and tries to create a relationship between the input data to the output data. Ordinary least squares is the minimization of the sum of squares of the differences between the observed dependent variable in the given dataset and those predicted by the function. The model encompasses numerous input features and aims to establish distinct relationships for each output variable. However, the pronounced nonlinearity observed in the rate constant, as evident from the results section, renders this model unsuitable for accurate representation.

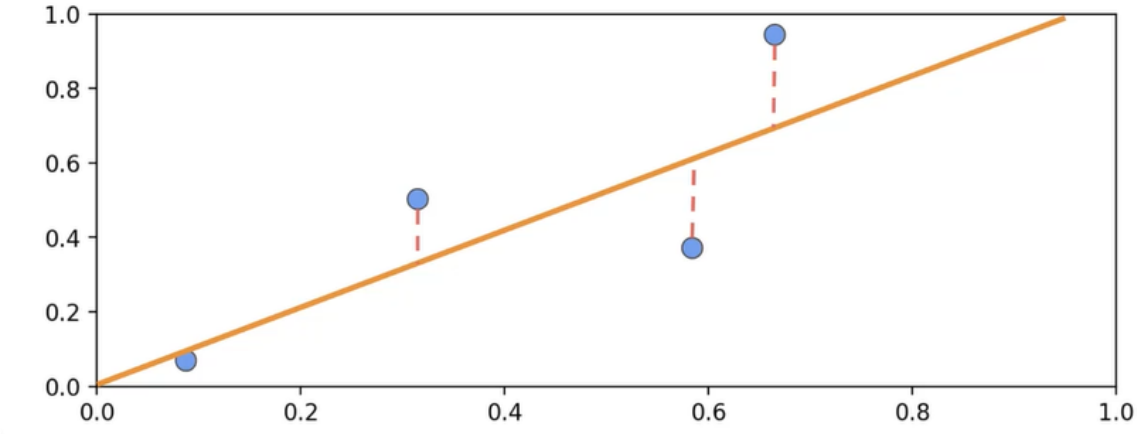

Figure 3.12: Visualisation of squared error in a linear regression problem.

The second model that tested was the **Support Vector Machine model.** Central to the approach is the utilization of hyperplanes to create distinct classes between the outcomes. Whether applied to classification or regression challenges, the establishment of a maximum margin classifier is imperative for finding diverse solutions. However, this paradigm creates ambiguity applied to continuous functions, such as in our scenario, especially in the presence of highly nonlinear parameters, like the rate constant. It's worth emphasizing that despite these complexities, the particles' and electrical conductivity could be successfully ascertained, exhibiting an error margin of approximately 8%.

The most efficient Machine learning model which also gave the motivation for the Monte Carlo approach was the **Random Forest Regression.** It based on a decision tree form by using statistical modeling where the node splits are decided based on an information metric. The core principle revolves around separating the input features and examining the outcomes associated with each subset resulting from this division. These outcomes can be categorized as either true or false. In instances where the outcome is false, a decision tree construction process continues, offering a variety of potential results. Ultimately, by interlinking all conceivable outcomes, a continuous function materializes, effectively representing the output variable. The separation of the input features

is based on Gini impurity. Avoiding the mathematic formulation, the intuition is how pure the different classes are. The lower the value of Gini impurity, the less mixing between the classes and the split leads to more homogeneous subsets and improved classification accuracy. Decision tree algorithms, like CART (Classification and Regression Trees), often use Gini impurity as a criterion for evaluating splits and growing the tree. This random splitting reaches to very accurate results for the conductivity parameters close to 2% and close to 10% for the rate constant.
Before continuing to the optimization algorithms, the main steps in a machine learning model should be noted.

1. Begin by reading the dataset and applying normalization to ensure that all features are scaled within the range of 0 to 1.
2. Divide the data into two subsets: the training dataset, which will be used to train the model, and the test dataset, which will be employed to assess the model's performance. Ensuring no interaction between these subsets is crucial to prevent any data leakage. Typically, the default separation allocates 70% of the input data to the training subset, with the remaining 30% forming the test subset.
3. Each machine learning model has its own set of specific parameters that must be defined when utilizing Python libraries. These parameters include aspects like maximum iterations, optimization method (e.g., gradient descent), polynomial degree (e.g., 2nd or 3rd degree), and learning rate. Defining these parameters accurately is pivotal in achieving optimal model performance.
4. Different performance metrics can be used as the mean squared error or the standard deviation of the solution for the post processing of the results.

The parameter identification using optimization algorithms is a very famous and especially in the battery community where many parameters can not be found experimentally. The first step is to construct the **estimator**.

$$\hat{\phi} = arg(min(F(\phi))) \tag{3.32}$$

where F is the objective function that needs to be minimised and $\hat{\phi}$ is the input argument (can be a vector). The most common, and also in this study, objective function is the mean root least squares equation.

$$F(\phi) = mean(\sum \sqrt{(V_{i,exp} - V_{i,sim}(\hat{\phi}))^2}) \tag{3.33}$$

The main problem of optimization of battery parameters is the convexity of a function. The convex problems have the advantage that any local minimum is also a global minimum, which is not the case for the non-convex problems. There are many different categories in optimization algorithms. The basic argument is if the method is based on the derivative of the objective function. The basic principle is that starting from a specific point within the parameter space, a gradual progression is made by moving in a direction that diminishes the cost function. This progression is guided by insights into the gradient and occasionally even the curvature of the function [3].

In this study a derivative-based method is partially implemented. Starting with a good initial guess, the goal is the decrease of the objective function as you iteratively change the parameters' values (ϕ). For the direction of your next iteration, the condition that should be fulfilled is presented

in equation 3.34. The vector $\hat{p}$ should be chosen so as the derivative of the objective function will decrease. Equation 3.35 is the condition for the step size where c_1 is between 0 and 1 and α is the step value. There are many different ways to calculate the step length and the descent direction which is not the scope of this study. Last step is the update of parameters' vectors and the check of the convergence criterion until you reach a minimum threshold. This method is called line-search method.

$$\nabla(F(\hat{\phi}))^T \hat{p} < 0 \tag{3.34}$$

$$F(x_{new}) \leq F(0) + \alpha c_1 \frac{\partial F(0)}{\partial x} \tag{3.35}$$

In this study a combination of the Monte-Carlo(MC) approach and the line-search method was implemented. The MC approach is a computational technique which includes a massive amount of simulations based on the law of large numbers and you approximate the solution of the minimization of the objective function. The randomness of the simulations gives an overview of the possible outcomes that can be established. The results based on statistical probabilities but the sample size plays an important role (law of large numbers). The descent direction and the step size of the different simulations are decided by the aforementioned line-search method. Running different samples of simulations, choosing every time the three best local minima solutions and running again in the vicinity of these solutions is the main methodology of our approach. This procedure did not guarantee the finding of the global minima but a very good approach of the optimization.

4

Experiments

The upcoming chapters will detail the primary methodology applied in the experimental section. The initial section will outline the preparation process for the components utilized in the experiments. Subsequently, a comprehensive account of the experimental procedure will be presented, along with the derivation of key assumptions. Towards the conclusion of the chapter, the experimental results will be discussed and explained in-depth, providing a thorough analysis of the outcomes.

4.1. Pretreatment and preparation of the components

The initial phase encompasses the collection of all requisite components, followed by appropriate processing. The assembly of a coin cell transpires within a glovebox, shielding the battery from environmental influences. Due to lithium's strong reactivity with oxygen and moisture, mitigation against their presence remains essential to avert unfavorable reactions. Additionally, the glovebox environment filters out airborne impurities that might otherwise compromise battery performance during assembly. The assembly steps are as follows:

1. **The separator and the LFP cathode electrode are precisely cut to their required dimensions using the Celgard 2500 as the separator, a widely used component in both experimental and modeling studies.** Figure 5.3 illustrates the tool employed for shaping the separator and the electrode. For comprehensive information on the dimensions and properties of the components, please refer to Table 4.1.

Figure 4.1: Tool for the circular shape of the separator with diameter of 19mm. A similar tool with diameter 12.77mm was used for the LFP cathode electrode.

2. **The various components are carefully arranged inside a dry vacuum chamber.** This specialized chamber is constructed using robust materials, such as stainless steel or glass, to withstand the low-pressure conditions. The process of degassing the battery components (as depicted in Figure 4.2) is essential to eliminate any potential air gases and bubbles. The chamber operates at a temperature of $80°C$ and a pressure 1 bar lower than atmospheric pressure . It is crucial for the components to remain inside the chamber for a minimum of 12 hours before they are transferred to the glove box. This precautionary step ensures that the components are thoroughly degassed and prepared for further assembly without any unwanted gas interference.

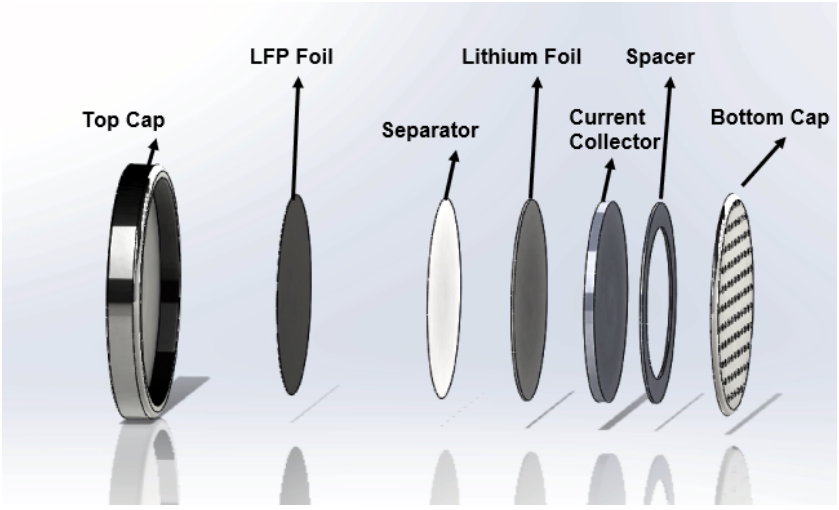

Figure 4.2: Explode-view of the battery coin cell

Figure 4.3: Dry vacuum chamber for degassing the components of the batteries.

3. **The assembly of the battery is conducted in the glovebox (Figure 4.4b) before starting the electrochemical cycling.** The only component which is not visible in Figure 4.2 is the electrolyte (Figure 4.4a) which is being absorbed by the separator during the manufacturing of the battery by using an adjustable pipette. The amount of electrolyte is 80μL.

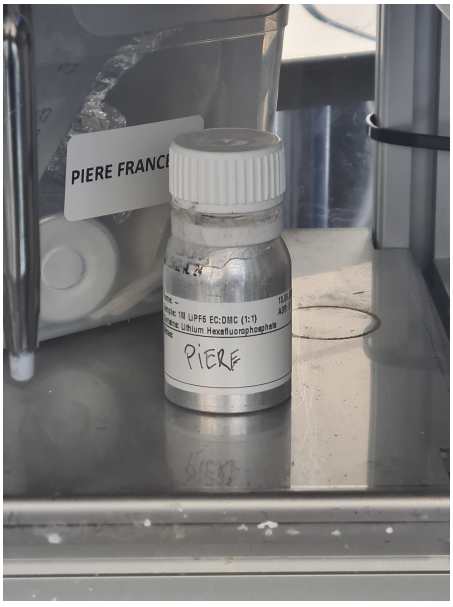

(a) Electrolyte ECDMC 1:1

(b) Glovebox of the battery lab

Figure 4.4: The use of glovebox is mandatory to prevent side reactions during the assembly of the coin cell.

Components	Material	Diameter(mm)	Thickness
Top cap	Steel	1.6 ± 0.001 (cm)	1 (mm)
Anode CC(current collector)	Aluminium	1.277 ± 0.001 cm	180 (μm)
Anode electrode	Lithium foil	1.277 ± 0.001 cm	110 (μm)
Separator	Plastic	1.5± 0.001 cm	20 (μm)
Electrolyte	ECDMC	-	-
Cathode electrode	LFP	1.277 ± 0.001 cm	80 (μm)
Cathode CC(current collector)	Aluminium	1.277 ± 0.001 cm	20 (μm)
Spacer	Steel	1.5 ± 0.001 (cm)	1 (mm)
Bottom cap	Steel	1.6 ± 0.001 (cm)	1 (mm)

Table 4.1: Design Properties of the components in a coin cell

4.2. Procedure for the conduction of electrochemical cycling experiments

For the electrochemical testing, two different softwares were used. The majority of the experiments conducted in the **Lanhe battery testing system**, and some of the high temperature experiments in the **Maccor battery testing system**.

4.2.1. Lanhe and Maccor Battery Testing System

This software represents a cutting-edge battery analysis tool for both academic and commercial purposes. Its remarkable precision, with a sampling rate of one ten-thousandth, and high-speed capabilities make it a standard in the field. The software offers versatility by allowing for a wide range of voltages and currents, making it suitable for various experiments and diverse capacity cells.

For constant current (CC) processes, electrical current is supplied from a power source until the predetermined maximum voltage is attained. Complex electrical circuits, including metal-oxide-semiconductor field-effect transistors (MOS-FETs), control the current during this phase. Similarly, for constant voltage (CV) processes, a comparable mechanism is employed. While Maccor is a similar software, it lacks the computational power of Lanhe, but for the purposes of this study, both software tools are more than adequate.

The experimental procedure initiates with the cell being allowed to rest for at least half a day, ensuring complete absorption of the electrolyte and reaching the desired temperature. Next, a charge cycle using constant current (CC) is performed, considering that lithium is present in the cathode material. After reaching the cut-off voltage, the cell undergoes another rest period before starting the discharge phase. The discharge phase involves two steps: a constant discharge current rate (D-CC) until the voltage reaches 2.5V, followed by a constant discharge voltage (D-CV) until the current drops below 0.03 C, ensuring full discharge of the battery. This procedure is repeated once more, with the initial two cycles referred to as formation cycles. The charge and discharge C-rate are set at 0.1 C, allowing the battery to approach equilibrium without causing damage.

Following the formation cycles, a specific pattern is repeated twice, employing four different current rates. Starting from 0.5 C, with increments of 0.5 C, the procedure begins with a 10-minute rest period. Subsequently, a constant current (CC) rate is applied until the cut-off voltage surpasses 4.0 V. The cell then rests for another 10 minutes, after which a CC rate of 0.1 C, with the same cut-off voltage, is used. A constant current-constant voltage (C-CV) at 4V is applied until the current reduces below 0.003 C. This completes the charge phase, followed by a 10-minute rest period before the discharge phase commences. The discharge phase mirrors the charge phase with a constant

discharge current rate (D-CC) of 2.5 V as the initial step..

Steps

Order	Work Mode	End/Jump Condition 1	and)End/Jump Condition 2	Range	Sampling Condition
1	REST	Time ≥ 12:10:00		Auto	60s
2	C_CRATE 0.1 C	Voltage ≥ 4 V		Auto	600s,5mV
3	REST	Time ≥ 10:00		Auto	60s
4	D_CRATE 0.1 C	Voltage ≤ 2.5 V		Auto	600s,5mV
5	REST	Time ≥ 10:00		Auto	600s,10mV
6	C_CRATE 0.1 C	Voltage ≥ 4 V		Auto	600s,5mV
7	REST	Time ≥ 10:00		Auto	60s
8	D_CRATE 0.1 C	Voltage ≤ 2.5 V		Auto	600s,5mV
9	D_CV 2.5 V	Current ≤ 0.03 mA		Auto	30s,20mV
10	REST	Time ≥ 10:00		Auto	600s,10mV
11	C_CRATE 0.5 C	Voltage ≥ 4 V		Auto	9s,5mV
12	REST	Time ≥ 30:00		Auto	60s
13	C_CRATE 0.1 C	Voltage ≥ 4 V		Auto	600ms,5mV
14	C_CV 4 V	Current ≤ 0.03 mA		Auto	60s
15	REST	Time ≥ 10:00		Auto	60s
16	D_CRATE 0.5 C	Voltage ≤ 2.5 V		Auto	9s,5mV
17	REST	Time ≥ 30:00		Auto	60s
18	D_CRATE 0.1 C	Voltage ≤ 2.5 V		Auto	600s,5mV
19	D_CV 2.5 V	Current ≤ 0.03 mA		Auto	60s
20	REST	Time ≥ 30:00		Auto	60s
21	[LOOP] 11 Step	LoopCount ≥ 2			

Figure 4.5: The procedure of the electrochemical testing.

The operating temperature is fixed by a cooling box or a temperature chamber. The experimental temperatures are $-5°C$, $0°C$, $10°C$ (fixed by cooling box) $25°C$ (Room temperature) and $50°C$ (fixed by temperature chamber). Furthermore, different high temperatures were tested but these results are not presented in this section but in the Appendix because of the use of a different cell. The two experimental tests have the material properties of table 4.1 with the only difference that one cell has capacity equal to 2mAh/cm^2 and the second one 1mAh/cm^2.

4.3. Measurements and calculations of design parameters

4.3.1. Isothermal Assumption

The area capacity by the manufacturer is 2mAh/cm^2.The area of coin cell is 1.28cm^2, thus the capacity at 1C is 2.56mAh.
By checking the OCV value which is 3.422V at 25 °C, and the discharge voltage curve for 1C at ambient temperature, the overpotential is approximately between 0.1 to 0.2V. Multiplying the overpotential with the capacity, the energy that has spent in irreversible processes can be calculated. The energy is equal to: $0.2V \cdot 0.00256Ah = 0.000512Wh$. Multiplying by 3600, the energy in Joule is: **E = 1.8452J.**
To simplify matters, assuming that the cell is exclusively made of stainless steel, the values for its mass (m) and heat capacity (c_p) can be found. The mass is measured close to 5.1g and the heat capacity of stainless steel is 520 $J/(kg \cdot K)$.
Assuming steady state, the temperature difference can be given by the following relation: $Q = m \cdot c_p \cdot \Delta T$. The maximum temperature difference using the total energy as heat is 0.68K.

To sum up, after many strong assumptions the maximum temperature difference that you can have in a coin cell which consists of stainless steel in close to 0.7K. The coin cell has different material layers, because of the anode(Lithium metal) separator and cathode which are materials such as plactic and LFP which have a higher heat capacity value. This implies that the temperature difference in our study will be a lot smaller. Hence, the isothermal assumption is valid.

4.3.2. Porosity calculation

The porosity was also reported by the manufacturer but the calculation is the following:

1^{st}Step: Area of cathode is calculated. The circular area in the coin cell of LFP is 1.28 cm^2.

2^{nd}Step: The total density of the cathode is calculated using the percentage of each material. The effective density is equal to 1.55 g/cm^2.

3^{rd}Step: Measure the weight of the cathode material. The current collector (aluminium) is attached to the cathode material and should be subtracted from the total weight. The effective weight of cathode is 18.5 mg. Using the weight and the density from step 2, the volume is calculated (0.0337 cm^3).

4^{th}Step: The effective volume of the cathode material is calculated by multiplying the area by the thickness of the electrode. The effective volume is 0.0896 cm^3.

5^{th}Step: The definition of porosity is given below.

$$\epsilon = \frac{V_{tot}}{V_{solid}} V_{tot} \approx 0.56 \tag{4.1}$$

4.3.3. Active material calculation

The manufacturer gives the active particle fraction per weight as 90 %, and 5% is carbon and 5% Polyvinylidene fluoride (PVDF). The input parameter should in volume loading so the following assumption about the density of the mentioned materials are presented.
Density of carbon: ρ_c= 2.2 g/cm^3
Density of PVDF: ρ_p= 1.8 g/cm^3
Density of LFP: ρ_l= 1.5 g/cm^3

Finding all the different volumes using the formula of density definition and take the percentage of each material, the final volume loading is 93%.

4.4. Experimental Results

The results are divided into two main parts. The first part focuses on the operating temperature and comprises five different figures, which demonstrate the effect of temperature on the battery's power output. This analysis provides valuable insights into how temperature influences the battery's performance.

In the second part, an analysis based on the C-rate is presented, offering essential insights into understanding the impact of temperature concerning the current demand.

The figures corresponds to the high capacity cell of 2mAh/cm^2 because only this cell is tested also in the computational section. The figures of the low capacity cell are presented in the Appendix.

4.4.1. Temperature variation

The figure displayed below illustrates the discharge voltage curves at room temperature. Throughout the experiment, temperature measurements were recorded using a thermocouple, with fluctuations of approximately 0.5 °C due to sensitivity errors. The isothermal assumption is commonly employed in such experiments, given the minimal power output generated by the coin cell. Additionally, evidence supporting the isothermal condition is provided, further confirming the validity of this assumption.

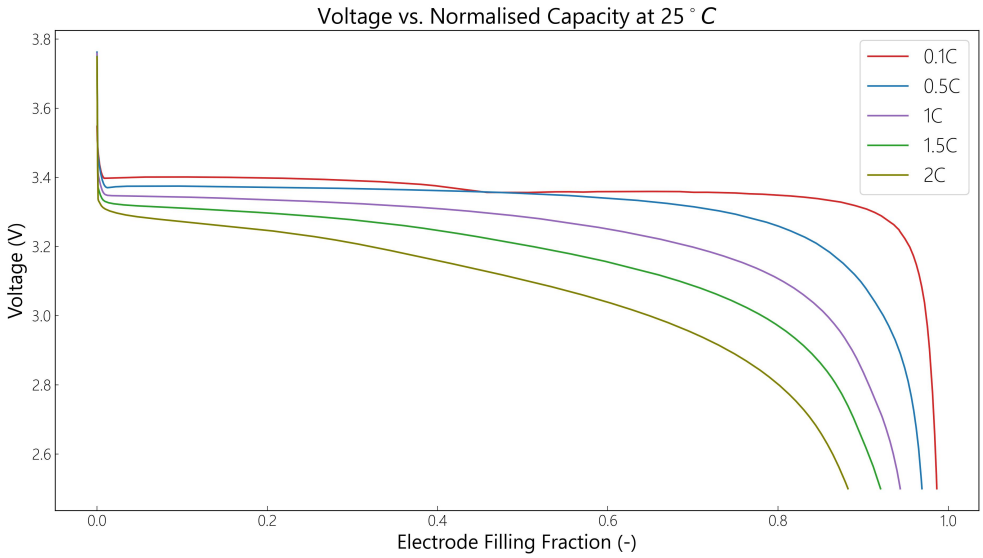

Figure 4.6: Experimental Discharge Voltage curve in five different C-rates at 25°C .

The first experiment was conducted at 25° C. In all battery testing experiments, as mentioned before the first two cycles are formation cycles. Thus, the dip in the 0.1C can be because of the formation of the cell. The capacity in such a small current reaches the maximum which shows that the overpotentials because of reaction and transport limitations are negligible. The increase of C-rate infers a decrease in the starting point of the voltage because of the separator overpotential.In the battery operation, the separator overpotential remains constant throughout the cycle, as it is not affected by the cycling time. On the other hand, the diffusion transport overpotential experiences an increase with longer cycling times. This phenomenon occurs due to the accumulation of reaction products or depletion of reactants at the electrode-electrolyte interface during extended cycling. As the cycling time increases, the rate of diffusion becomes a limiting factor, leading to a higher overpotential associated with the transport of reactants and products within the battery. The variation in diffusion transport overpotential is a critical aspect to consider when analyzing battery performance over extended cycling periods.Furthermore, at lower C-rates, due to the reaction approaching equilibrium, the system tends to stabilize around certain points. Stability points are the lowest value points in the green curve shown in Figure 2.6. Additionally, during this phase, a

relatively flat plateau becomes apparent in the data. Increasing the C-rate, transport limitations because of conductivity losses are dominant and some particles can not be lithiated reaching lower maximum capacity.

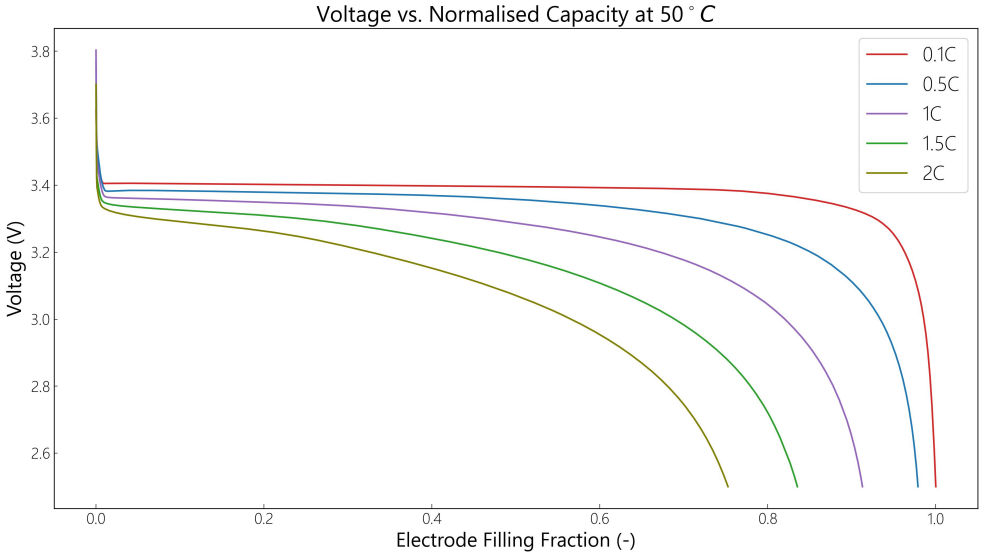

Figure 4.7: Experimental Discharge Voltage curve in five different C-rates at 50°C .

This graph is in elevated temperature. The optimal temperature range of LFP batteries is below 50° C and this was the reason for the choice of this value. The high temperature promotes the reaction rate through the Arrhenius relation. The electrolyte conductivity is known to increase with an increase in temperature, as described by the model of Stefan-Maxwell and Valoen-Bernardi coefficients. As the temperature rises, the mobility of ions within the electrolyte increases, leading to higher ion transport rates and a subsequent increase in conductivity, thus, the lithium ions intercalate faster in the particles. The starting point of the voltage curve is higher than the previous case which means that the separator overpotential decreases. Although the increase on C-rate presents a steeper gradient in the voltage curves which ends in smaller capacities as we will see in the next subsection. Thus, the higher temperature accelerates the reactions but also decrease the full capacity of the cell.

The figure below initiates the analysis of the impact of low operating temperature on battery performance. Notably, the voltage loss at low temperature is substantial compared to previous cases. Additionally, as the C-rates increase, the derivative of voltage with respect to the filling fraction becomes constant. This behavior indicates that the low temperature poses challenges for ion movement and their reaction with solid particles. The activation barrier is difficult to be overcome, leading to decreased utilization of the full length of the electrode. The hindrance in ion movement and reaction at low temperature limits the overall battery performance, resulting in reduced efficiency and capacity.

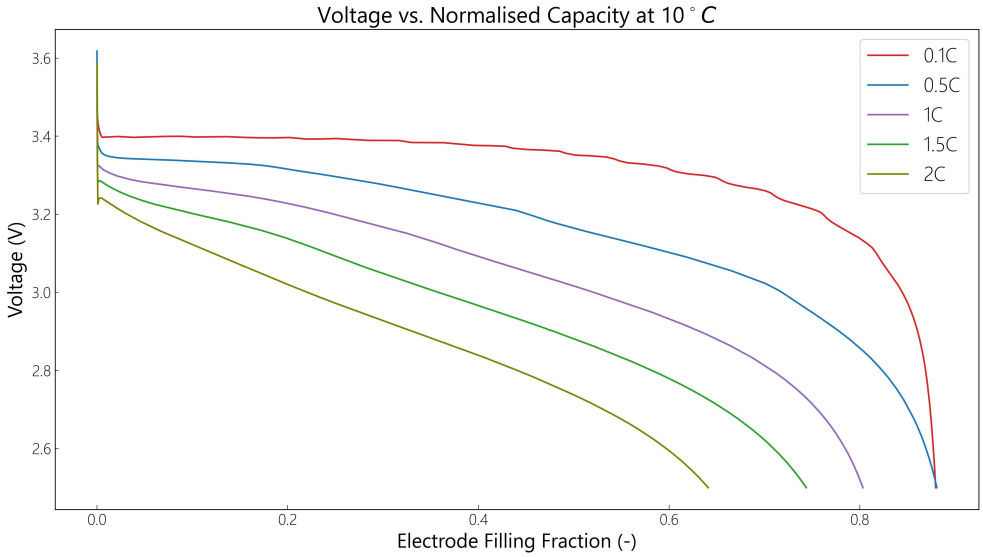

Figure 4.8: Experimental Discharge Voltage curve in five different C-rates at 10°C .

Resting the battery for 12 hours at 0°C results in the partial freezing of the electrolyte or electrode components. Consequently, some particles become completely inactive during the subsequent electrochemical testing of the battery. This leads to more than 20% of the total capacity being rendered useless during testing at 0.1C due to the adverse effects of low temperature. Furthermore, when the C-rate is increased, the voltage curve experiences a significant drop, indicating very high overpotentials at low temperatures. This suggests that the battery's performance is notably affected by the rate of current discharge, particularly in colder conditions, resulting in substantial losses in efficiency.

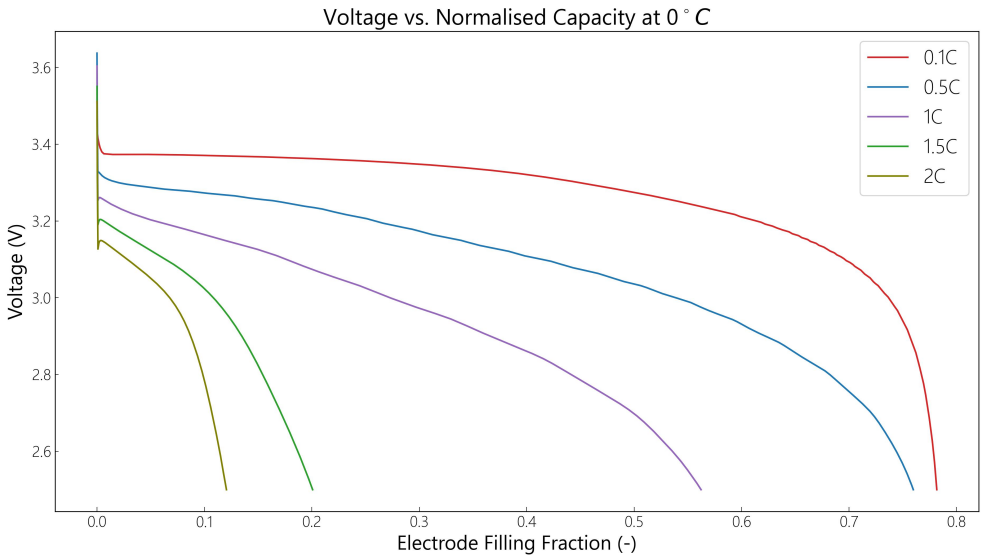

Figure 4.9: Experimental Discharge Voltage curve in five different C-rates at 0°C .

Between -5°C and 0°C, the results show a remarkable similarity, with the curvature of the discharge curve nearly diminished. This leads to a linear relationship between voltage and filling fraction within this temperature range. However, it is important to note that the dependence on the C-rate is entirely nonlinear, suggesting that the battery's response to changes in the rate of current discharge is not linearly proportional. The nonlinearity with respect to the C-rate signifies that the battery's performance is highly sensitive to the rate at which it is charged or discharged in very low temperatures (so in countries which the temperature during winter is close to 0 °C) , which requires careful consideration.

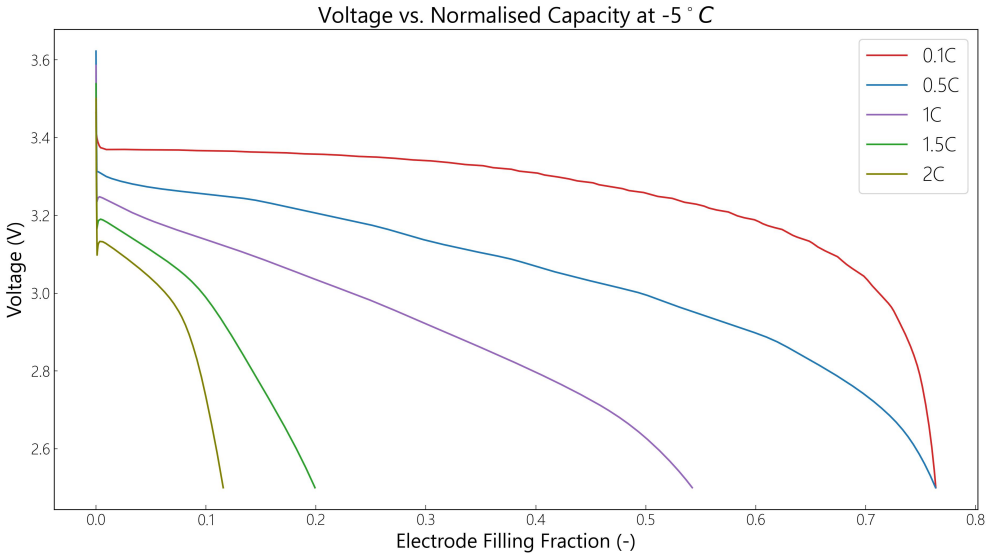

Figure 4.10: Experimental Discharge Voltage curve in five different C-rates at -5°C .

4.4.2. Current Variation

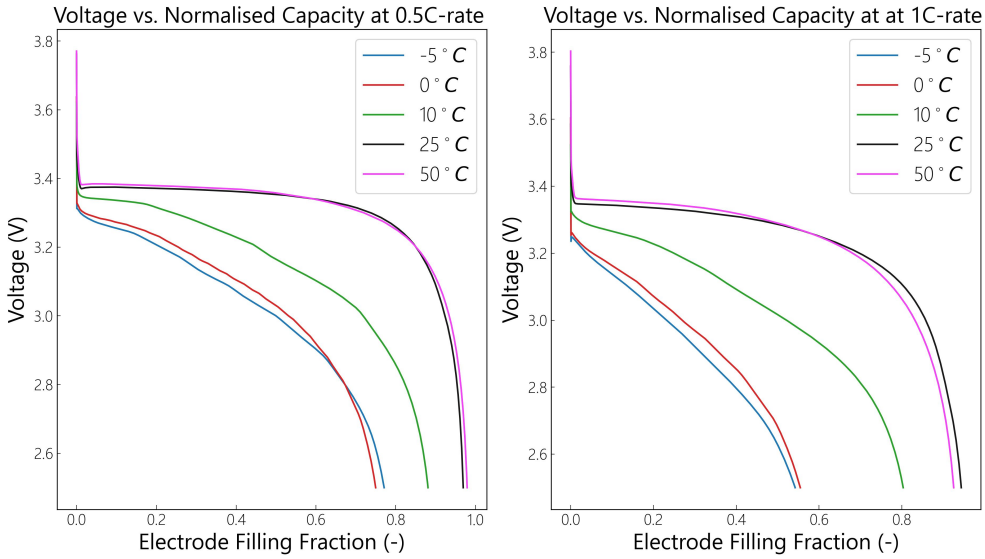

Figure 4.11: Experimental voltage curves in different temperatures in 0.5C (Left) and in 1C(Right).

In the figure 4.11 different discharge voltage curves are presented in five different temperatures in 0.5C and 1C. The capacity loss increases as the C-rate increases and when the temperature plummets below 10 °C this behavior becomes nonlinear. The difference between the two figures is a loss of 10% to 20% of capacity by increasing the C-rate from 0.5C to 1C. Indeed, an intriguing observation is that the discharge curve at 50°C exhibits a slightly lower capacity than the curve at ambient temperature. This unexpected behavior will be subject to a detailed investigation and analysis in the forthcoming figure. A comprehensive examination will be conducted to elucidate the underlying factors responsible for this unique characteristic, shedding light on the intricate relationship between temperature and battery performance at 50 °C.

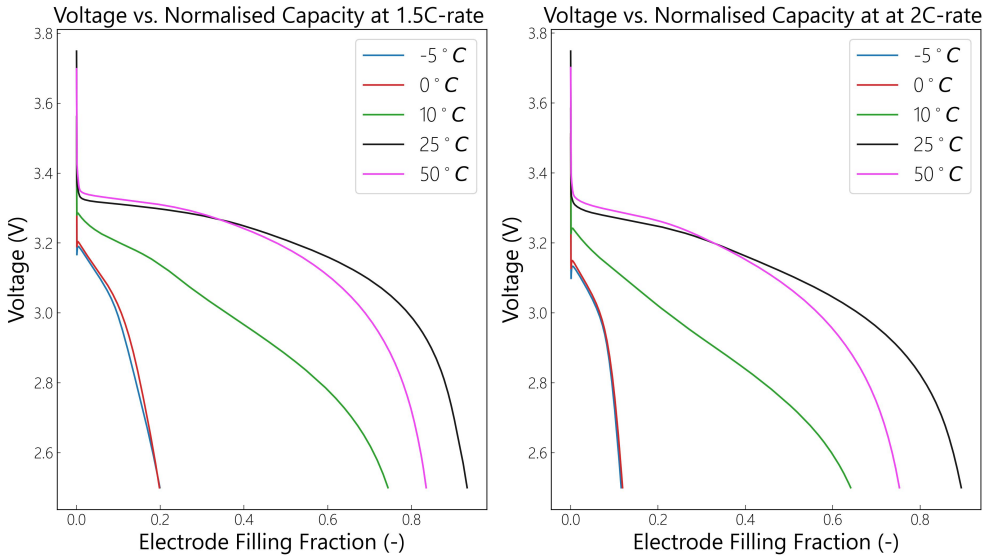

Figure 4.12: Experimental voltage curves in different temperatures in 1.5C (Left) and in 2C(Right).

As the C-rate increases to 1.5 and 2 at 50 ° C, the behavior of the cell progressively becomes less efficient. This trend is evident from the discharge voltage curves, which show a notable decrease in the cell's overall capacity at higher C-rates. The higher current demand at these elevated temperatures results in increased overpotentials and a more pronounced voltage drop during discharge. Consequently, the battery's capacity is compromised, leading to reduced energy output and efficiency. This finding was counterintuitive, because the higher temperature, the faster the reaction rate and the movement of the ions. The optimum temperature range is between 20 ° C and 50 ° C thus this experimental temperature was the threshold.
The first mechanism that could explain this outcome was the state of charge of the battery. After every cycle a Constant Current and Constant voltage steps are implemented to completely charge the battery before the next cycle. In this temperature after the CC step the capacity was a lot lower than the previous cycles. Although after the CV step, the discharge capacity reaches very close to the initial capacity that can be measured in the 0.1C cycle. In the literature, there is a profound dependence of open circuit voltage to the state of charge and this also is connected to the operating temperature ([32],[10], [44]) .
The second mechanism was the degradation. The lower capacity as you increase the c-rate in this elevated temperature indicates a possible irreversible damage in the cell. The developed solid electrolyte interphase (SEI) demonstrates a lack of thermal stability, rendering it susceptible to degradation. Exposure to elevated temperatures during cycling can lead to its deterioration and potential destruction. The formation of a new SEI demands the consumption of lithium ions which infers the decrease of active material and hence, the capacity loss[2]. Furthermore, battery degradation can be due to reaction kinetics degradation and impedance increase. This can be observed by an earlier end of the charging or the discharging process, similar to our case [39]. In the same research the big influence of temperature to capacity fade is also presented. Cycles with operating temperature above 50 °C can have 10 times bigger capacity impact than in the ambient temperature (Figure 4.13).

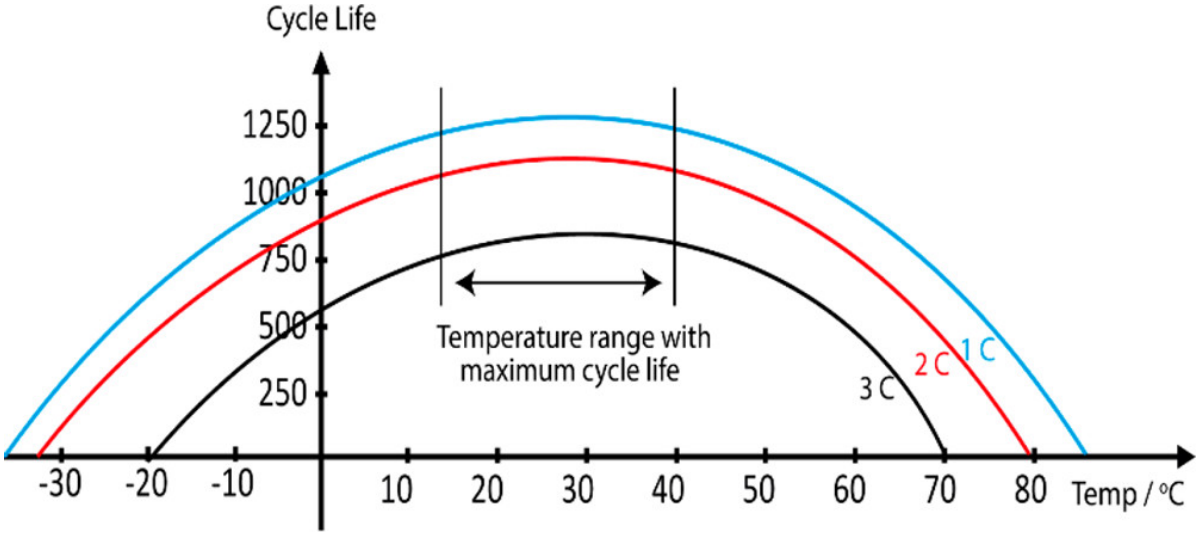

Figure 4.13: Effect of operating temperature on LIB cycle life [39].

5

Results

5.1. Monte Carlo Analysis and Optimization Insights

Initially, the research centered on estimating four crucial parameters: the serial electrical conductivity, the Bruggerman exponent, the particles' electrical conductivity, and the reaction constant k_0. Among these parameters, the Bruggerman exponent and electrical conductivity were chosen as constant values, as detailed in the Methodology section. This decision was based not only on existing literature but also due to the high sensitivity of the results to these values. While some parameter combinations exhibited better fits with the experimental discharge voltage curves, the same parameters yielded entirely random results at different C-rates and temperatures. This unpredictability underscored the complexity of the battery behavior and the significance of accurately defining these constants for reliable predictions.

The parameter estimation takes into account five different temperatures (-5°C, 0°C, 10°C, 25°C, 50°C) and two different C-rates(0.5C, 1C). Below the objective function (Mean root squared error between simulated and experimental discharge voltage curve) of the modified Monte-Carlo approach is presented in 3 different operating conditions.

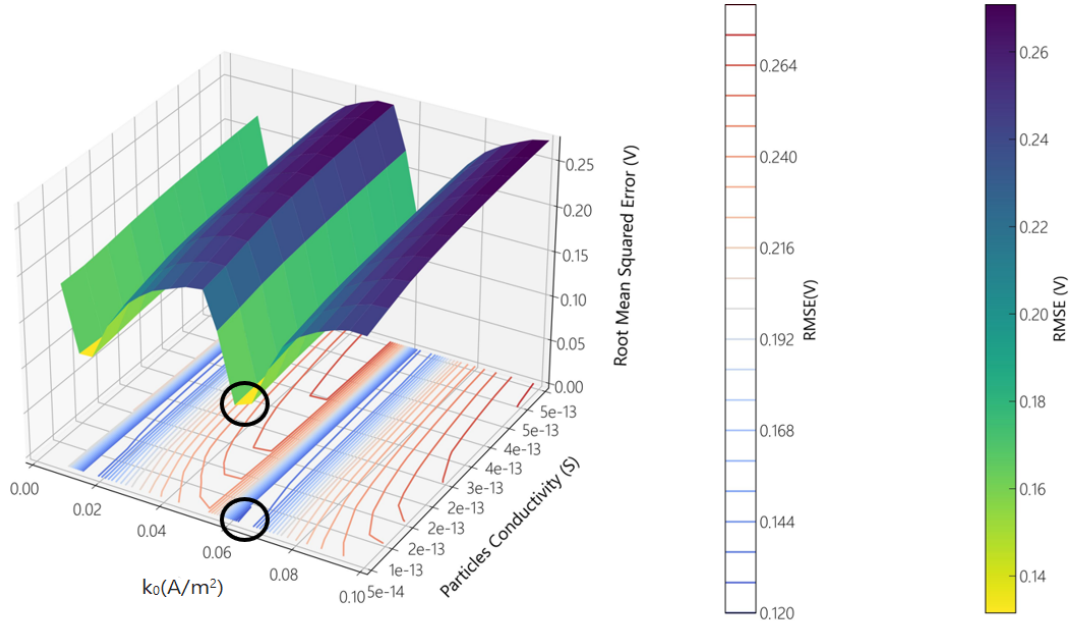

Figure 5.1: Optimization for 0.5C and 0°C.

The figure 5.1 illustrates the value of the root mean squared error at 0.5C and 0°C. As it is mentioned before, many simulations were conducted and the 3 best simulations were chosen in order to repeat the procedure of the root finding in the vicinity of them. The figure 5.1 is one of the last bunch of simulations and the range of the varying parameters were: k_0 between 0.01 to 0.1 and Particles Conductivity between $0.5e^{-13}$S to $5e^{-13}$S. It is clear that different local minima can be noticed from the 3D plot depending on the k_0 value. The projection of the 3D curve in the k_0-Particles' conductivity plane is also depicted (coolwarm contours). The influence of particles conductivity is not so visible but the smaller the value the closer to the minimization of the error is(black circles in the figure).

It is important to note that the k_0 is not the effective in these 3D plots but the prefactor k in the equation 5.1. This is the reason for the formulation of this relationship in the next subsection. In MPET the activation energy and the temperature with respect to the ambient temperature in Kelvin is normalised as depicted below.

$$k_{0,eff} = k \cdot e^{\frac{Ea}{Na \cdot k_b \cdot T_{ref}} \cdot (-\frac{1}{\frac{T_{op}}{T_{ref}}} + 1)} \tag{5.1}$$

A similar graph can be presented at 0.5C - 10°C, where the range of k_0 remains unchanged, but the G_c (particles' conductivity) varies between $0.5e^{-13}$ S to $3e^{-13}$ S. Notably, the introduction of series conductivity between paticles is the key factor that enables the battery to achieve the same maximum capacity as observed in the experiments. Consequently, the effective range of this value aligns with the depicted ranges for each specific case. The ability to capture the same maximum capacity through the implementation of parallel conductivity underscores its crucial role in accurately simulating the battery's performance across different conditions and parameters.

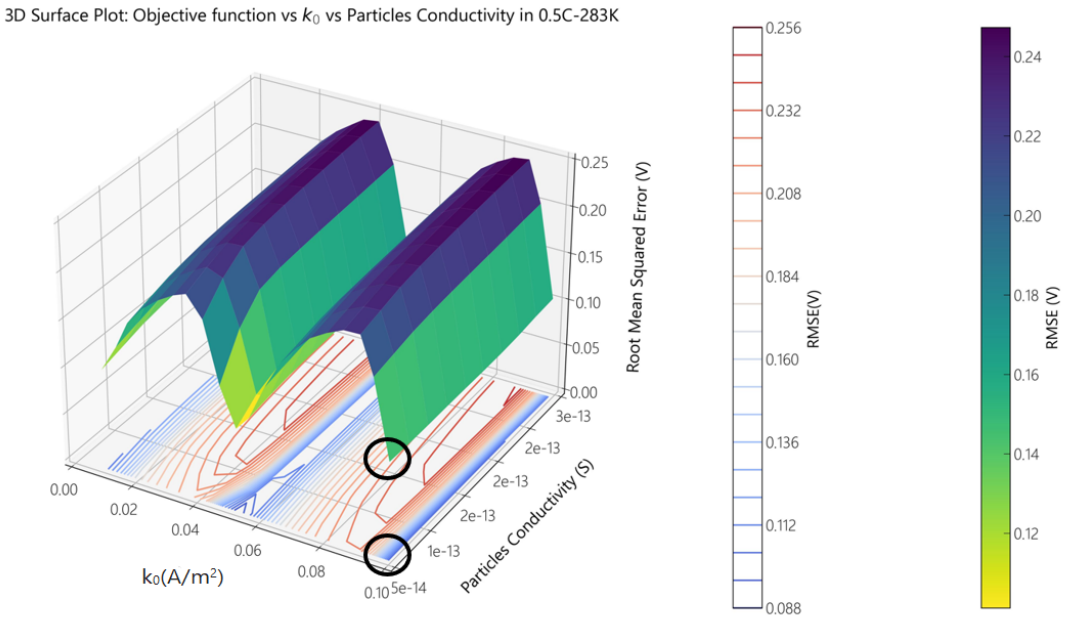

Figure 5.2: Optimization for 0.5C and 10°C.

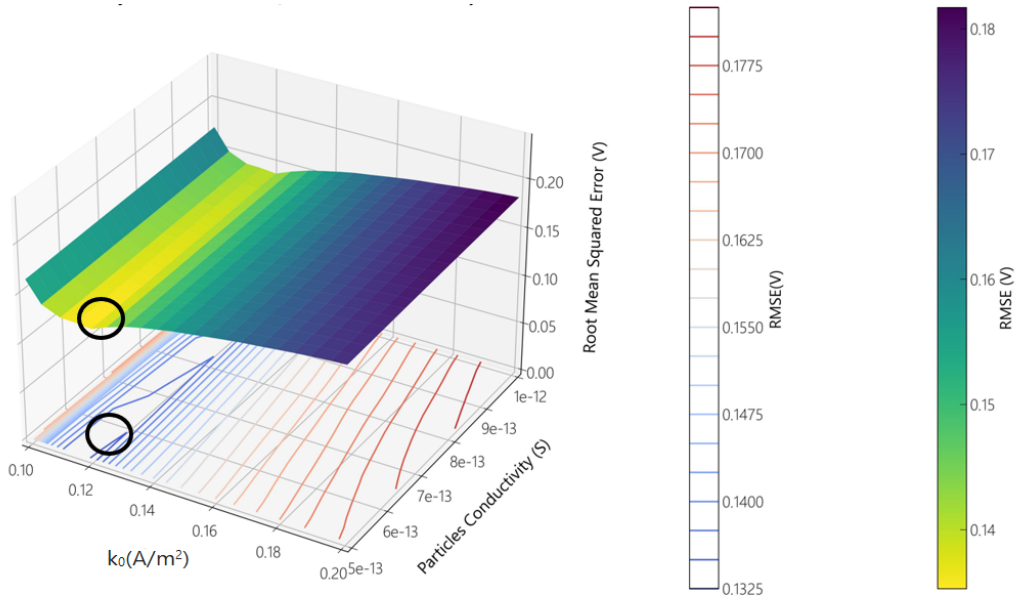

Figure 5.3: Optimization for 1C and 25°C.

This 3D plot represents the objective function's values at 1C - 25°C, demonstrating a different range compared to the previous cases. Here, the parameter k0 varies between 0.1 and 0.2, while G_c falls within the range of $5e^{-13}$ S to $10e^{-13}$ S. A crucial finding from these simulations is the identification of a threshold value for the particles' conductivity, which was observed to be around $8e^{-13}$ S. Notably, particle conductivities greater than this threshold had no discernible influence on the maximum capacity.

It is essential to note that the 3D plots presented here pertain solely to the 1C-rate scenario,

yet the optimization process encompasses the best parameters for two C-rates. Therefore, the final results for validation may exhibit slight variations due to the inclusion of additional C-rate data.

5.2. Validation of simulations and experiments

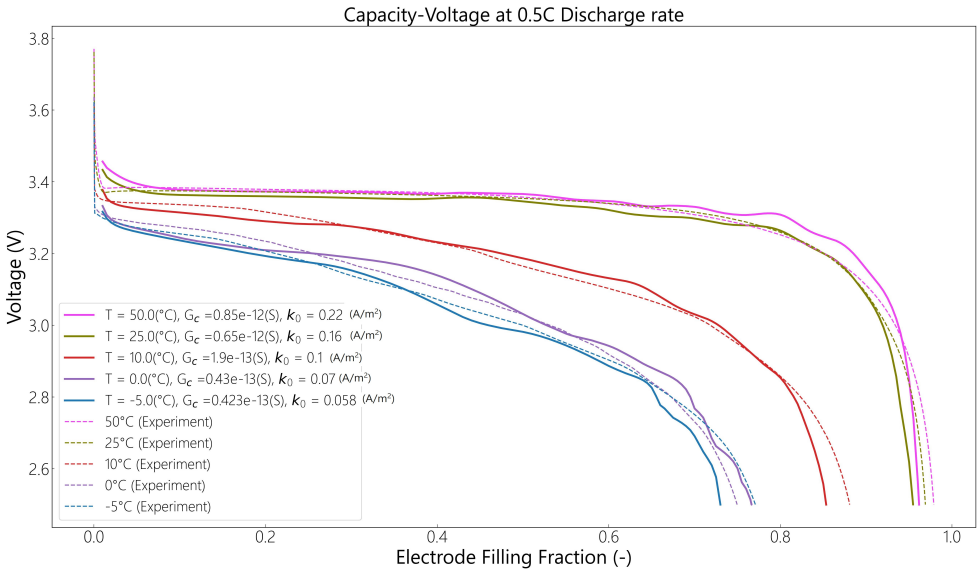

Figure 5.4: Validation of simulation results with the experimental results for all the temperatures in 0.5C.

C-rate	Temperature(°C)	RMSE(V)
0.5	-5	0.08(2.7%)
0.5	0	0.05(1.8%)
0.5	10	0.06(1.9%)
0.5	25	0.07(2.2%)
0.5	50	0.07(2.2%)
1	-5	0.13(4.3%)
1	0	0.09(3.1%)
1	10	0.06(2.0%)
1	25	0.08(2.5%)
1	50	0.16(4.7%)

Table 5.1: Summary of Root mean squared error values between experimental and simulated discharge curves

The parameter estimation depends on 5 different temperatures and 2 different c-rates. In the table you can see the final RMSE value of every curve. The simulation in 0.5C is very close to the experiments because of the smaller overpotentials. More specifically, the value of k_0 influence the starting point of all discharge curves. The maximum capacity can be simulated as close as possible but with a small deviation from the real value. A better optimization of the G_c will result to the best fit. The trend of the simulated curves are similar to the experiments which is the most important outcome. The wavy behavior can be explained by the numerical limitations because of the simulation of discrete particles. The discretization that this software is using has a sensitivity in very steep concentration gradients, which can cause minor oscillations. Increasing the number of particles, this wavy behavior can be nullified.

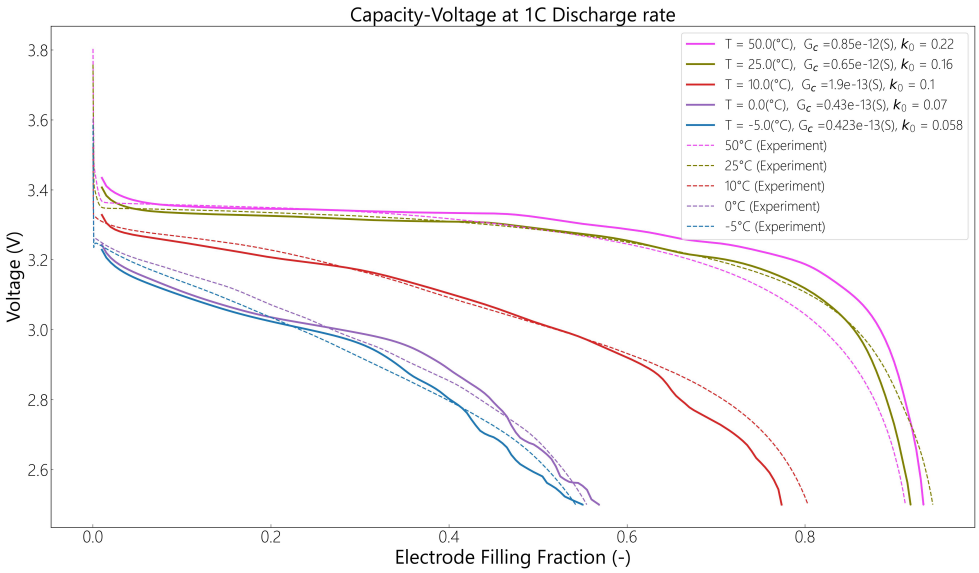

Figure 5.5: Validation of simulation results with the experimental results for all the temperatures in 1C.

As the current increases, the curves become unstable in the end of the simulation in low temperatures This can be explained because of, not only the bigger overpotential but also the discrete number of simulated particles. The biggest deviation is observed in 50°C as it was expected because this experiment was the last one and the cell starts to degrade. A further investigation of more experiments should be conducted but as it is clear from the next figure, according to simulations the maximum capacity does not decrease with the increased temperature.

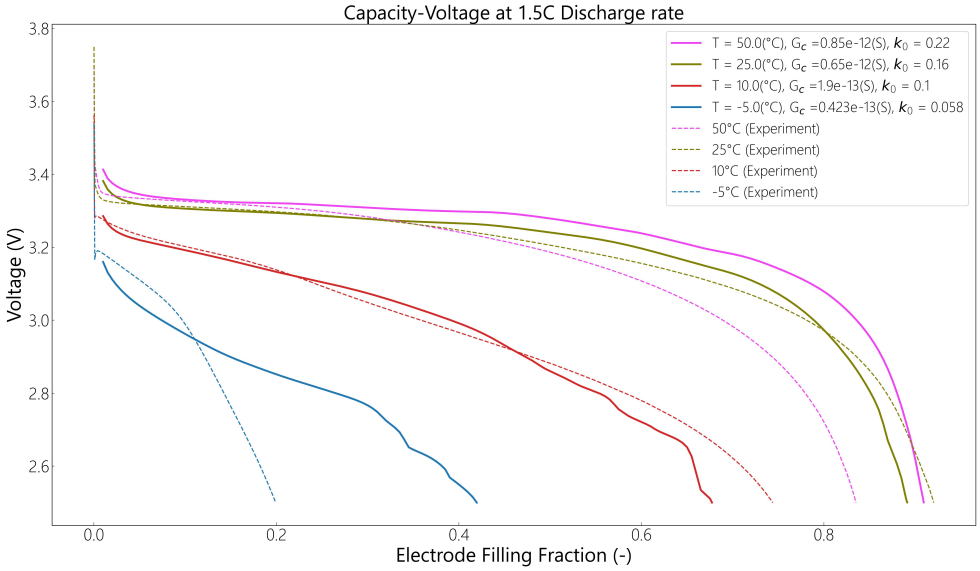

Figure 5.6: Validation of simulation results with the experimental results for all the temperatures in 1.5C.

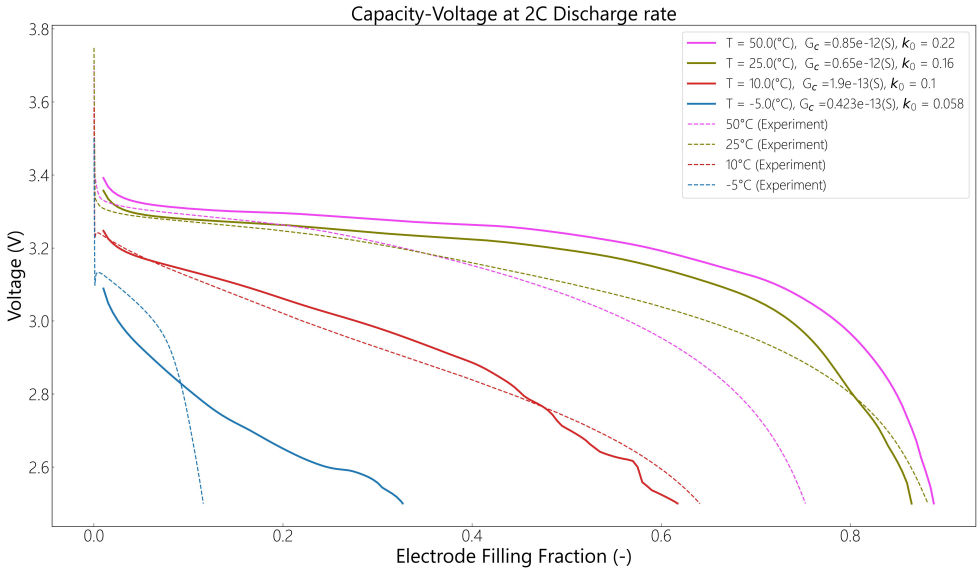

Figure 5.7: Validation of simulation results with the experimental results for all the temperatures in 2C.

The previous figures do not include the 0°C discharge curves(the solver did not converge because of the LU factorization failure) but the main outcome is that the software loses its accuracy in very low temperatures(the error is 8%). Furthermore, when comparing the simulation and experimental results at 50°C, the likelihood of cell degradation becomes more evident. Moreover, the cell doesn't recover the same capacity at ambient temperature after the high-temperature experiment,

implying irreversible damage.

Below, the two interpolated functions that stand as the primary outcome of this study are showcased. The rate constant has an exponential correlation with temperature, as governed by the Arrhenius relation. The equation formulated here enables the fitting of the activation energy. The MIT group discovered that a comparable relationship is corroborated by utilizing chronoamperometry experiments, a completely different approach. This study concludes with a value of activation energy which is remarkably close to our findings[4].

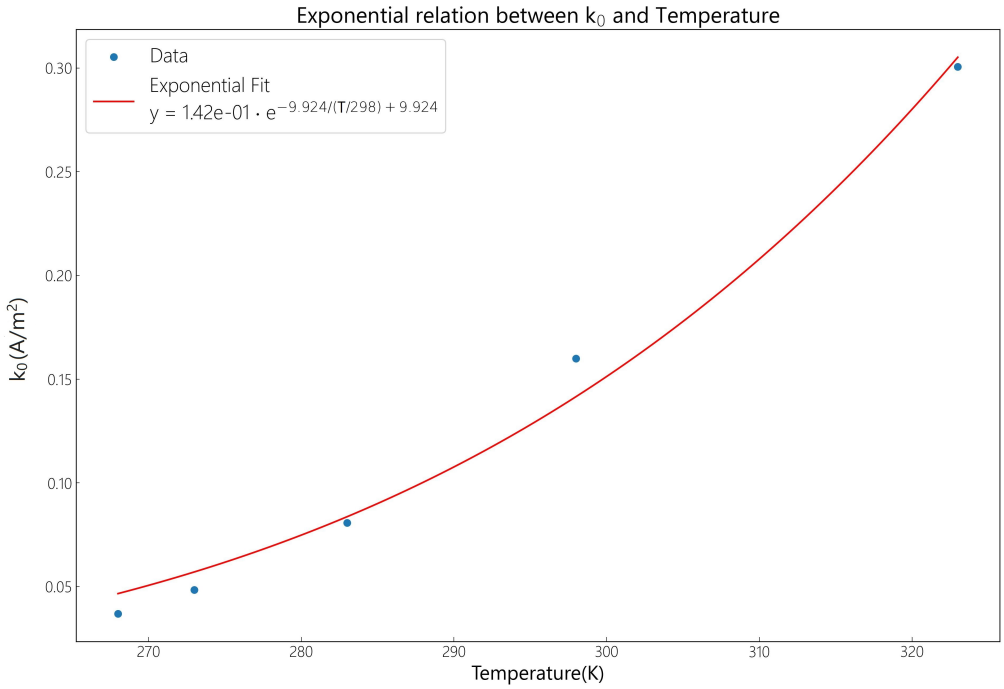

Figure 5.8: Relation between k_0 with temperature.

One of the main limitations of LFP material is its poor electrical conductivity. The particles conductivity is a very complex phenomenon to describe numerically and in the following two researches an exponential relation between temperature and G_c is suggested [11],[29]. The behavior of electrical conductivity with respect to temperature can be similar to a semiconductor's behavior. The poor electrical conductivity of LFP but the high amount of loading by carbon can enable this behavior and the exponential relation between the temperature and the particles' conductivity can be justified.

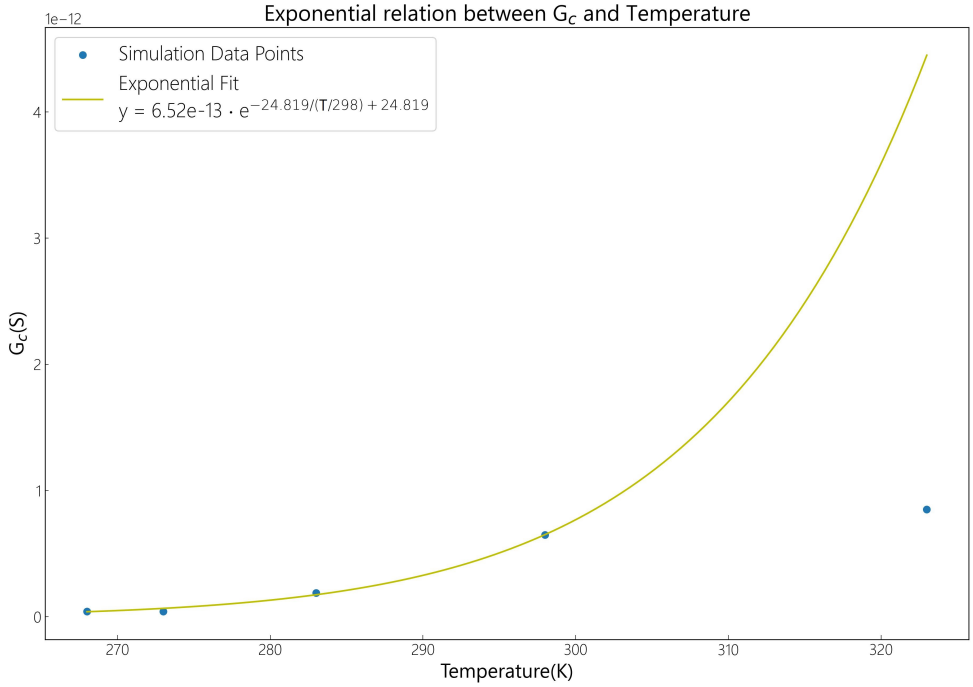

Figure 5.9: Relation between g_c with temperature.

Following the application of the aforementioned equations, the visualized graphs display the comparison between simulations and experimental results. The only discernible distinction emerges in the 0°C discharge curve. These graphs aptly demonstrate the remarkable adaptability of the software in forecasting coin cell voltage curves across diverse C-rates and temperatures, all while maintaining the integrity of other parameters constant. This outcome underscores the software's potency in modeling intricate battery behavior with dynamic precision.

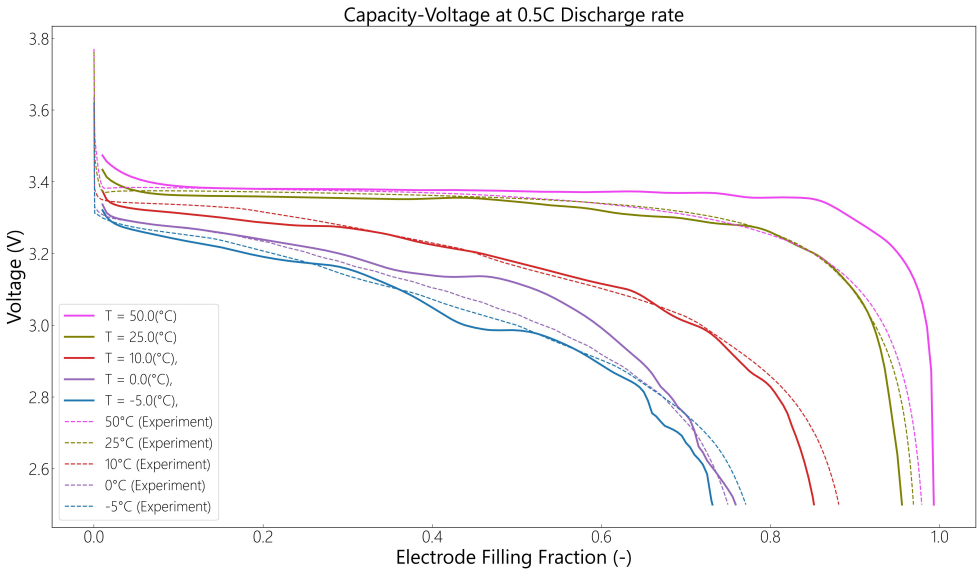

Figure 5.10: Validation of simulation results with the experimental results for all the temperatures in 0.5C.

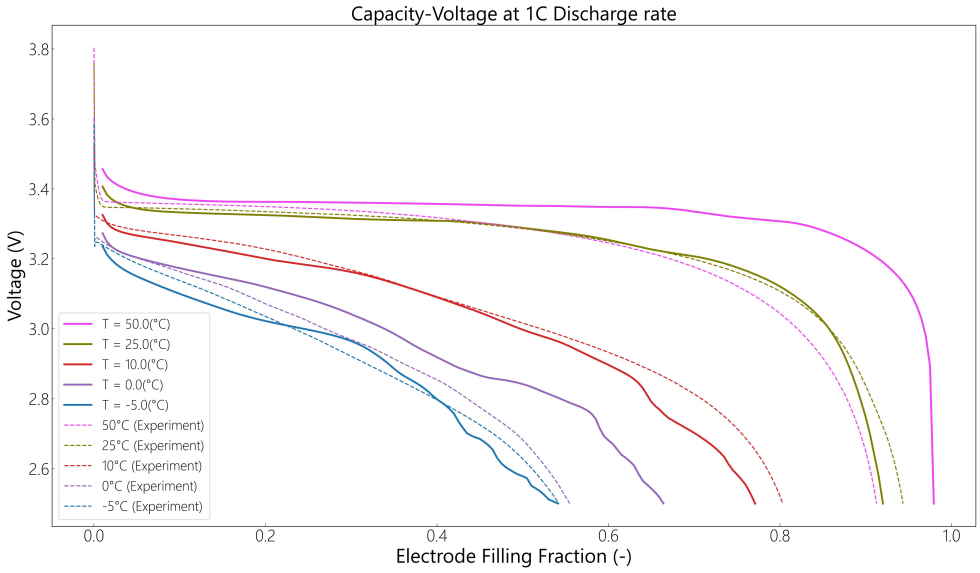

Figure 5.11: Validation of simulation results with the experimental results for all the temperatures in 1C.

5.3. Active particle population with temperature

One of the main capabilities of MPET is the implementation of phase field modelling which is one of the main characteristic of the LFP material. The phase field enables the possibility of varying the active particle population based on the surface area of the particle. This is the significant point to

grasp from the following figures. The active particle population gives insight of how the particle size influences the connectivity between the particles, if the system is transport of reaction limited or even where a possible hotspot can be generated.
The subsequent illustrations depict the dynamic distribution of active particles throughout the battery discharge process. The connection between the intercalation of lithium ions within the particles is governed by a correlation between the rate constant and the temperature. In simulations conducted at extremely low temperatures, the range of active particles during discharge lies within the 20% to 30% range, with certain particles becoming completely inactive over the course of the process (see Figure 5.14). This particular figure represents a similar simulation conducted at 0°C, featuring a smaller number of particles.
The ease of lithiation for particles with smaller surface areas, influenced by the Allen-Cahn model, is noteworthy. Additionally, the particles' conductivity significantly influences their lithiation process. Notably, particles connected to larger particles do not experience lithiation with the same consistency compared to those interconnected with smaller particles. As the temperature is elevated, the population of active particles grows. Nonetheless, upon comparing simulations conducted at room temperature with those at higher temperatures, a notable disparity of over 10% in active particle population is observed in the room temperature simulation.

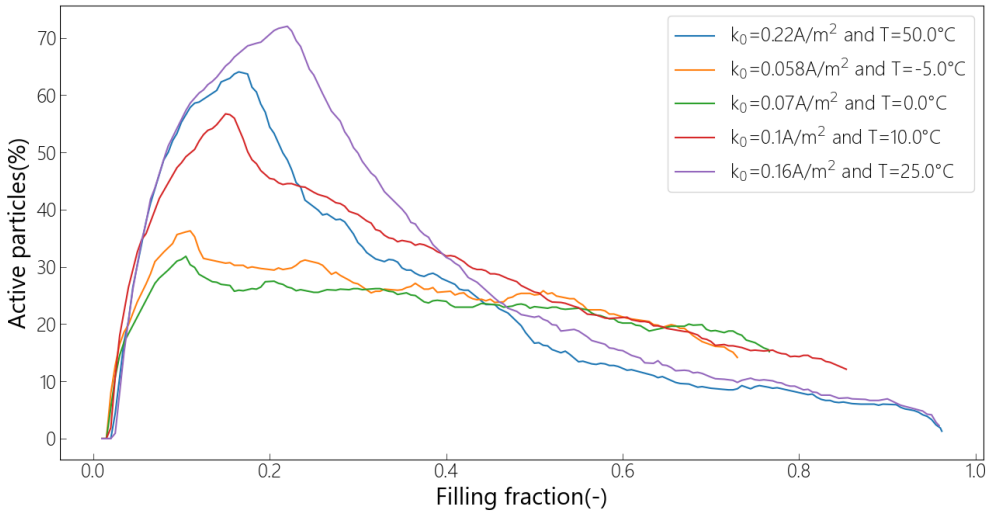

Figure 5.12: Active particle population in 0.5C.

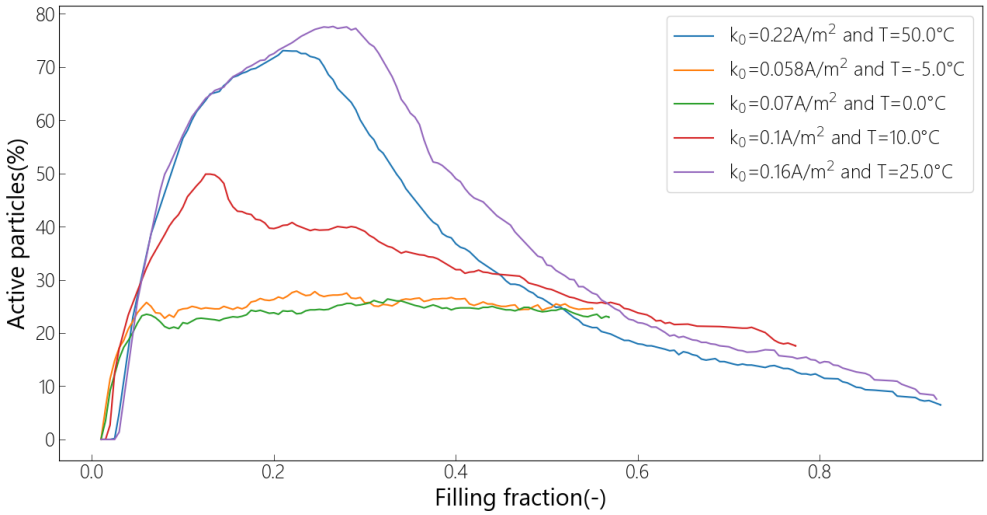

Figure 5.13: Active particle population in 1C.

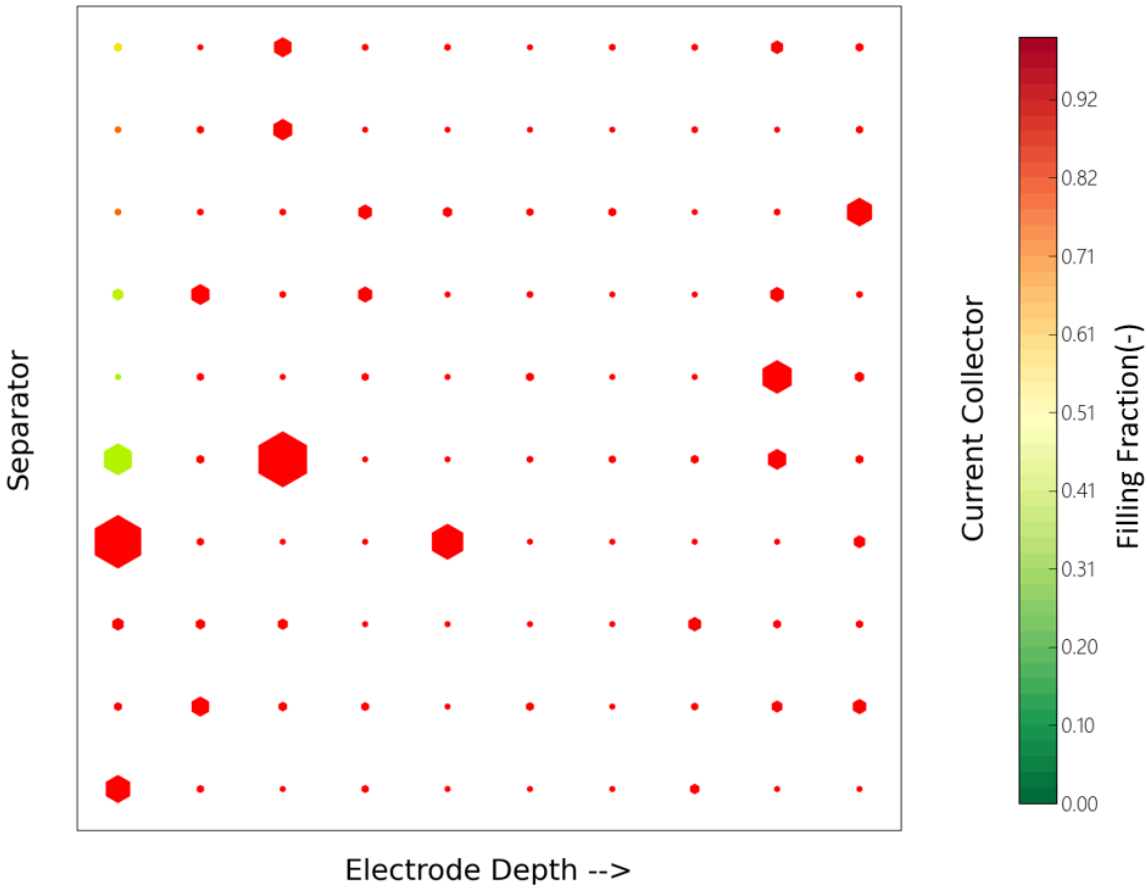

Figure 5.15: SoC in particles with 1C and 25°C.

In the following figure, we present the input parameters utilized to create the heat maps. Selecting these specific values is crucial for examining how a given parameter interacts with factors

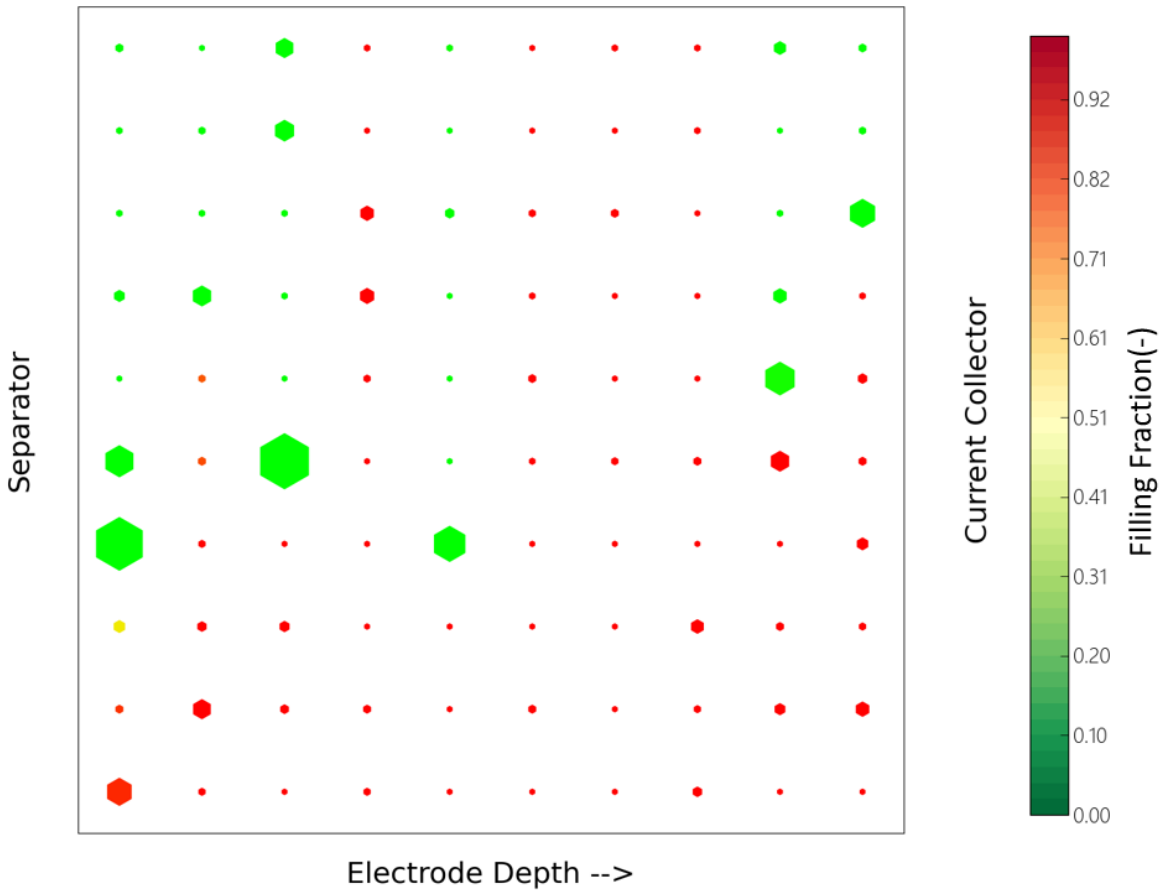

Figure 5.14: SoC in particles at 1C and 0°C.

like temperature or C-rate. Additionally, these parameters closely align with those chosen when validating the model at room temperature.

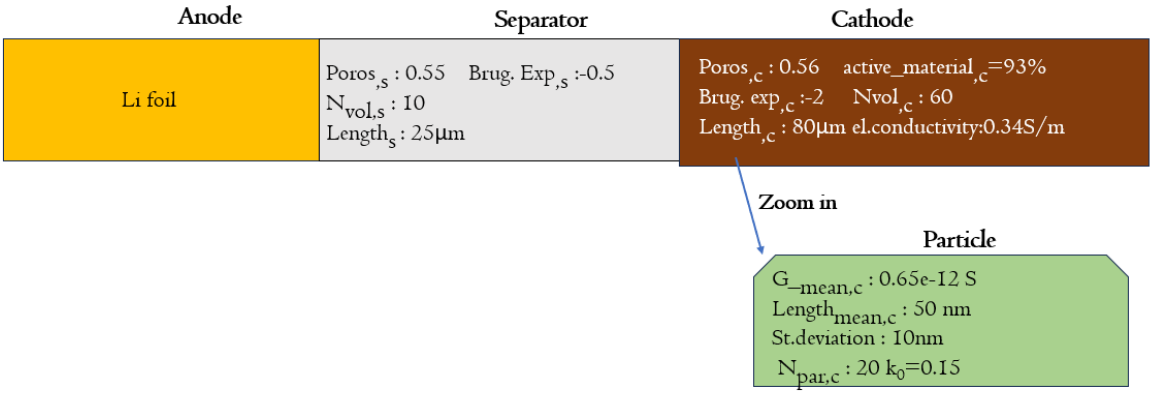

Figure 5.16: Input Specifications for the simulations which are used in the following heat maps.

Before embarking on the sensitivity analysis concerning geometrical properties, it is imperative to establish an understanding of the intricate interplay between the maximum active particle count and variables such as temperature, C-rate, and pivotal parameters like the rate constant or particles

conductivity. To clarify this interrelation, a set of three main plots has been presented for each parameter. These plots are subdivided into two subplots: the left one pertains to the maximum count of active particles, while the right subplot delves into the maximum filling fraction or the state of charge. These plots meticulously elucidate the impact of temperature and the specific research parameter on the aforementioned variables. The initial plot pertains to the 1C rate, followed by the second one for the 2C rate, and the third for the 3C rate. Correspondingly, similar visual representations are crafted for the second parameter in question.

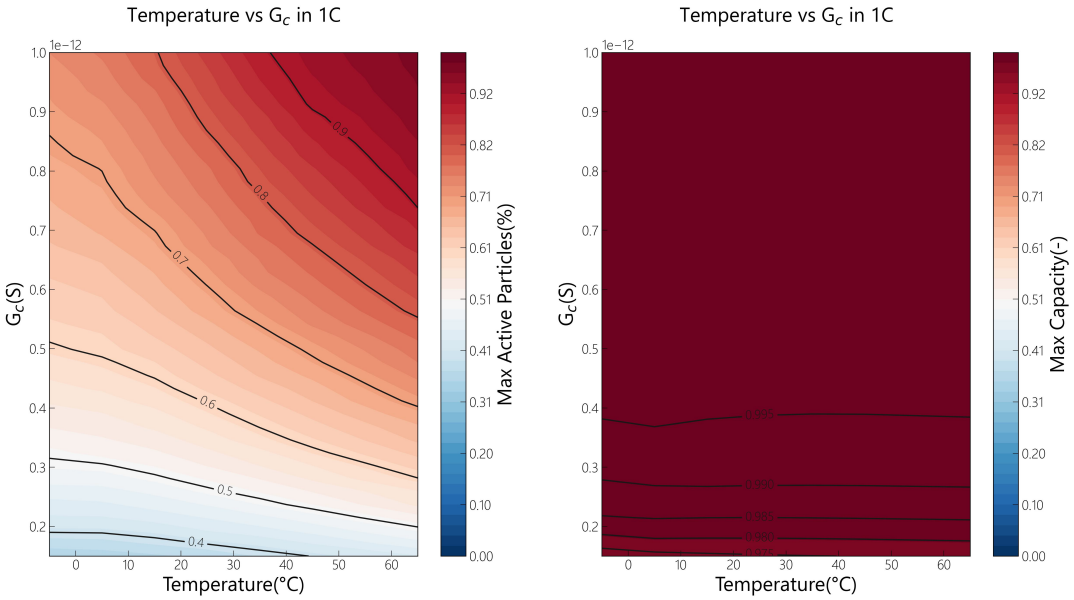

Figure 5.17: Left:Maximum active particle population based on particles conductivity vs temperature in 1C. Right: Filling fraction based on particles conductivity vs temperature in 1C.

The conductivity and the temperature has a very big influence to the maximum active particles. It is intuitive that the decrease of temperature infers a decrease in the maximum active particles but also the value of conductivity has an influence. An important note is that the increase in C-rate does not result to higher maximum active particles, whereas more and more particles can produce the demanding current. This tool can be very useful to realise the importance of particles connectivity and how the heat is generated in the cathode. A future validation with experimental data can be revolutionary in battery community.

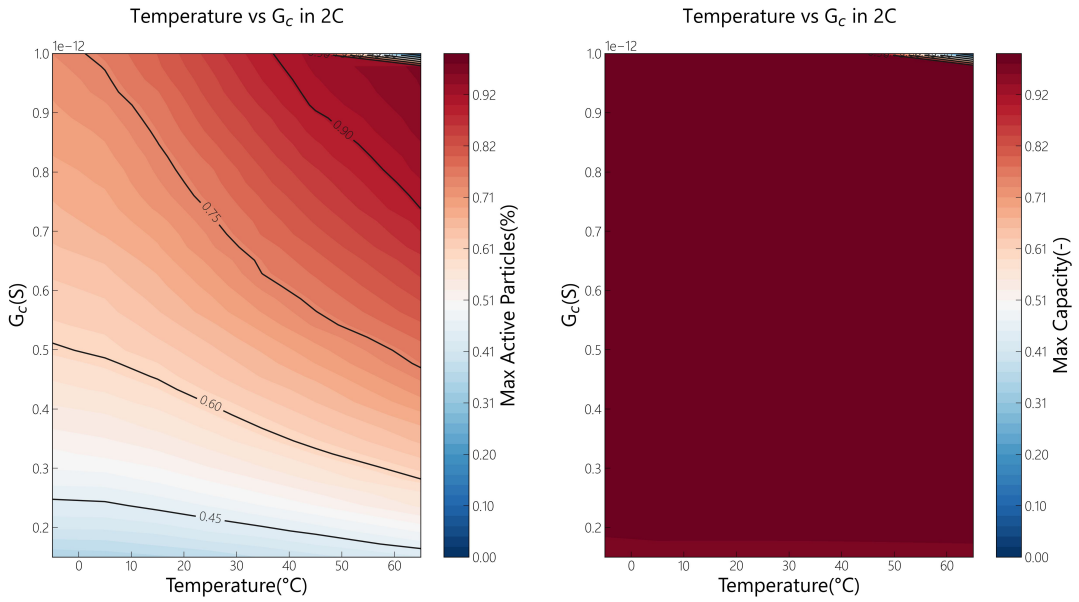

Figure 5.18: Left:Maximum active particle population based on particles conductivity vs temperature in 2C. Right: Filling fraction based on particles conductivity vs temperature in 2C.

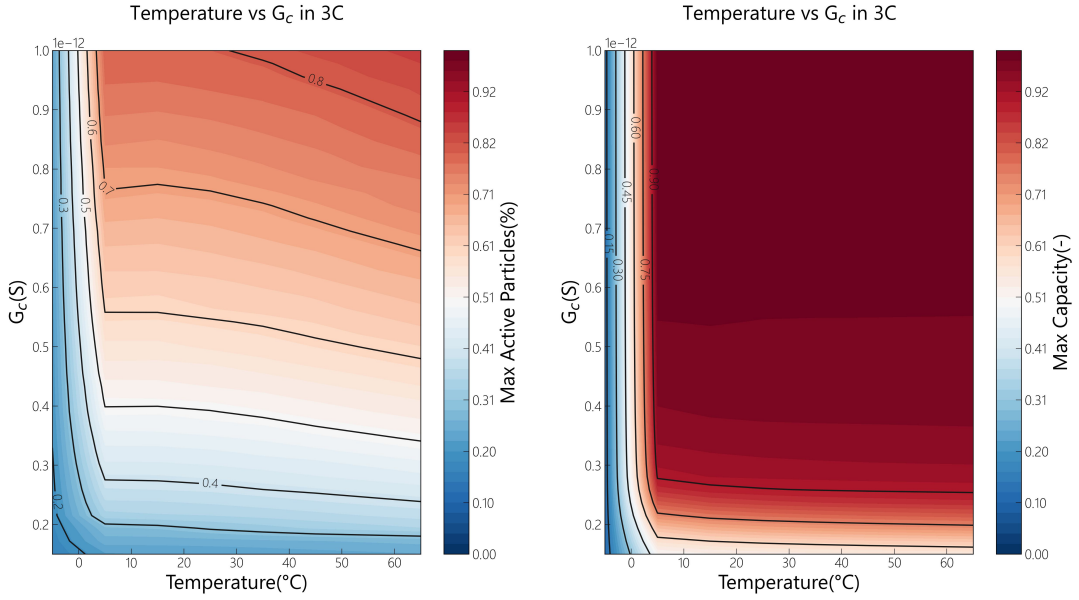

Figure 5.19: Left:Maximum active particle population based on particles conductivity vs temperature in 3C. Right: Filling fraction based on particles conductivity vs temperature in 3C.

Regarding the rate constant, there is a threshold which has an influence in the active particle population. Bigger values than 0.1, shows a drop from 100% to 60%. The rate constant represents the ease of a particle to lose or gain an electron. The higher the value the more energy is required for the

intercalation to happen. The analysis confirms that the prediction of the active particle population is not proportional to temperature in all cases, but variables as the rate constant and conductivity between particles can have a significant influence which can also accumulate all the active particles in a specific region resulting in damage of the cell and even thermal runaway.

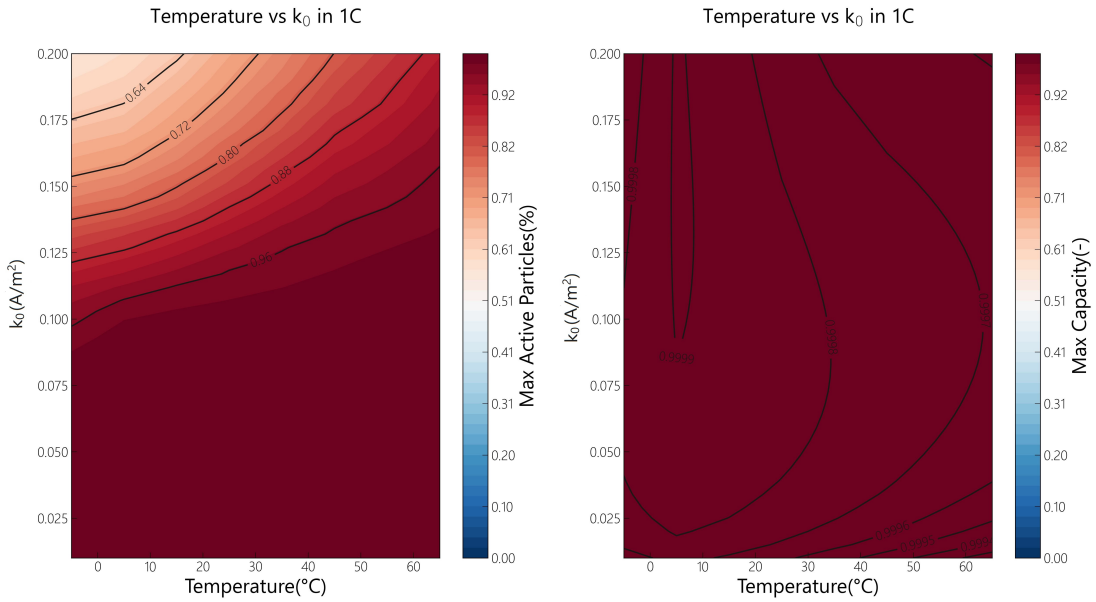

Figure 5.20: Left:Maximum active particle population based on rate constant vs temperature in 1C. Right: Filling fraction based on rate constant vs temperature in 1C.

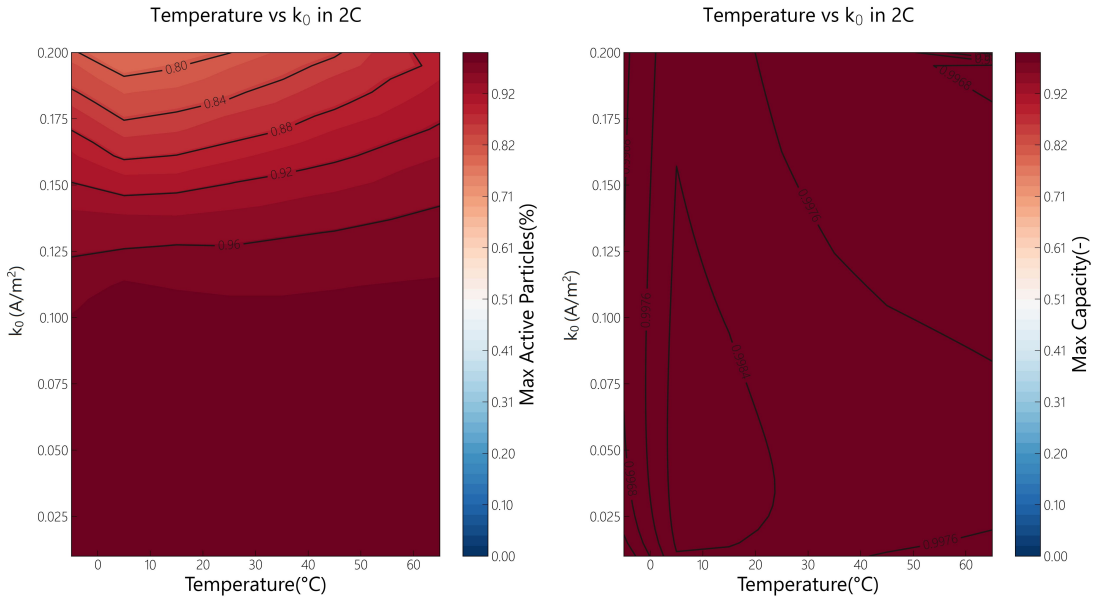

Figure 5.21: Left:Maximum active particle population based on rate constant vs temperature in 2C. Right: Filling fraction based on rate constant vs temperature in 2C.

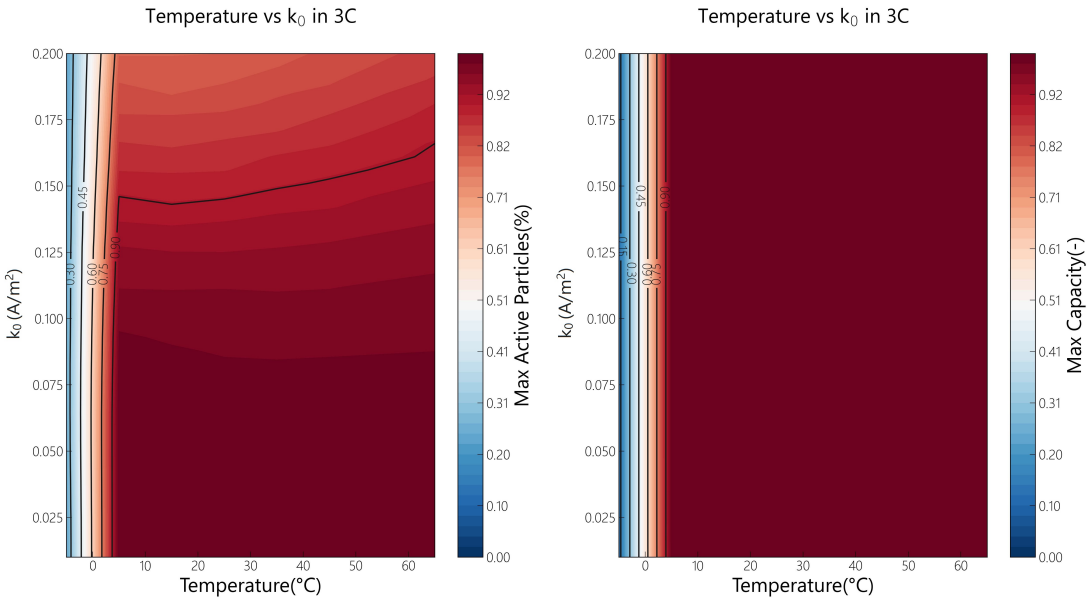

Figure 5.22: Left:Maximum active particle population based on rate constant vs temperature in 3C. Right: Filling fraction based on rate constant vs temperature in 3C

5.4. Temperature influence in design parameters

5.4.1. Particle size with different particle size standard deviation

In the conducted analysis, it is discernible that the operational temperature remains invariant in its effect on the maximum capacity across various particle sizes. Crucially, the study underscores that variations in particle size distribution can exert a considerable influence on the attainable maximum capacity. The implications of this finding suggest that careful consideration of particle size distribution is paramount when optimizing for maximum capacity, irrespective of the operational temperature. This nuanced understanding can offer valuable insights into the design and optimization of energy storage systems.

Furthermore, the more realistic scenario, as presented in the Methodology section, showed the high importance of big standard deviation so as to simulate accurately the state of charge of the battery. In the ideal case, where the particles have equal size, the state of charge can reach almost 100% in all the temperature ranges. On the other hand the maximum value can be 90%.

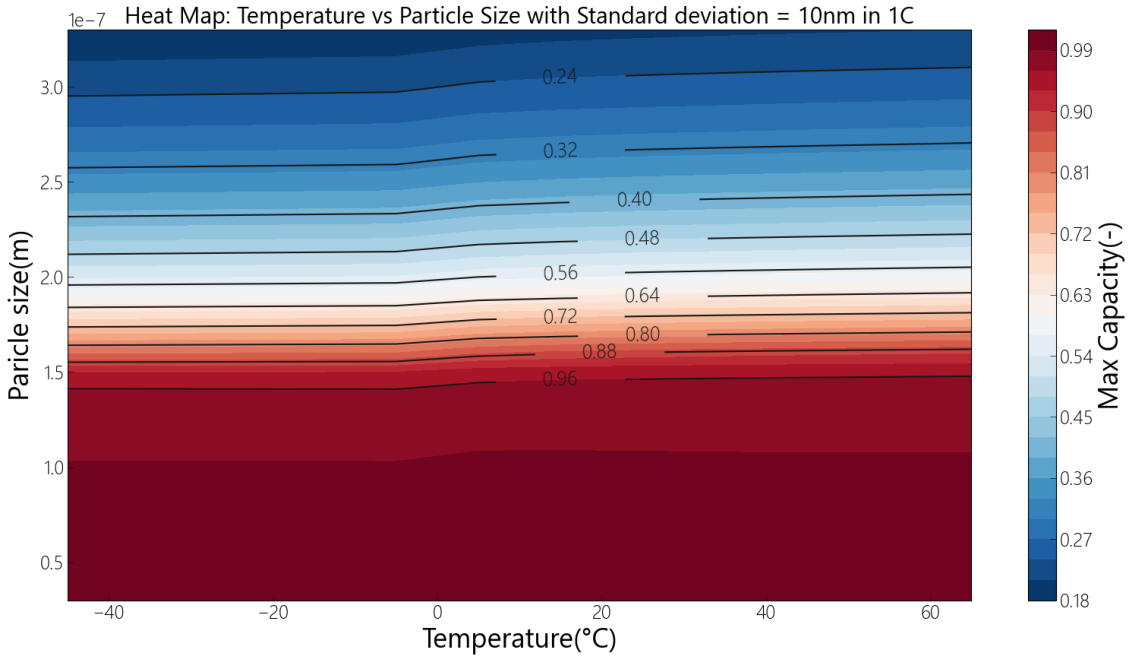

Figure 5.23: Particle size sensitivity with temperature in 1C. with particle standard deviation distribution equal 10nm.

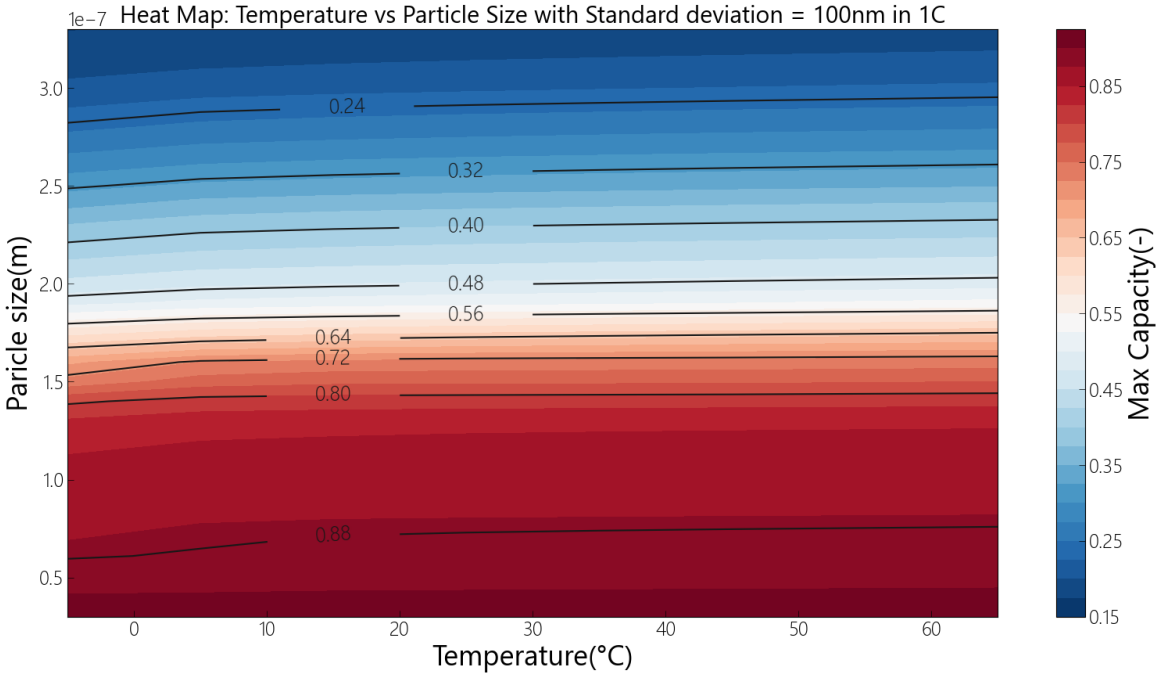

Figure 5.24: Paricle size sensitivity with temperature in 1C. with particle standard deviation distribution equal 100nm.

5.4.2. Cathode Porosity in different C-rates

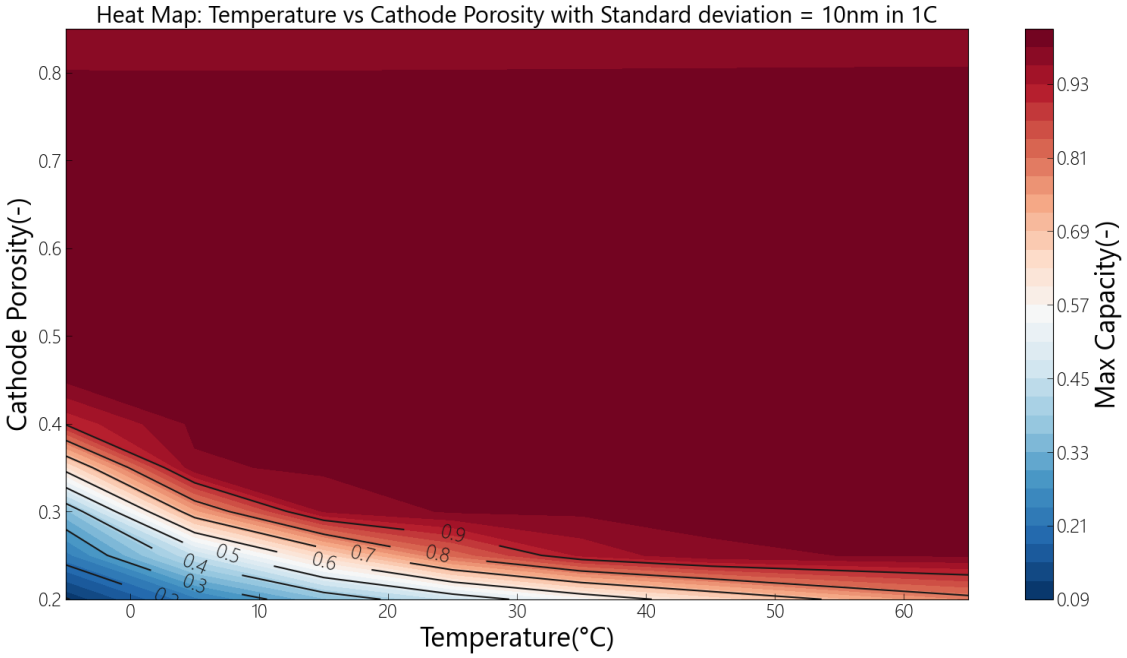

Figure 5.25: Electrode porosity sensitivity with temperature in 1C.

In comparison to the effects of particle size, the relationship between electrode porosity and temperature is more pronounced. At a discharge rate of 1C, porosity should exceed 0.4 to attain the maximum capacity across various temperature scenarios. As the C-rates increase, there's a narrowing of suitable porosity values within distinct temperature regions. This highlights the interplay between porosity and discharge rates, emphasizing the significance of optimizing these parameters for efficient battery operation at different temperatures. Such insights could be pivotal in guiding battery design and performance enhancements.

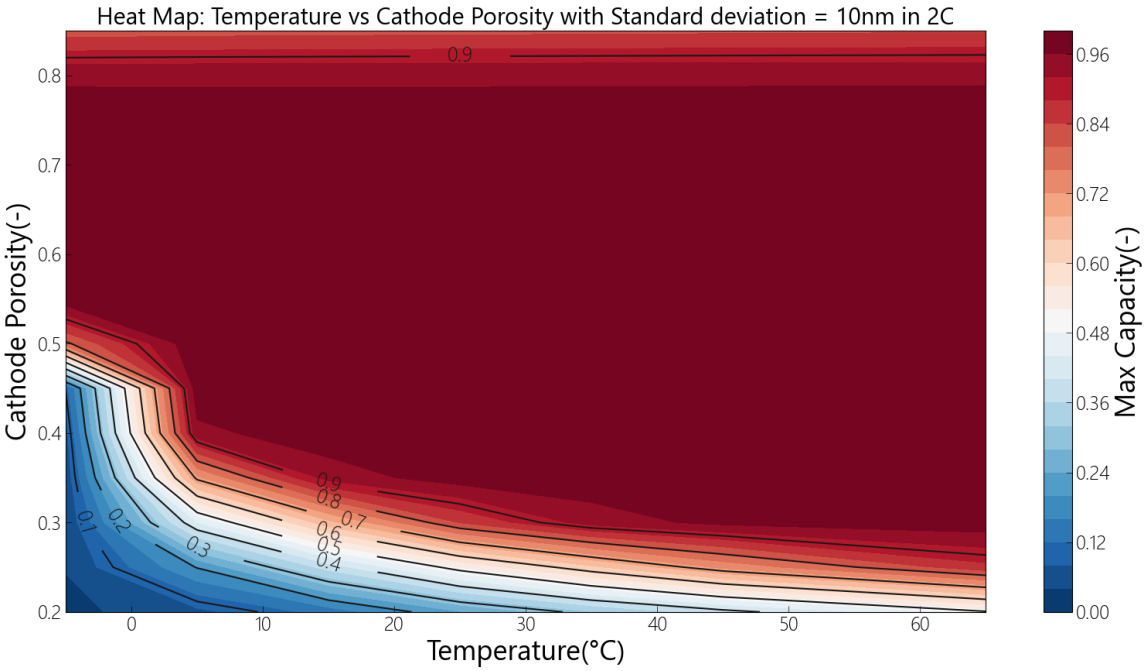

Figure 5.26: Electrode porosity sensitivity with temperature in 2C.

5.4.3. Cathode Electrode Length in different C-rates

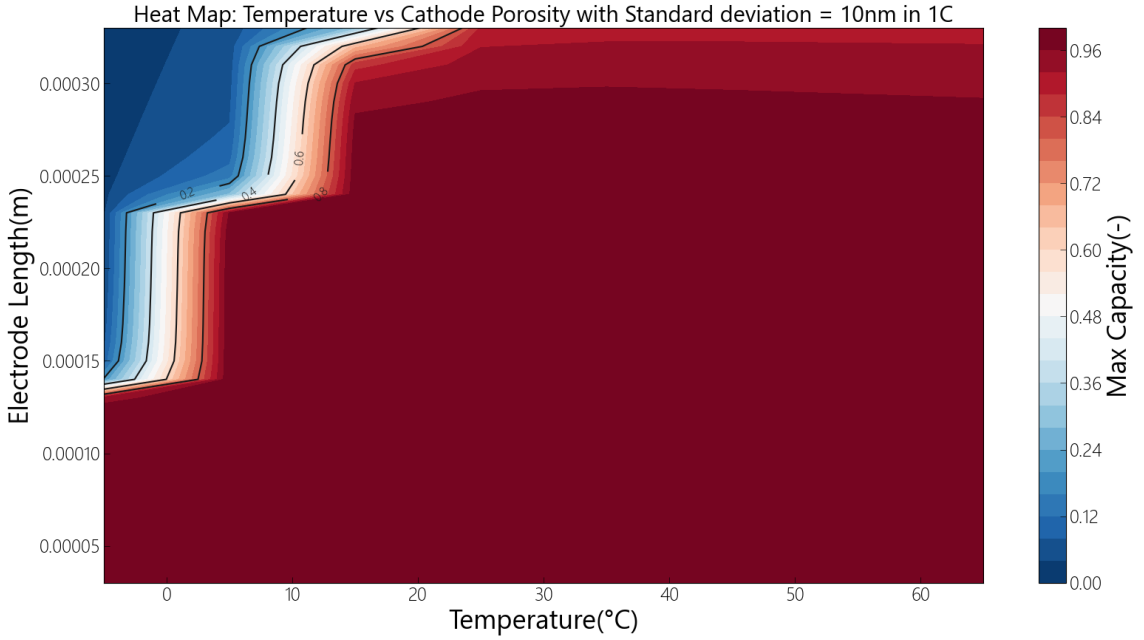

Figure 5.27: Electrode length sensitivity with temperature in 1C.

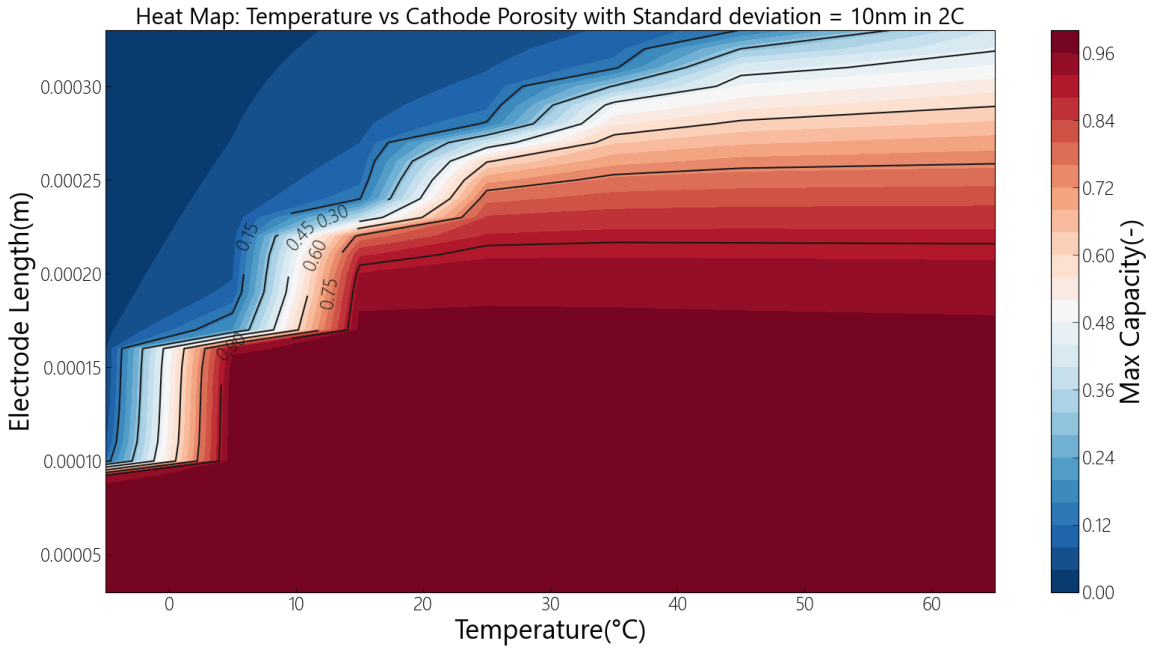

Figure 5.28: Electrode length sensitivity with temperature in 2C.

As the battery operates at different temperatures, the relationship between electrode length and capacity is investigated. At a discharge rate of 1C, the electrode length must surpass a certain critical value to achieve optimal capacity across various temperature ranges. Moreover, as the discharge rates increase, the suitable range of electrode lengths becomes narrower, particularly in distinct temperature regions. This intricate interplay between electrode length and operating temperature underscores the need to carefully consider and optimize these parameters to ensure efficient battery operation under varying temperature conditions. By understanding the crucial role of electrode length in battery performance, researchers and engineers can fine-tune and tailor battery designs.

5.4.4. Tortuosity sensitivity

The Bruggeman exponent plays a pivotal role not only in characterizing tortuosity within the battery structure but also in influencing the effective properties utilized in volume-averaged equations. Although this value is often treated as a fitting parameter to match experimental data, its true significance in simulation scenarios cannot be understated. The Bruggeman exponent governs the pathways through which ions and electrons navigate within the battery, impacting overall transport processes and kinetics.

As temperature variations are taken into account, the influence of the Bruggerman exponent on maximum capacity becomes more and more visible. This phenomenon arises due to the intricate interplay between temperature, tortuosity, and effective properties within the battery structure. The temperature-dependent behavior of the Bruggeman exponent underscores the complexity of battery performance under varying operating conditions.

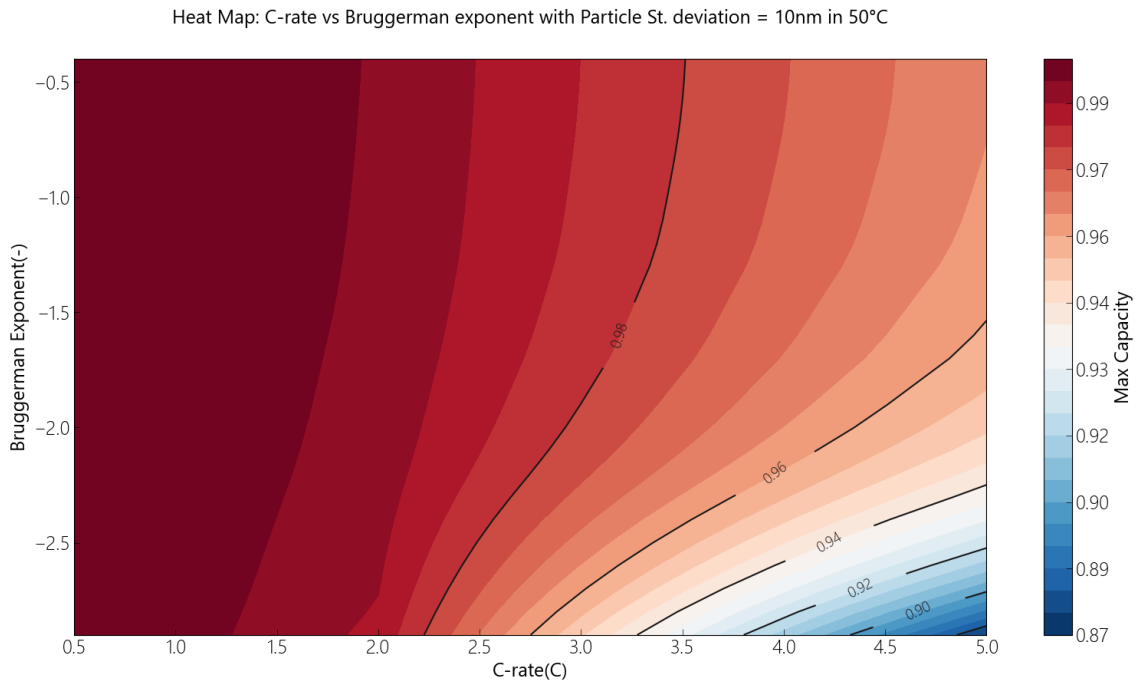

Figure 5.29: Bruggerman exponent sensitivity with current in 323K.

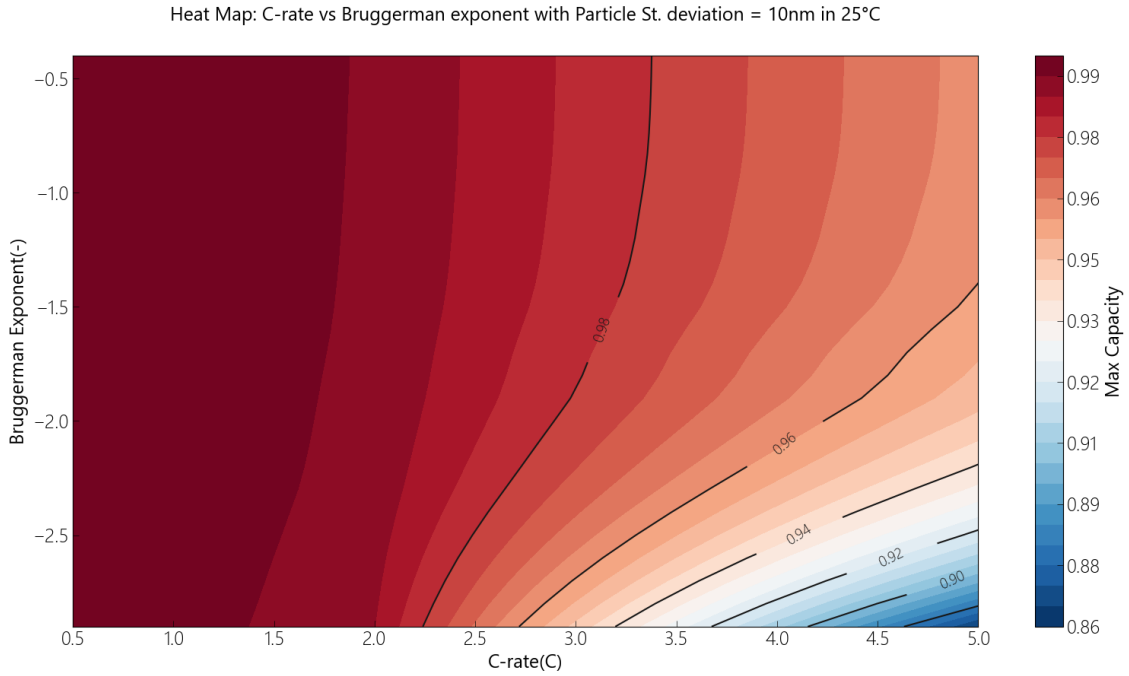

Figure 5.30: Bruggerman exponent sensitivity with current in 298K.

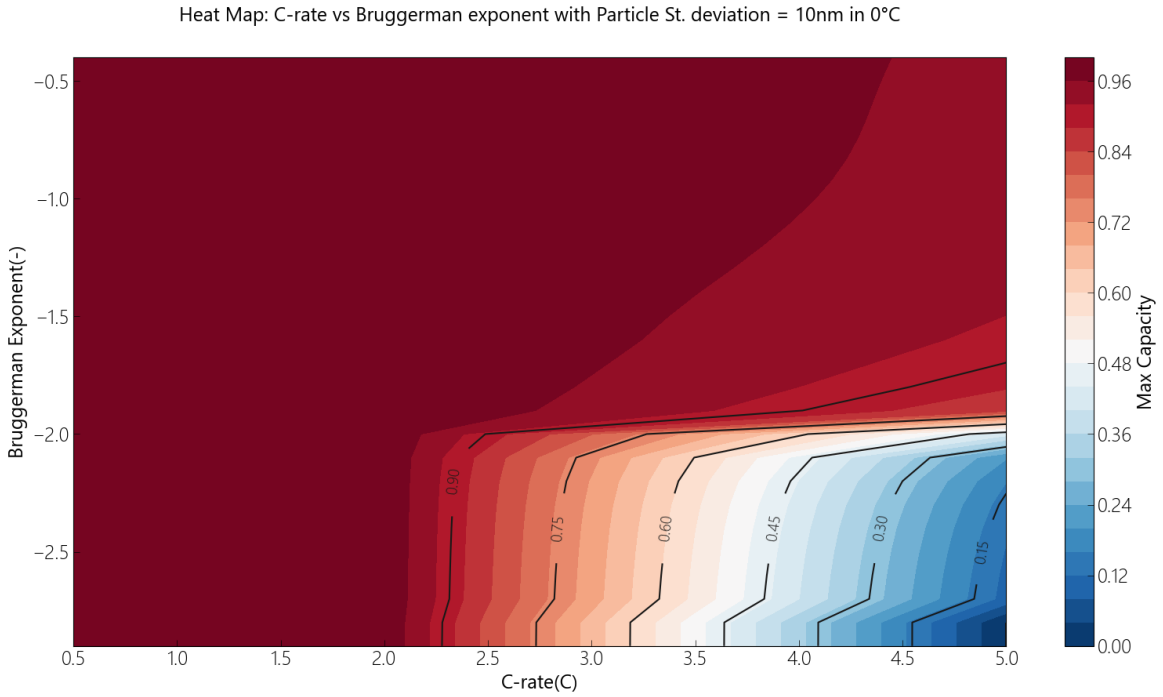

Figure 5.31: Bruggerman exponent sensitivity with current in 273K.

It is essential to comprehend and accurately calibrate the Bruggeman exponent to ensure reliable and accurate simulations of battery behavior across different temperatures. Understanding its role in temperature-dependent performance evaluations is crucial for developing efficient and robust battery models that accurately capture the intricacies of battery operation under real-world conditions.

5.5. Optimal region for LFP battery construction

The conclusion of the mentioned sensitivity analysis is the following graphs. Without paying attention to the operating temperature, the battery can reach in a state of charge higher than 85% in a range of values as can be seen in figure 5.32. Although, this optimal region decreases significantly by taking into consideration the operating temperature. The Bruggerman exponent should be bigger than -2 instead of -2.5, the porosity should be between 52% to 85% instead of 30% to 85%, and the length of cathode electrode should be between 30 to 900 μm instead of 30 to 200 μm. This analysis is based on a coin cell, thus this region should be different for cylindrical cells which can be simulated as many parallel coin cells.

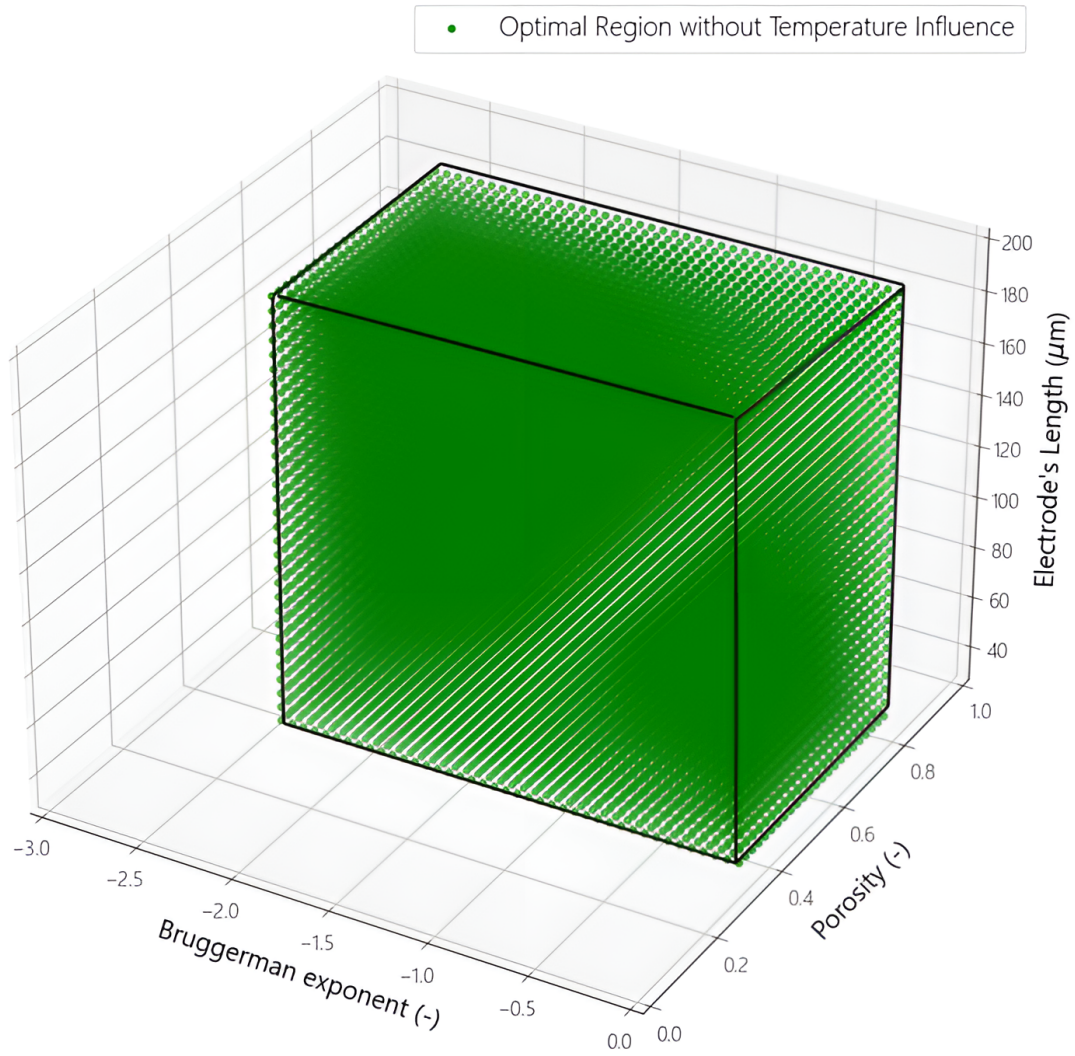

Figure 5.32: Optimal Region without taking into account temperature impact.

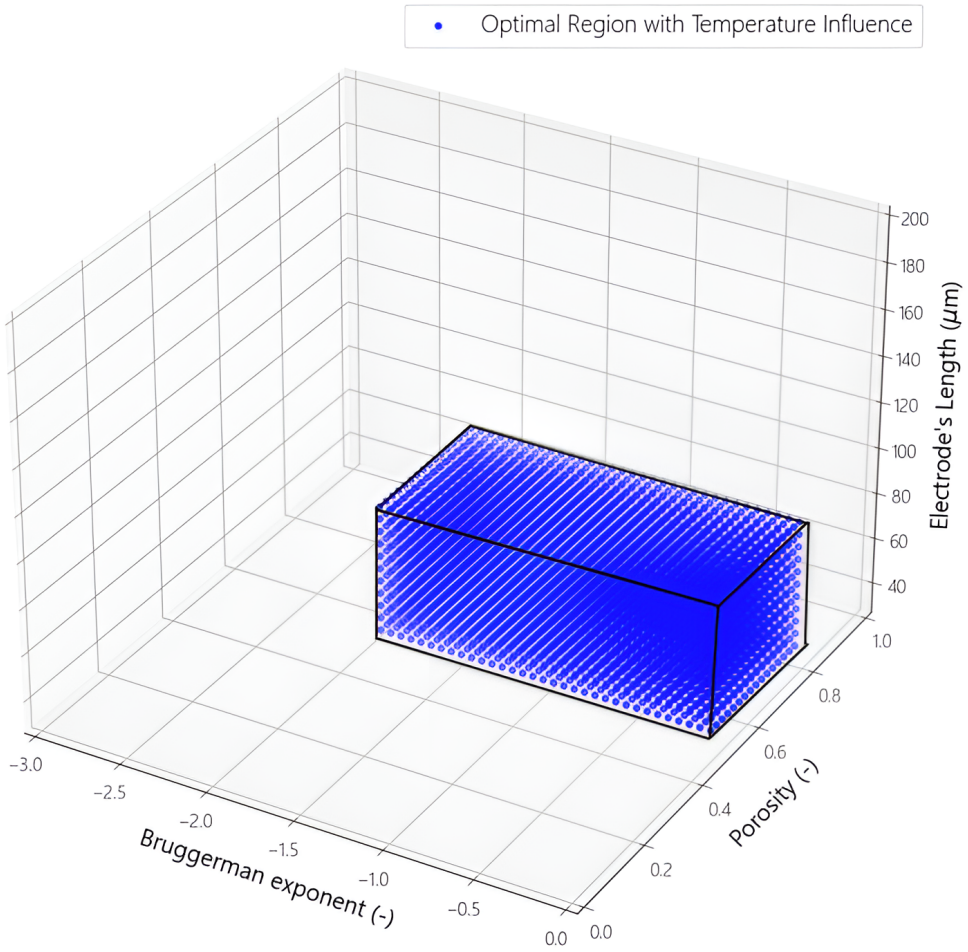

Figure 5.33: Optimal Region with temperature impact.

6

Conclusion

The ongoing debate between physics-based and machine learning models regarding their dominance in battery simulation is a well-recognized phenomenon. The Multiphase Porous Electrode Theory emerges as a model closely related to the DFN (Doyle-Fuller-Newman) framework. It integrates non-equilibrium thermodynamics to effectively capture particle inhomogeneities within the battery electrode structure. The reliability of this model was rigorously assessed through experimental validation.

Coin cells, assembled within the university laboratory, were utilized as experimental batteries. These cells underwent thorough electrochemical testing involving diverse Constant Current-Constant Voltage charge and discharge cycles, enabling the extraction of voltage curves. The results showed the temperature and current dependence in the voltage performance. One of the main outcomes was the capacity loss in the highest experimental temperature and as you increase the current rate. This was explained by degradation mechanisms and state of charge dependence and enable a future research in this subsection of battery simulations.

Introducing a customized Monte Carlo approach applicable to various parameter estimation scenarios, the significant yet unknown parameters were successfully identified. Subsequently, the model underwent validation across five distinct temperatures and two different C-rates, reaffirming its accuracy and robustness. The main outcome of this research was the formulation of two relations as a function of temperature. The rate constant and particles' conductivity exhibit an exponential correlation with temperature. For accurate battery simulation across diverse operational conditions, it is imperative that the model incorporates this temperature-dependent relationship. The degradation also can be artificially simulated if you include a number of cycle dependence in the relation of the particles' conductivity, but this relation should be investigated in another research.

The last result comprised a sensitivity analysis focused on optimizing performance geometry while accounting for temperature influence. In the previous section, the contrasting impact of considering solely C-rate dependence versus incorporating both C-rate and temperature dependence is readily apparent. The model effectively demonstrates its capabilities, motivating further exploration through simulations involving multiple cells. This approach is vital for representing cylindrical cell configurations, thereby establishing a more accurate depiction of the critical region that could serve as a cornerstone in the development of efficient phase-separating lithium-ion batteries.

7

Recommendations

This research is the beginning of a new chapter in research at TU Delft. The experimental investigation of operating temperature and after that, the heat generation in the core of a battery will enhance the understanding of battery operation. The conduction of more experiments in the temperature of interest (below 0 °C and above 50°C) will result to a better understanding of temperature influence not only to the capacity but also to the degradation mechanisms. Experimental techniques which will investigate the surface of the cathode material so as to realise possible aging and loss of active material can be a future study to confirm the findings of this research.

The implementation of a physics-informed neural network would be the next step in the modelling community which can take advantage of both the underlying physics and the machine learning. The results of our research showed encouraging outcomes regarding the random forest regression model which opens the discussion if the increase of data simulations and the implementation of a neural network can improve the accuracy of the results.

A connection between the interpolated functions and the capacity and state of charge should be established. Although an optimal region for construction of LFP batteries is proposed, this corresponds to coin cells. The experiments in cylindrical cells and the modelling of a cylindrical cell using many cells in parallel can create a more robust relation which will correspond to a wider range of battery cells.

The experiments in cylindrical cells should be validated by simulations with the use of MPET. The connection of many different cells will be an important extension of this software which can show its capabilities in many cells and even in a battery pack. The problem of thermal runaway can be meticulously investigated if a physics-based model is implemented in this scale. Although the computational time should be improved and the use of supercomputers for this project is mandatory.

The phase field modelling can be influenced by mechanical stresses which are not included yet in this model. The investigation of heat generation in LFP batteries should also take into account the mechanical stresses that can be created by the deformation of the particles.

A

Appendix

Table A.1: General terminology for batteries

Terminology	Definition	Units
Cell	Consists of two electrodes and electrolyte which enhances the movement of ions. A separator is also present.	No Units
C-Rate	Expresses electrical current. For example, if one battery has capacity of 10 Ah, then the 1C definition means that the battery can be fully discharged in one hour if it provides a constant current of 10A.	A(Ampere)
Cut-off Voltage	Convention voltage where the battery is considered empty and can not be discharged anymore than this point.	V(Voltage)
State Of Charge(SOC)	The amount of charge that is available in the battery.	%
Terminal Voltage	The applied voltage in the two terminals.	V(Voltage)
Open-Circuit Voltage	The Terminal Voltage when no current is flowing in the wire.	V(Voltage)
Porosity(ϵ_s)	The volume fraction $\frac{V_{pore}}{V_{total}}$ where V_{pore} is the void volume that the electrolyte can flow.	No units
Tortuosity(τ)	Fraction which describes the real "path" of a molecule with respect to the distance if the molecule was travelling only in a straight horizontal line. High tortuosity means difficulty on the movement of a molecule which translates to less transportation and less production.	No units
Coulombic efficiency	The ratio between the Discharge capacity to the charge capacity.	%
Energy efficiency	Energy that goes out divided to the energy that is supplied. Energy is the integration of voltage in an infinitesimal capacity difference.	%

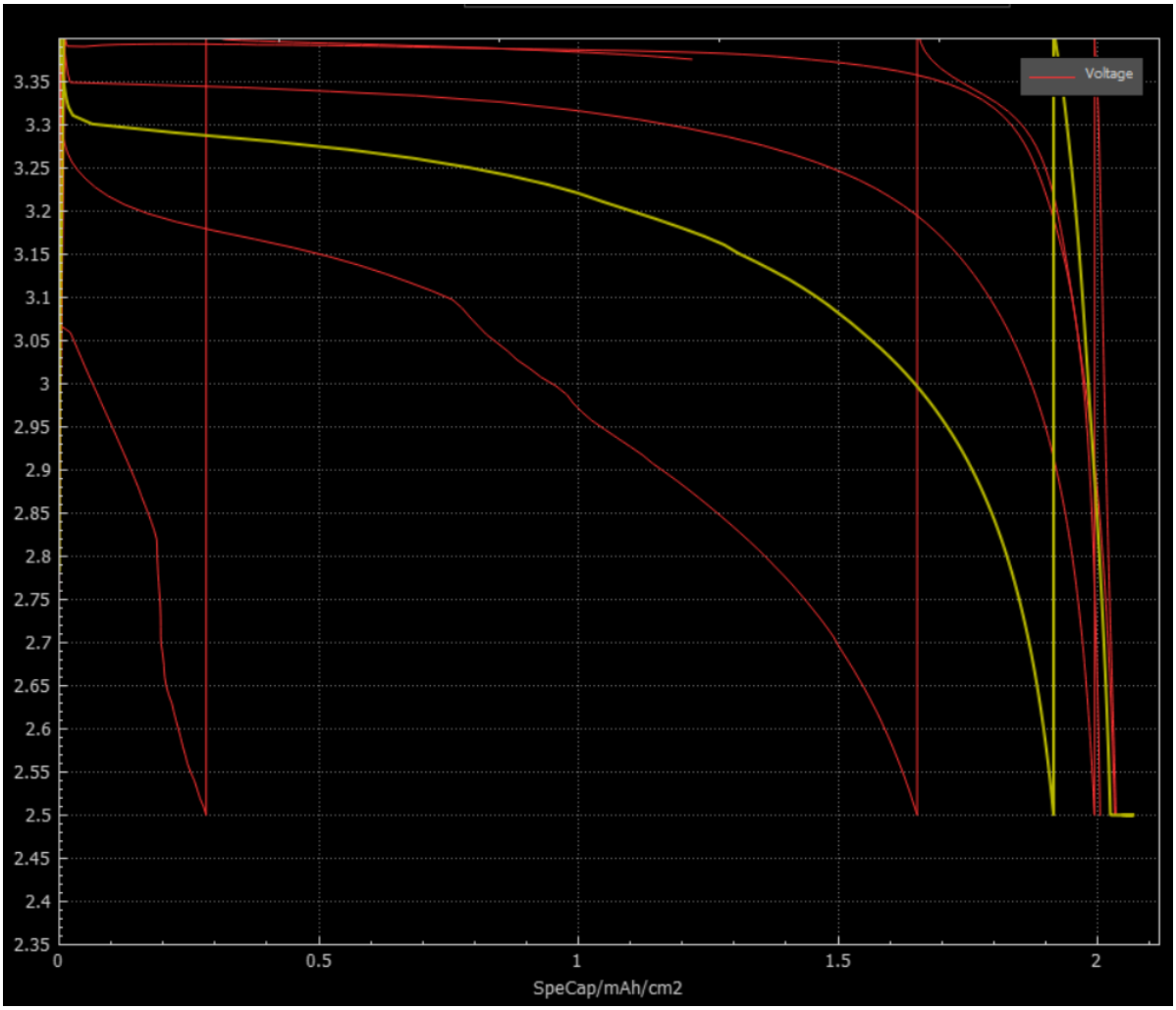

Figure A.1: 1C discharge voltage curve in ambient temperature from Lahne.

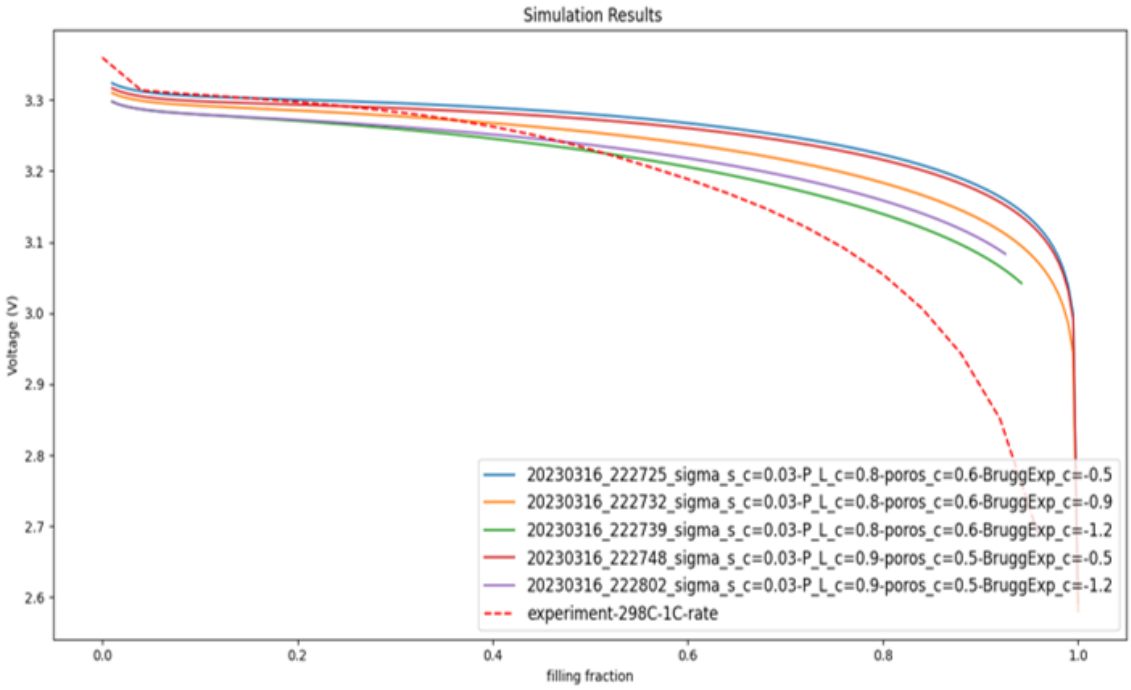

Figure A.2: Some of the results of the simulations and the experimental results in the same graph in the beginning of the project.

Below the comparison between the two coin cells with $1 mAh/cm^2$ and $2 mAh/cm^2$ is presented.

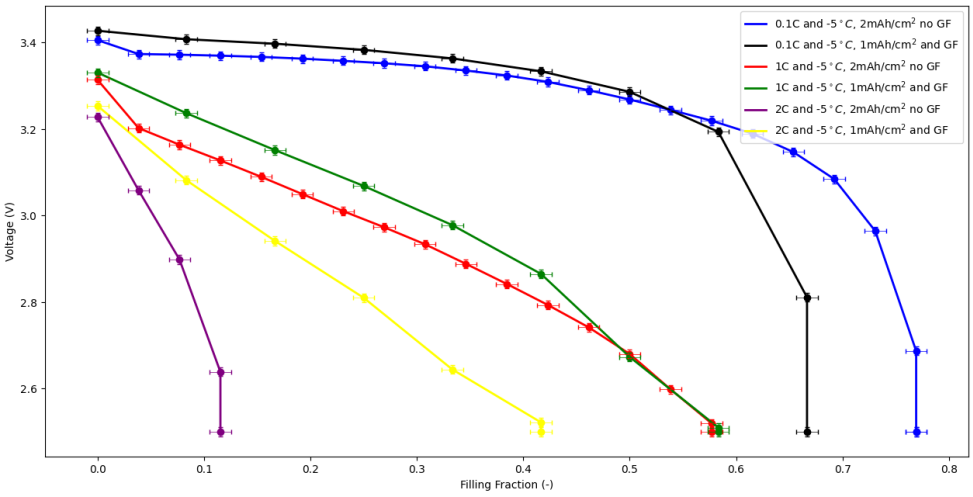

Figure A.3: Comparison between low and high capacity cell in different C-rates at -5°C.

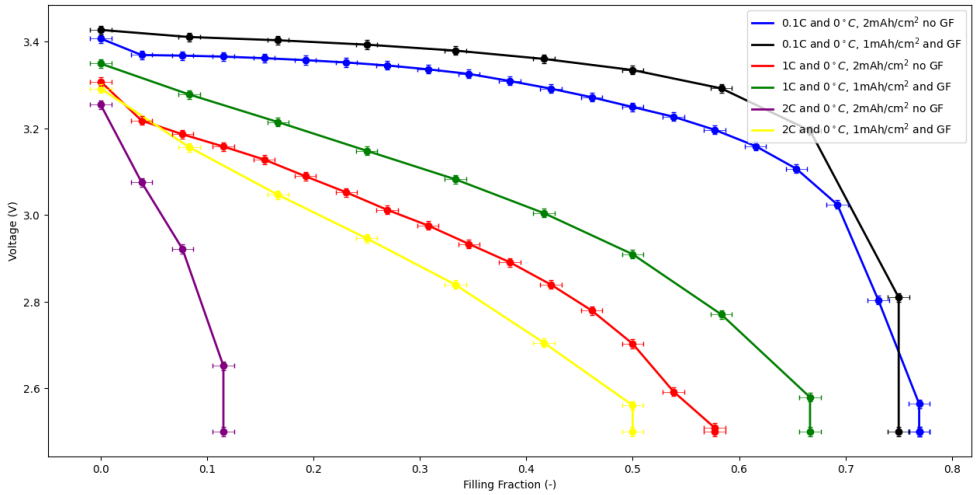

Figure A.4: Comparison between low and high capacity cell in different C-rates at 0°C.

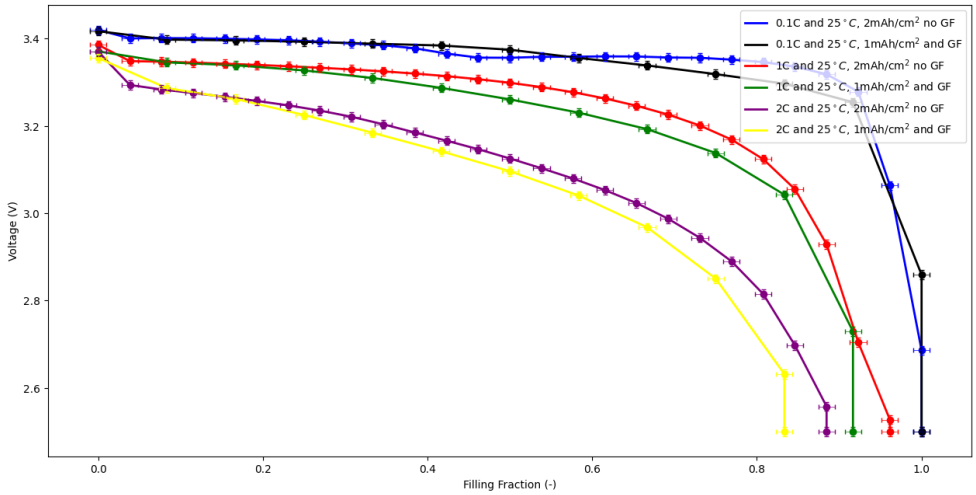

Figure A.5: Comparison between low and high capacity cell in different C-rates at 25°C.

The temperature and the maximum capacity of every material plays an important role to the capacity loss. This is why a relation with the capacity should be implemented in the research.

Furthermore, the behavior of higher capacity loss in higher temperature is also noted in another cell with the same capacity with the cell which is analysed in the main report.

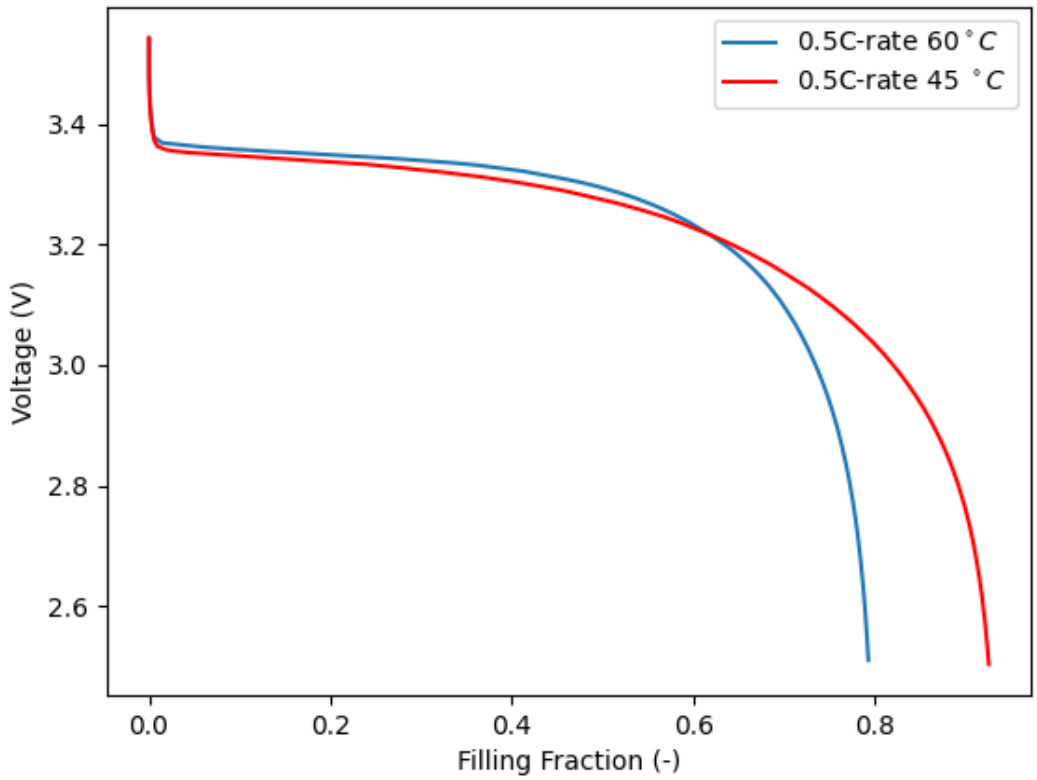

Figure A.6: High capacity cell's voltage curve at 45°C and 60°C at 0.5C.

Some results from the support vector machine regression and the random forest regression by predicting the electrical conductivity.

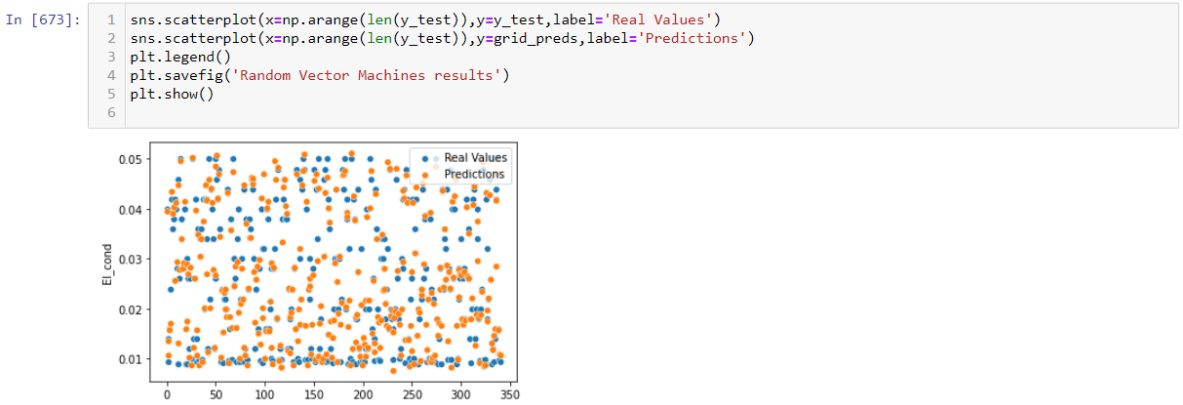

Figure A.7: Support vector machine regression analysis for predicting the electrical conductivity.

In [220]:
```
### Random Forest Regression
from sklearn.ensemble import RandomForestRegressor
trees = [10,50,100]
for n in trees:

    model = RandomForestRegressor(n_estimators=n)

    run_model(model,X_train,y_train,X_test,y_test)

```

```
RMSE : 0.0032450901711629067
RMSE : 0.0029373271329784464
RMSE : 0.0031008552528729973
```

In [221]:
```
signal_range =  average_voltage_k0_0_06_concat
output = model.predict(signal_range.reshape(-1,400))
output
```

Out[221]:
```
array([0.02216])
```

In [222]:
```
### boosting methods
from sklearn.ensemble import GradientBoostingRegressor
model = GradientBoostingRegressor()

run_model(model,X_train,y_train,X_test,y_test)
```

```
RMSE : 0.002669731270837341
```

Out[222]:
```
array([0.02215786])
```

Figure A.8: Random forrest regression with boosting methods to predict the electrical conductivity.

Bibliography

[1] Hamdi Abdi et al. “Chapter 7 - Energy Storage Systems”. In: *Distributed Generation Systems*. Ed. by G.B. Gharehpetian and S. Mohammad Mousavi Agah. Butterworth-Heinemann, 2017, pp. 333–368. ISBN: 978-0-12-804208-3. DOI: https://doi.org/10.1016/B978-0-12-804208-3.00007-8. URL: https://www.sciencedirect.com/science/article/pii/B9780128042083000078.

[2] Mohammad Alipour et al. “A Review on Temperature-Dependent Electrochemical Properties, Aging, and Performance of Lithium-Ion Cells”. In: *Batteries* 6.3 (2020). ISSN: 2313-0105. DOI: 10.3390/batteries6030035. URL: https://www.mdpi.com/2313-0105/6/3/35.

[3] Malin Andersson et al. “Parametrization of physics-based battery models from inputoutput data: A review of methodology and current research”. In: *Journal of Power Sources* 521 (2022), p. 230859. ISSN: 0378-7753. DOI: https://doi.org/10.1016/j.jpowsour.2021.230859. URL: https://www.sciencedirect.com/science/article/pii/S0378775321013458.

[4] Peng Bai and Martin Z. Bazant. “Charge transfer kinetics at the solidsolid interface in porous electrodes”. In: *Nature Communications* 5.1 (Apr. 2014). DOI: 10.1038/ncomms4585. URL: https://doi.org/10.1038%2Fncomms4585.

[5] M. Bini et al. “1 - Rechargeable lithium batteries: key scientific and technological challenges”. In: *Rechargeable Lithium Batteries*. Ed. by Alejandro A. Franco. Woodhead Publishing Series in Energy. Woodhead Publishing, 2015, pp. 1–17. ISBN: 978-1-78242-090-3. DOI: https://doi.org/10.1016/B978-1-78242-090-3.00001-8. URL: https://www.sciencedirect.com/science/article/pii/B9781782420903000018.

[6] Ralph J. Brodd. *Batteries for Sustainability*. Springer New York, NY, 2013, pp. VI, 514. ISBN: 978-1-4614-5790-9.

[7] F Brosa Planella et al. “A continuum of physics-based lithium-ion battery models reviewed”. In: *Progress in Energy* 4.4 (2022).

[8] C. P. Buckley and C. B. Bucknall. Principles of Polymer Engineering. “Potential to kinetic energy and elastic,inelastic collision”. In: (2020). URL: https:http://scienceline.ucsb.edu/getkey.php?key=3948.

[9] Sarah Cairoli. “Consequences of Carbon Emissions for Humans”. In: *Sciencing.com* (2018). URL: https://sciencing.com/consequences-of-carbon-emissions-for-humans-12730960.html.

[10] Eunseok Choi and Sekchin Chang. “A Temperature-Dependent State of Charge Estimation Method Including Hysteresis for Lithium-Ion Batteries in Hybrid Electric Vehicles”. In: *IEEE Access* 8 (2020), pp. 129857–129868. DOI: 10.1109/ACCESS.2020.3009281.

[11] SungYoon Chung, Jason T Bloking, and YetMing Chiang. “Electronically conductive phospho-olivines as lithium storage electrodes”. In: *Nature Materials* 1 (2002), pp. 123–128. URL: https://api.semanticscholar.org/CorpusID:2741069.

[12] Eric C. Darcy. “Passively Thermal Runaway Propagation Resistant Battery Module that Achieves > 190 Wh/kg”. In: 2016.

[13] Van-Huan Duong, Hany Ayad Bastawrous, and Khay Wai See. "Accurate approach to the temperature effect on state of charge estimation in the LiFePO4 battery under dynamic load operation". In: *Applied Energy* 204 (2017), pp. 560–571. ISSN: 0306-2619. DOI: https://doi.org/10.1016/j.apenergy.2017.07.056. URL: https://www.sciencedirect.com/science/article/pii/S0306261917309297.

[14] Hongjeng Zhang Fei Liu Dongfeng Xue. "Selective crystallization with preferred lithium-ion storage capability of inorganic materials". In: (2012).

[15] Xuning Feng et al. "Mitigating Thermal Runaway of Lithium-Ion Batteries". In: *Joule* 4.4 (2020), pp. 743–770. ISSN: 2542-4351. DOI: https://doi.org/10.1016/j.joule.2020.02.010. URL: https://www.sciencedirect.com/science/article/pii/S254243512030088X.

[16] Todd R. Ferguson and Martin Z. Bazant. "Nonequilibrium Thermodynamics of Porous Electrodes". In: *Journal of The Electrochemical Society* 159.12 (Oct. 2012), A1967. DOI: 10.1149/2.048212jes. URL: https://dx.doi.org/10.1149/2.048212jes.

[17] Thomas F. Fuller, M. L. Doyle, and John. Newman. "Simulation and Optimization of the Dual Lithium Ion Insertion Cell". In: *Journal of The Electrochemical Society* 141 (1994), pp. 1–10.

[18] Mostafa Al-Gabalawy, Nesreen S. Hosny, and Shimaa A. Hussien. "Lithium-Ion Battery Modeling Including Degradation Based on Single-Particle Approximations". In: *Batteries* 6.3 (2020). ISSN: 2313-0105. DOI: 10.3390/batteries6030037. URL: https://www.mdpi.com/2313-0105/6/3/37.

[19] John B. Goodenough and Youngsik Kim. "Challenges for Rechargeable Li Batteries". In: *Chemistry of Materials* 22.3 (2010), pp. 587–603. DOI: 10.1021/cm901452z. eprint: https://doi.org/10.1021/cm901452z. URL: https://doi.org/10.1021/cm901452z.

[20] J. Hou et al. "6 - Electrochemistry of rechargeable lithiumair batteries". In: *Rechargeable Lithium Batteries*. Ed. by Alejandro A. Franco. Woodhead Publishing Series in Energy. Woodhead Publishing, 2015, pp. 149–181. ISBN: 978-1-78242-090-3. DOI: https://doi.org/10.1016/B978-1-78242-090-3.00006-7. URL: https://www.sciencedirect.com/science/article/pii/B9781782420903000067.

[21] Gregory L.Plett. *Battery Management Systems:Volume 1, Battery Modelling*. Second. Vol. 1. Sigma Series in Pure Mathematics. Berlin: Artek house Publishers, 2015.

[22] V SHANKAR LAKSHMI VAIDEESWARANNAVIN MITTAL SANAN. "For sustainability. Many challenges of lithium ion batteries". In: (2022). URL: https://www.thehindubusinessline.com/opinion/many-challenges-of-lithium-ion-batteries/article66057886.ece.

[23] Johannes Landesfeind et al. "Tortuosity Determination of Battery Electrodes and Separators by Impedance Spectroscopy". In: *Journal of The Electrochemical Society* 163.7 (Apr. 2016), A1373. DOI: 10.1149/2.1141607jes. URL: https://dx.doi.org/10.1149/2.1141607jes.

[24] Seong Beom Lee et al. "Advanced Battery Management Systems: Modeling and Numerical Simulation for Control". In: *2022 American Control Conference (ACC)*. 2022, pp. 4403–4414. DOI: 10.23919/ACC53348.2022.9867639.

[25] G. B. Less et al. "Micro-Scale Modeling of Li-Ion Batteries: Parameterization and Validation". In: *Journal of The Electrochemical Society* 159.6 (Mar. 2012), A697. DOI: 10.1149/2.096205jes. URL: https://dx.doi.org/10.1149/2.096205jes.

[26] Jiexun Liu, Dawei Gao, and Jianhua Cao. "Study on the effects of temperature on LiFePO4 battery life". In: *2012 IEEE Vehicle Power and Propulsion Conference*. 2012, pp. 1436–1440. DOI: 10.1109/VPPC.2012.6422610.

[27] Garside M. "Reserves of graphite worldwide from 2010 to 2021". In: (2022). URL: https://www.statista.com/statistics/1172356/global-graphite-reservers/.

[28] Victoria Masterson. “The European Union has cut greenhouse gas emissions in every sector - except this one”. In: *Economic forum* (2022). URL: https://www.weforum.org/agenda/2022/09/eu-greenhouse-gas-emissions-transport/.

[29] Janina Molenda et al. “Structural, Transport and Electrochemical Properties of LiFePO4 Substituted in Lithium and Iron Sublattices (Al, Zr, W, Mn, Co and Ni)”. In: *Materials* 6.5 (2013), pp. 1656–1687. ISSN: 1996-1944. DOI: 10.3390/ma6051656. URL: https://www.mdpi.com/1996-1944/6/5/1656.

[30] Sabine Paarmann et al. “Measurement of the Temperature Influence on the Current Distribution in Lithium-Ion Batteries”. In: *Energy Technology* 9.6 (2021), p. 2000862. DOI: https://doi.org/10.1002/ente.202000862. eprint: https://onlinelibrary.wiley.com/doi/pdf/10.1002/ente.202000862. URL: https://onlinelibrary.wiley.com/doi/abs/10.1002/ente.202000862.

[31] Ahmad Pesaran, Shriram Santhanagopalan, and GiHeon Kim. “Addressing the Impact of Temperature Extremes on Large Format Li-Ion Batteries for Vehicle Applications (Presentation)”. In: 2013.

[32] Yuliya Preger et al. “Degradation of Commercial Lithium-Ion Cells as a Function of Chemistry and Cycling Conditions”. In: *Journal of The Electrochemical Society* 167.12 (Sept. 2020), p. 120532. DOI: 10.1149/1945-7111/abae37. URL: https://dx.doi.org/10.1149/1945-7111/abae37.

[33] Iman K. Reksowardojo et al. “Energy Management System Design for Good Delivery Electric Trike Equipped with Different Powertrain Configurations”. In: *World Electric Vehicle Journal* 11.4 (2020). ISSN: 2032-6653. DOI: 10.3390/wevj11040076. URL: https://www.mdpi.com/2032-6653/11/4/76.

[34] G. Richardson and I. Korotkin. “Heat generation and a conservation law for chemical energy in Li-ion batteries”. In: *Electrochimica Acta* 392 (2021), p. 138909. ISSN: 0013-4686. DOI: https://doi.org/10.1016/j.electacta.2021.138909. URL: https://www.sciencedirect.com/science/article/pii/S0013468621011993.

[35] G. W. RICHARDSON et al. “Charge transport modelling of Lithium-ion batteries”. In: *European Journal of Applied Mathematics* 33.6 (2022), pp. 983–1031. DOI: 10.1017/S0956792521000292.

[36] Renato Seeber, Chiara Zanardi, and György Inzelt. “Links between electrochemical thermodynamics and kinetics”. In: *ChemTexts* 1 (2015), pp. 1–16.

[37] Ho Chul Shin, Won Il Cho, and Ho Jang. “Electrochemical properties of carbon-coated LiFePO4 cathode using graphite, carbon black, and acetylene black”. In: *Electrochimica Acta* 52.4 (2006). ELECTROCHEMICAL ENERGY CONVERSION AND STORAGE - ISE MEETING 2005, pp. 1472–1476. ISSN: 0013-4686. DOI: https://doi.org/10.1016/j.electacta.2006.01.078. URL: https://www.sciencedirect.com/science/article/pii/S0013468606004026.

[38] Raymond B. Smith and Martin Z. Bazant. “Multiphase Porous Electrode Theory”. In: *Journal of The Electrochemical Society* 164.11 (June 2017), E3291. DOI: 10.1149/2.0171711jes. URL: https://dx.doi.org/10.1149/2.0171711jes.

[39] Lena Spitthoff, Paul R. Shearing, and Odne Stokke Burheim. “Temperature, Ageing and Thermal Management of Lithium-Ion Batteries”. In: *Energies* 14.5 (2021). ISSN: 1996-1073. DOI: 10.3390/en14051248. URL: https://www.mdpi.com/1996-1073/14/5/1248.

[40] S. Tamilselvi et al. “A Review on Battery Modelling Techniques”. In: *Sustainability* 13.18 (2021). ISSN: 2071-1050. DOI: 10.3390/su131810042. URL: https://www.mdpi.com/2071-1050/13/18/10042.

[41] Marian Tomasov et al. “Overview of Battery Models for Sustainable Power and Transport Applications”. In: *Transportation Research Procedia* 40 (2019). TRANSCOM 2019 13th International Scientific Conference on Sustainable, Modern and Safe Transport, pp. 548–555. ISSN: 2352-1465. DOI: https://doi.org/10.1016/j.trpro.2019.07.079. URL: https://www.sciencedirect.com/science/article/pii/S235214651930242X.

[42] Lars Ole Valøen and Jan Naess Reimers. “Transport Properties of LiPF6-Based Li-Ion Battery Electrolytes”. In: *Journal of The Electrochemical Society* 152 (2005).

[43] Alexandros Vasileiadis et al. “Toward Optimal Performance and InDepth Understanding of Spinel Li4Ti5O12 Electrodes through Phase Field Modeling”. In: *Advanced Functional Materials* 28 (2018).

[44] Tingting Wang et al. “Thermal Modeling and Prediction of The Lithium-ion Battery Based on Driving Behavior”. In: *Energies* 15.23 (2022). ISSN: 1996-1073. DOI: 10.3390/en15239088. URL: https://www.mdpi.com/1996-1073/15/23/9088.